Contract No. NAS9-13162
DRL NO. 2
DRD No. MA-129TA
MDC G5058

CR-134193

DESIGN, FABRICATION, TEST, AND DELIVERY OF A K-BAND ANTENNA BREADBOARD MODEL

Final Report
January 1974

McDonnell Douglas Astronautics Company
5301 Bolsa Avenue
Huntington Beach, California 92647

Contract No. NAS9-13162
DRL No. 2
DRD NO. MA-129TA
MDC G5058

DESIGN, FABRICATION, TEST, AND DELIVERY OF A K-BAND ANTENNA BREADBOARD MODEL

Final Report
January 1974

Approved by
R. L. BEAVIN
Project Manager

McDonnell Douglas Astronautics Company
5301 Bolsa Avenue
Huntington Beach, California 92647

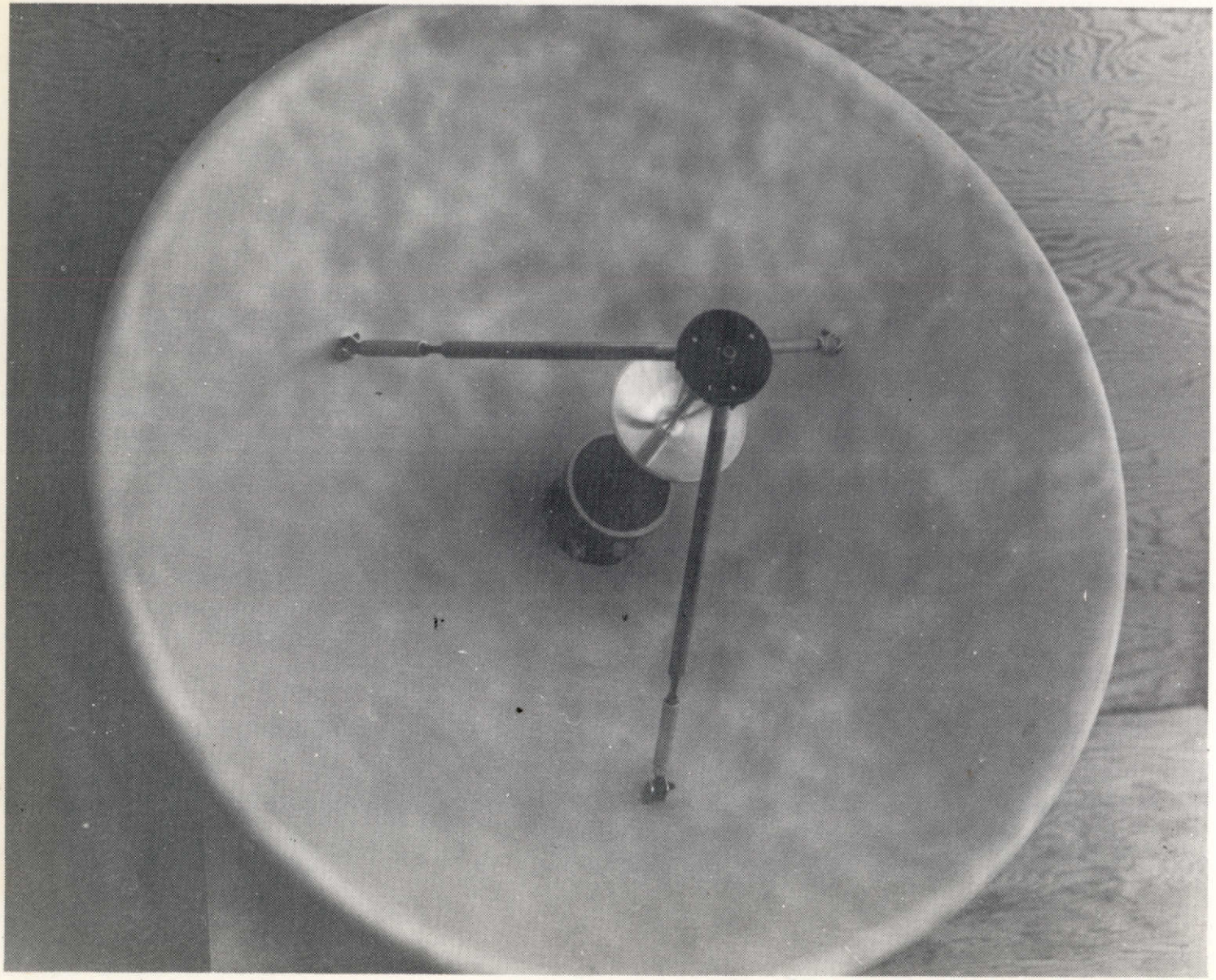

Ku-Band Single-Channel Monopulse Antenna Assembly

ABSTRACT

This report presents the results of a research effort to develop a Ku-Band single-channel monopulse antenna with significant improvements in efficiency and bandwidth. A single-aperture, multi-mode horn, utilized in a near-field Cassegrainian configuration, was the technique selected for achieving the desired efficiency and bandwidth performance.

In order to provide wide polarization flexibility, a wire-grid, space-filter polarizer was developed. A solid-state switching network with appropriate driving electronics provides the receive channel sum and difference signal interface with an existing Apollo-type tracking electronics subsystem.

A full-scale breadboard model of the antenna, consisting of a near-field feed network, circular polarizer, Cassegrainian reflectors, and tracking network, was fabricated and tested. Performance of the model was well within the requirements and goals of the contract. An overall antenna subsystem efficiency approaching 70 percent was shown to be achievable over a bandwidth of 1.25 GHz. Included in this report are the analytical bases of each of the components and of the antenna assembly, summaries of trades performed to determine optimum alternatives, and the test results obtained with each element and with the final antenna assembly.

CONTENTS

Section 1
INTRODUCTION

The objective of this contract was to design, fabricate, and test a breadboard model of a single-channel monopulse feed and reflector assembly for operation at K_u-band, in support of earth-orbiting spacecraft. The antenna assembly is intended for the purpose of evaluation at NASA-MSC in conjunction with an Apollo type antenna electronics box and a breadboard K_u-band transceiver.

Single-channel monopulse tracking for communications antennas was successfully developed at S-band for the NASA Apollo program. The driving force which led to the Apollo single-channel tracking development was the weight and power reduction made possible by the fact that no auxiliary receivers are required. While weight and power will not be quite as critical for future programs, they will remain extremely important considerations, and costs are becoming much more crucial. The elimination of auxiliary receivers offers substantial cost savings.

The radio frequency (RF) implementation of the tracking techniques developed for Apollo at S-band cannot be utilized effectively at the higher frequencies. It was therefore considered judicious to develop a breadboard antenna model at K_u-band to assess the feasibility of a high-performance, wideband, single-channel monopulse system.

It has been shown (Reference 1) that to achieve a specified value of antenna gain, an increase in antenna efficiency of 10 percent provides the performance equivalent of a reflector diameter change which would result in a 20 percent increase in structural cost. Also, the reproduction cost of a high-efficiency feed is comparable to that for a low-efficiency configuration, while the cost of reproduction of a reflector varies with the square or cube of the diameter. These considerations, when coupled with the obvious spacecraft penalties of increased weight and packaging problems attendant to increased antenna size, strongly justify design effort to optimize antenna efficiency.

The major requirements imposed on the antenna design included (1) maximization of antenna efficiency; (2) flexibility to provide any combinations of left and right circular, or linear, polarization; (3) compatibility with Apollo antenna tracking electronics; and (4) wideband operation.

The approach taken to meet these requirements was based substantially on the results of previous MDAC independent research studies aimed at performance optimization of space communication antennas. The antenna configuration selected consists of a multimode feed network with rectangular aperture horn, which provides the pattern shaping required for aperture efficiency and the generation of monopulse tracking signals, an external space filter for generation of circular polarization, and near-field Cassegrainian reflector. A solid-state switching and phase-shifting network was developed to modulate the sum pattern with the elevation and azimuth difference patterns for single-channel operation.

Results achieved with this configuration demonstrate the validity of the selected design approach. An aperture efficiency of 87 percent was attained over a bandwidth of 1.25 GHz, and an overall antenna subsystem efficiency approaching 70 percent was shown to be achievable for a circularly polarized monopulse tracking antenna.

A lightweight antenna configuration, utilizing a graphite-epoxy composite material in a semi-monocoque construction, was designed. This type of construction offers a substantial weight reduction coupled with excellent thermal distortion characteristics. Design details of the lightweight antenna are provided in the report.

This contractual effort was performed for the Telemetry and Communications System Division of the Manned Spacecraft Center, National Aeronautics and Space Administration, under contract NAS9-13162. The technical monitor for the program was Mr. James S. Kelly of the NASA-MSC Electromagnetic Systems Branch.

Section 2

ANTENNA DEVELOPMENT

2.1 CONTRACT TECHNICAL REQUIREMENTS

The following technical requirements and specifications were imposed on the antenna assembly:

A. Design must be flexible enough to support any combinations of right and left circular polarization for transmitting and receiving. The deliverable unit will be assembled so as to transmit left and receive right. In addition, all of the necessary components will be provided to allow assembly for any combination of transmit-receive polarizations.

B. As a design goal, the antenna assembly shall handle 50 watts (or greater) of transmitter power. Verification by test is not required.

C. The design shall maximize transmit-receive isolation to the extent possible; however, special filters are not required solely for the purpose of isolation.

D. Modulation level of error signal on the receiver channel sum signal shall be 20 ± 2 percent per degree within the 3-db beamwidth*. Modulation effects on the transmit channel shall be negligible.

E. Switching voltages to be made available by MSC are +5, -50 volts at 50 $\angle 0°$ Hz and 50 $\angle -90°$ Hz supplied from an Apollo-type electronics box.

F. Antenna and lobing system must be compatible with Apollo tracking electronics.

G. Feed and lobing network are of prime importance. Efficiency of feed and lobing components shall be maximized.

---

*The modulation level was changed at NASA-MSC request from 1 to 2 percent per degree within ±25 percent of the 3-db beamwidth at the outset of the program. The current specification was accepted as a design goal.

H. Pointing accuracy to be within the pattern 1-db beamwidths for both transmitting and receiving, including effects of tracking errors, beam misalignments, etc.

I. No requirement is set for delivered system weight; however, the configuration selected must have potential of lightweight implementation. The lightweight design data shall be provided.

J.* Transmitter frequency: 14.550 GHz to 14.750 GHz
Receiver frequency: 13.500 GHz to 13.700 GHz

K. The antenna reflector shall be sized for a beamwidth of 1 to 1.5 degrees.

L. The delivered model is to be breadboard in nature. Components to be supplied include antenna reflectors, circularly polarized feed system, and combining and isolating components needed to provide sum and error signals and to isolate the transmit channel from the lobing switches.

2.2 TECHNICAL APPROACH

2.2.1 Subsystem Implementation

The selection of an optimum design approach for a high-efficiency antenna subsystem involves the consideration of a variety of techniques and application-imposed constraints. A previous MDAC Independent Research and Development (IRAD) effort (Reference 2) included a trade study which determined the near-field multimode feed in a Cassegrainian configuration to be the most promising candidate for achieving very high efficiency and wideband performance. A number of other candidates, including multiple-horn clusters, focal-plane matched feeds, scalar (corrugated) horns, dielguide, and far- and near-field, conical and rectangular multimode feeds were investigated in that study. Considering as primary parameters efficiency, bandwidth, and capability to provide monopulse tracking, the near-field

*The operating frequencies were changed at NASA-MSC request early in the program. Original frequency specification was 15.2190 GHz to 15.2367 GHz for the transmitter, and 14.2808 GHz to 14.3008 GHz for the receiver.

multimode technique was selected. The rectangular aperture was chosen over the conical version mainly because of bandwidth characteristics and simplicity of the feed structure (References 3 and 4).

The near-field multimode feed combines the beam-collimating properties of near-field feeds with the beam shaping and monopulse capabilities of controlled higher-order mode radiation. The Cassegrainian reflector configuration offers operational convenience (i.e., structural and packaging geometry), flexibility in feed system design to properly use the near-field characteristics, and a longer effective focal length to optimize the monopulse tracking (Reference 5). In addition, Cassegrainian antennas demonstrate (Reference 6) exceptional cross-polarization characteristics which increase cross-polarization efficiency as well as easing the achievement of circular polarization over a large bandwidth.

It is obvious from the above that the various elements making up a high-performance antenna are very interdependent and cannot be considered independently, particularly the feed network and reflector elements. In the present design, the polarizer and tracking (single-channel monopulse lobing) networks are more loosely coupled to other system elements but, as will be shown in the following discussions, still have considerable impact on the other elements and the achievable results are degraded if any possible interactions are overlooked.

2.2.2 Antenna Efficiency

In this section, the terms relating to each aspect of antenna efficiency are defined. The ideal gain of a paraboloidal antenna, corresponding to zero spillover, blockage, losses, etc., and uniform aperture illumination in both amplitude and phase, is given by

$$G_o = \frac{4\pi A}{\lambda^2} \tag{1}$$

where A is the physical aperture area. The actual gain for the antenna is related to the ideal by an efficiency factor η;

$$G = \eta G_o \tag{2}$$

In turn, η can be expressed as the product of a number of (not necessarily independent) factors, each corresponding to an effect which reduces on-axis gain.

$$\eta = \eta_i \eta_{i\phi} \eta_s \eta_b \eta_x \eta_r \eta_h \eta_a \eta_m \eta_e \tag{3}$$

where

η_i is the primary feed amplitude illumination efficiency

η_ϕ is the primary feed phase illumination efficiency

η_s is the spillover efficiency

η_b is the blockage efficiency

η_x is cross-polarization efficiency

η_r is the paraboloidal reflector efficiency, including amplitude and phase due to surface contour and surface reflectivity

η_h is the hyperboloidal subreflector efficiency

η_a is the efficiency due to alignment error

η_m is the feed mismatch or (VSWR) reflected energy efficiency

η_e is the feed network efficiency, including ohmic losses and interactive losses within the feed.

Additionally, a "beamwidth efficiency" term α is defined as the ratio of measured beamwidth to minimum possible beamwidth. This term is related to a number of the above efficiency terms; it provides an excellent figure of merit for antenna performance.

Each of these efficiency terms, their causes and effects as well as a derivation of their maximum possible values, will be discussed in the section dealing with the primary influencing factor of that term.

2.2.3 Antenna Geometry

The antenna specification requires a 3-db beamwidth of between 1 and 1.5 degrees. The beamwidth in a given plane of an antenna is given by

$$BW = \frac{58.5}{a} \frac{\lambda}{D} \text{ degrees} \tag{4}$$

The smallest possible beamwidth of a circular aperture is 58.5 degrees, assuming a uniformly illuminated aperture with no phase error or aperture blockage. At the center frequencies of the transmit (14.650 GHz) and receive (13.600 GHz) bands, a reflector diameter of 48 inches results in minimum beamwidths of 0.98 and 1.06 degrees, respectively. It was desirable for the purposes of this effort to use the maximum reflector diameter consistent with the required beamwidth due to the related effects on blockage efficiency and small (in terms of wavelengths) subreflector diameter*. Naturally, this results in the highest gain within the beamwidth limitation. The other parameter required to define the paraboloid is the focal length, F, or F over D ratio. To minimize the secondary spillover (Reference 7) past the paraboloid edges, a deep dish (small F/D) is desirable. The cross-polarized currents induced on a highly curved reflector leads to selection of a shallow dish (large F/D). The range of F/D values typically used is between 0.25 and 0.4. A variety of factors, including thermal distortion and packaging (compactness), are affected by the choice of F/D, but the criterion used for selection was primarily the effect on efficiency. (As will be shown later, the F/D selected on the basis of efficiency resulted in an excellent compromise of the other considerations.)

In order to achieve the increased efficiency benefits available through the use of the near-field multimode concept, a number of constraints must be imposed over and above those normally encountered in a typical Cassegrainian antenna design. These constraints consist primarily of fixed relationships between horn/subreflector spacing, horn flare angle, subreflector included angle,

*In general, 1 degree is considered to be the maximum beamwidth for which the use of a Cassegrainian reflector system is justified.

etc., which must be maintained to achieve the desired illumination and blocking characteristics. An attempt was made to determine an analytical expression to optimize these parameters, but the formulation rapidly became too unwieldly to be of practical use. Therefore, an iterative approach was adopted, in which a "best estimate" set of parameters was used to develop an initial design for which illumination and blockage characteristics were determined. Then deviations from the original parameters, both singly and in combination, were input in an iterative process to determine the resulting effects. In this way, visibility was maintained within the process so that the result of any particular change could be tracked.

After a large number of iterations, a set of parameters and resulting characteristics were obtained which were deemed optimum. These parameters, if varied in any manner, yielded characteristics less desirable than those obtained with the optimum set.

The antenna geometry utilized in the design procedure is shown in Figure 1, and a definition of the terms is given in Table 1.

Table 1

DEFINITION OF CASSEGRAINIAN TERMS

Paraboloid		Hyperboloid	
D	paraboloid diameter	d	hyperboloid diameter
F	paraboloid focal length	f	hyperboloid focal length
ϕ_o	paraboloid half angle	p	hyperboloid axial length
K	F/D ratio	α	hyperboloid half angle
ρ	polar coordinate of parabolic surface	M	hyperboloid magnification
		e	hyperboloid eccentricity
Feed		a	hyperboloid equation constant
h	total feed aperture	B	linear blockage ratio
s	feed/subreflector spacing	μ	focal ratio
l_h	horn phase center/ aperture spacing		
θ	horn flare angle		

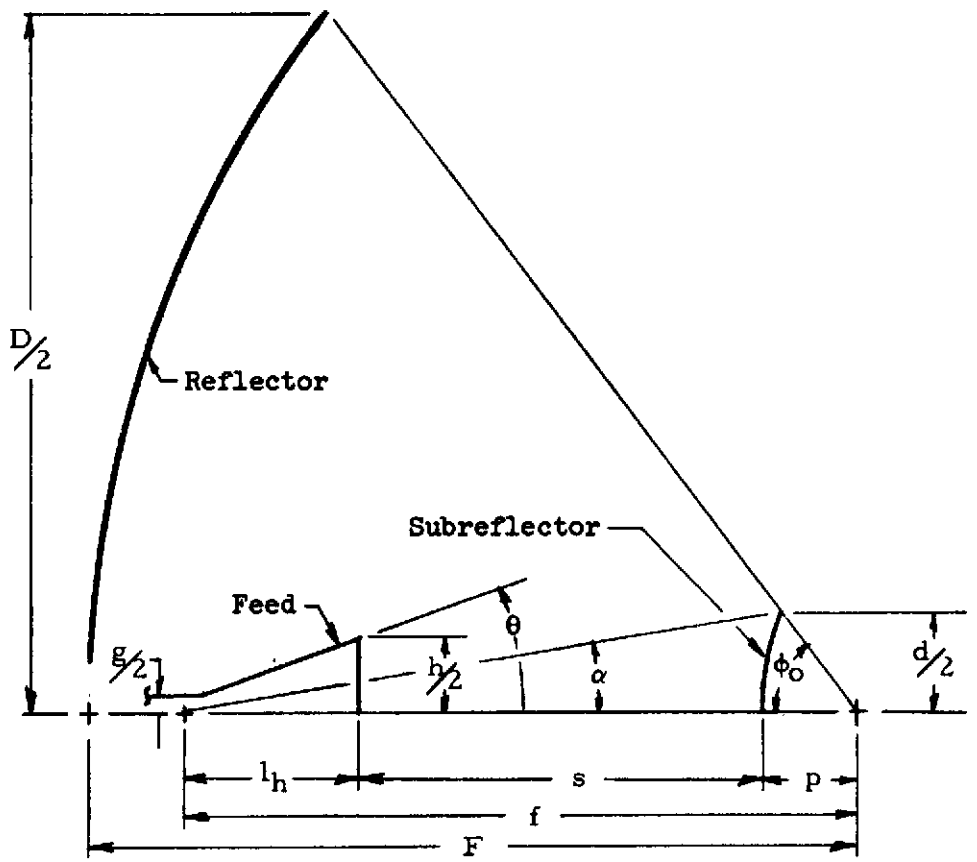

Fig. 1 Cassegrainian Geometry

A survey of pertinent published literature indicates the existence of a major unanswered question pertaining to near-field feeds (References 8 and 9, for example). The issue involves the nature of the phase characteristics in the near field of an aperture. It can be shown that, within the approximation of geometric optics, the near field of an aperture is collimated and planar (i. e., of uniform phase) over the dimension of the aperture. Indeed, the collimation properties are the basis of the increased efficiency of near-field feeds. Such a uniform phase condition would require a parabolic subreflector. On the other hand, much of the near-field design effort has been based on considering the phase characteristic to be spherical, as it would be from a point-source feed. In this instance, a hyperboloidal subreflector would be required. It is quite possible that these two views are compatible, in that separate feed horn (and therefore "phase center") locations may exist which would provide equal performance with either form of subreflector. Some empirical data obtained tend to indicate such compatibility. A combined analytical and experimental effort should be performed in order to resolve this question, but was considered to be beyond the scope of the present contract. In any case, the phase measurements made on the current feed network design indicated a spherical phase front symmetrical about a unique phase center (see Section 2. 2. 4. 3), and the design proceeded on that basis and utilized a hyperboloidal subreflector.

The systematic design process followed to determine the antenna design follows. The parameter values shown in the calculations are the final values resulting from the iterative process and used in the hardware design.

$D = 48.00$ in. (fixed)

$F = 14.500$ in. (limited variable)

$K = F/D = 0.3021$

$\phi_o = 2 \tan^{-1} (D/4F) = 79.22$ degrees

$d = 6.30$ in. (variable)

$B = d/D = 0.131$ The linear blockage ratio is usually chosen for minimum blockage of the feed and hyperboloid combination. On the near-field design, this ratio involves additional considerations. For maximum

spillover efficiency, the subreflector diameter should be as large as permissible, the horn and subreflector should be of comparable size, and in order to minimize blockage, the effective blockage area of feed and subreflector should be equal. d and h are two of the most important variables in the iterative process.

h = 3.577 in. (variable)

ℓ_h = 4.688 in. (estimated) This value for location of the horn phase center was based on previous horn measurements. The phase center was assumed to be 1/5 the distance from horn throat to apex. Measurements on the current horn determined the phase center to be approximately 1/4 the distance from the throat to the horn aperture, resulting in a value for ℓ_h of 3.250 inches which in turn moves the feed away from the subreflector, since the horn phase center must be placed at the forward focus of the hyperbolic subreflector. This feed location proved fortuitous in that it left room for the polarizer, which had not been considered in this phase of the design, without substantially increasing the blockage area.

α = 13.50 degrees (variable)

θ = $\alpha/0.85$ = 15.88 degrees Optimum near-field subreflector illumination occurs for $\theta \sim \alpha/0.85$, so that the subreflector included angle is slightly less than the feed horn flare angle.

$$M = \frac{1}{4K} \operatorname{Ctn} \alpha/2 = 6.992$$

$$e = \frac{M+1}{M-1} = 1.334$$

$$\mu = \frac{B}{2K} (\operatorname{Cot} \phi_o + \operatorname{Cos} \alpha) = 0.946$$

$$f = \mu F = 13.720 \text{ in.}$$

$$a = \frac{f}{2e} = 5.143 \text{ in.}$$

$b = 2\sqrt{e^2-1} = 4.539$ in.

$p = \sqrt{2^2+b^2}-2 = 1.717$ in.

$s = f-\ell_h-p = 7.315$ in. Reference 10 shows that the feed/subreflector spacing may be as great as $d^2/2\lambda$ without incurring significant loss. Larger spacings cause the efficiency to decrease rapidly. Using the lowest frequency of 13.500 GHz with a wavelength of 0.875 inch, which corresponds to the worst case, the maximum allowable spacing, Smax, is given by

$$Smax = \frac{d^2}{2\lambda} = 7.317 \text{ in.} \quad (5)$$

An approximation to the resulting aperture blockage is given by

$$A'_{block} \approx 1.025 \left(\frac{Fh}{s+p}\right)^2 = 33.8 \text{ in.}^2 \quad (6)$$

This blockage approximation was used to evaluate the results during the iterative design process.

Figure 2 shows one aspect of the results obtained during the iterations. The data are plotted in terms of S/Smax versus A'_{block}, with variable parameters of h, d, and α given in that order. These three parameters, coupled with ℓ_n and f (which itself depends on several other variables) were adjusted to find the combination which provided the minimum A'_{block} without exceeding Smax. The resulting antenna geometry is shown in Figure 3.

The actual combined blockage of feed and subreflector is given by

$$A_{f+s} = 4\left[\frac{R^2}{2}(\theta_i - \mathrm{Sin}\theta_i) + (h')^2\right] = 34.69 \text{ in.}^2 \quad (7)$$

where $R = d/2$, h' is the projected blockage aperture of the feed (as shown in Figure 3) and θ_i is the angle of intersection of the feed and subreflector blockage, as shown in Figure 4.

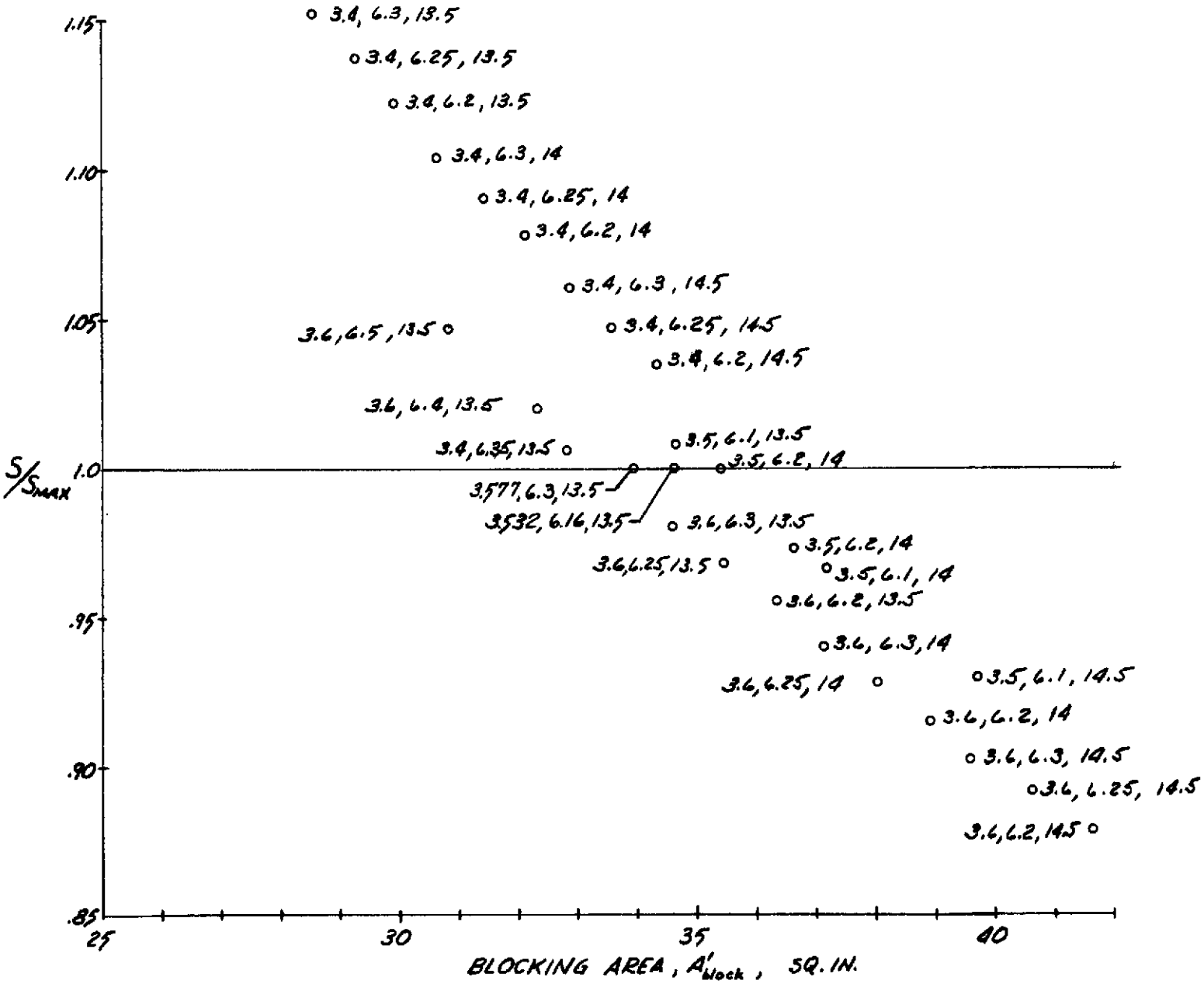

FIG. 2 ITERATION RESULTS

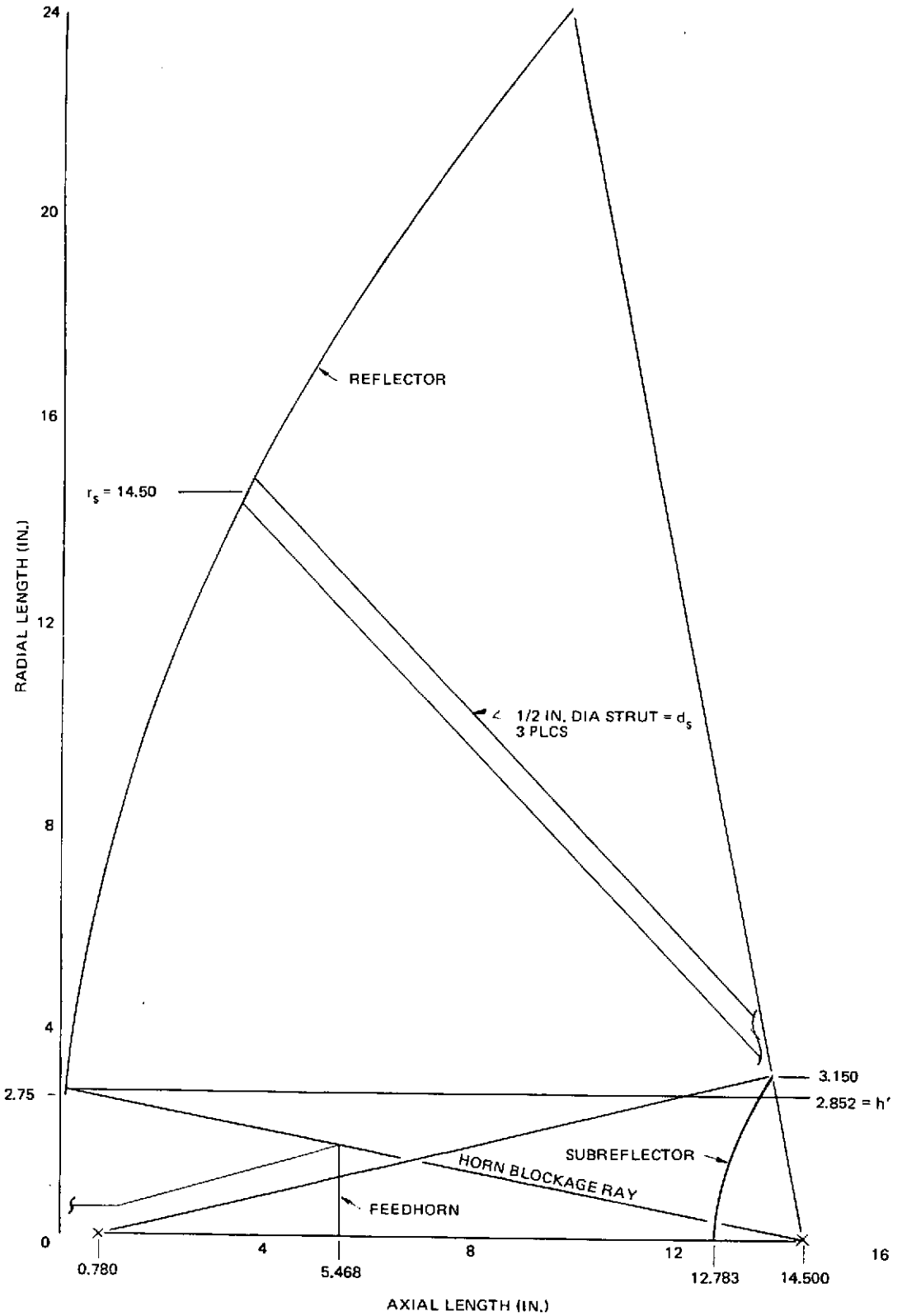

Figure 3. Antenna Design

The blockage created by the subreflector support struts is determined by calculating the strut projected area multiplied by an approximate factor which accounts for illumination taper effectivity:

$$A_{struts} = 3\left[(r_s - r_o)\, d_s\right] \times 0.67 = 3\left[(14.50-3.15)0.5\right] \times 0.67 = 11.35 \text{ in.}^2 \tag{8}$$

The total blockage area is then given by

$$A_{block} = A_{f+s} + A_{struts} = 46.04 \text{ in.}^2$$

To determine the effects of blockage, the total blockage area is converted to an effective blocking diameter, d', which is 7.66 inches. Then

$$B_{eff.} = \frac{d'}{D} = 0.1595 \tag{9}$$

The blockage gain loss is given by

$$G_b = -20 \log\left(1-2B_{eff.}^2\right) = 0.454 \text{ db} \tag{10}$$

which results in a blockage efficiency of 90 percent.

The final, as-delivered configuration is shown in Figure 5. The major difference between it and that of Figure 3 is in the location of the feed and inclusion of the polarizer. Also, the diameter of the subreflector support struts was increased from 0.5 to 0.75 inch. Table 2 provides a summary of the blockage characteristics for both linear and circular configurations. It can be seen that inclusion of the circular polarizer substantially increases the blockage area and reduces the blocking efficiency by approximately 5 percent. Any subsequent iteration of this design would account for the polarizer from the outset, and the blocking efficiency of the circular polarized configuration would be substantially improved.

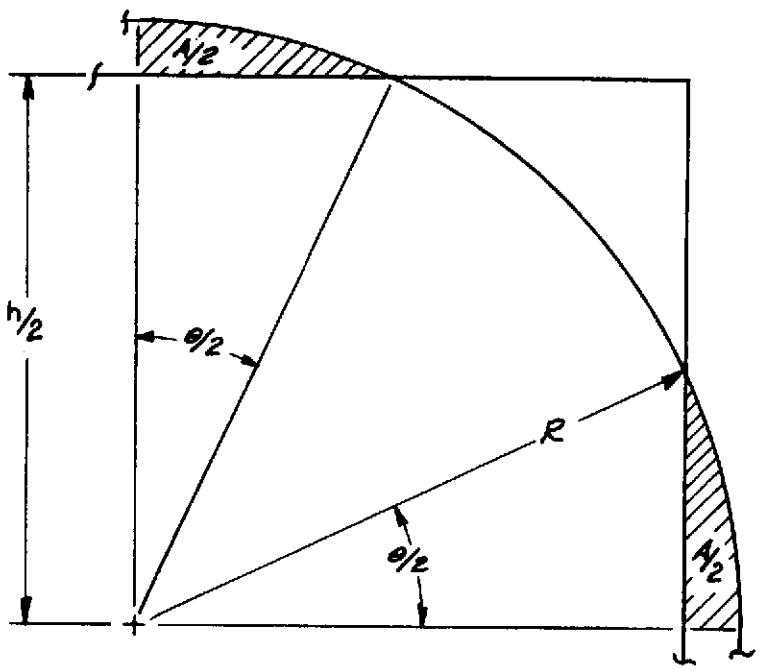

FIGURE 4 BLOCKAGE GEOMETRY

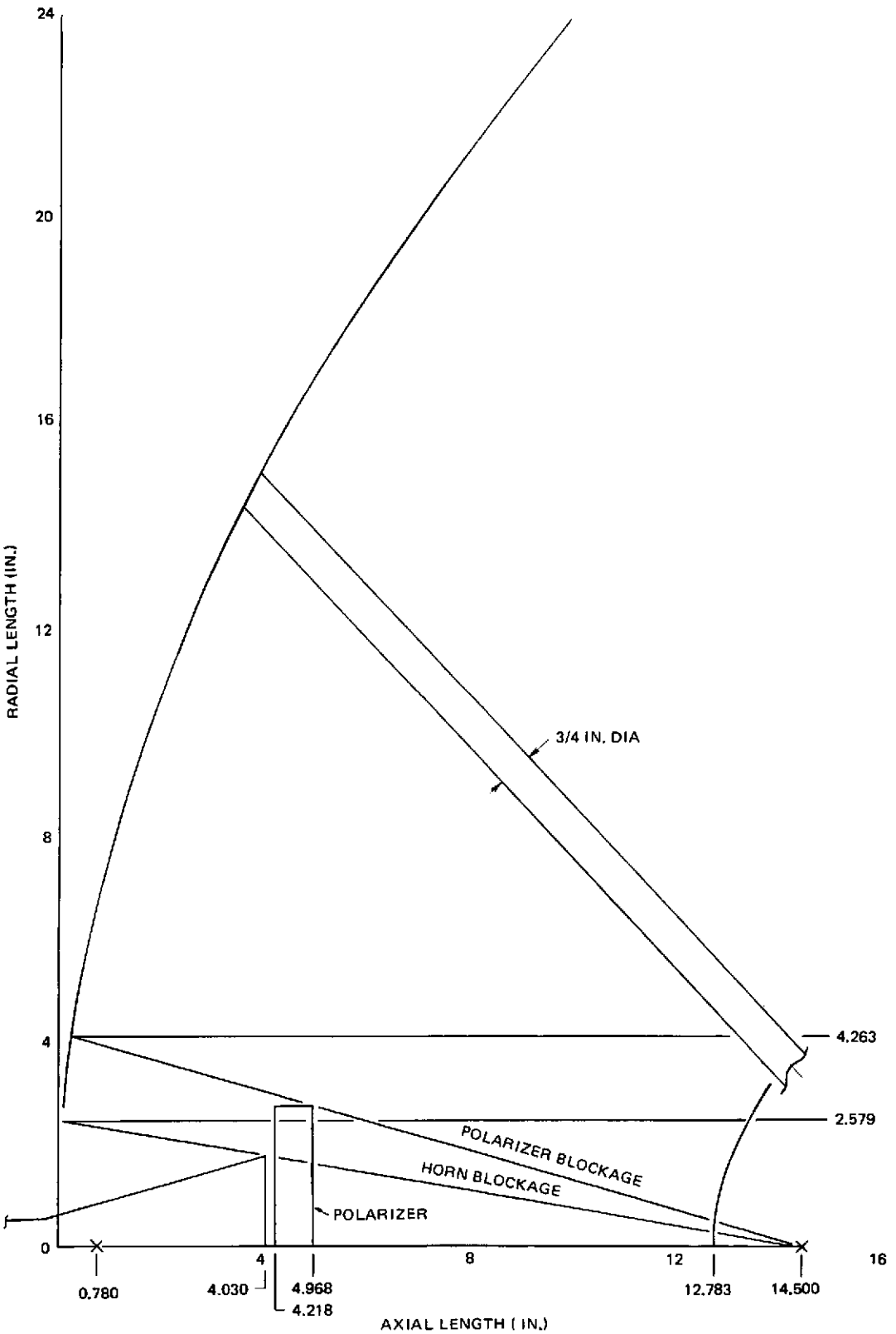

Figure 5. Final Antenna Geometry

Table 2

BLOCKAGE SUMMARY

		Design	Final	
		Linear	Linear	Circular
A_{f+s}:	Horn and Subreflector (in.^{2})	34.69	32.23	57.09
A_{strut}:	Struts (in.^{2})	11.35	17.49	15.81
A_{Block}:	Total Area (in.^{2})	46.04	49.72	72.90
d':	Effective Blocking Diameter (in.)	7.66	7.96	9.63
B_{eff}:	Blockage Ratio	0.160	0.166	0.201
G_b:	Gain Loss (db)	0.454	0.491	0.730
η_b:	Blockage Efficiency (%)	90.0	89.3	84.5

Parameters of the final antenna assembly are given in Table 3. It should be noted that the only parameter concerning the feed horn so far determined is the horn aperture, h. The remaining feed parameters will be developed in the following section. The parabolic equation defining the reflector surface is given by

$$y^2 = 4Fx \tag{11}$$

while the hyperbolic equation for the subreflector is given by

$$x = a\left[\left(1+\frac{y^2}{b^2}\right)^{1/2} - 1\right] \tag{12}$$

A number of factors affecting the analysis and achievable characteristics of the near-field Cassegrainian configuration are dependent upon the size of reflector surfaces in terms of operating wavelengths. Much of the analysis used in the design process is based upon minimum values of 12λ for the subreflector and 100λ for the reflector. Using diameters less than the minimum

Table 3

ANTENNA PARAMETERS

Reflector Diameter 48.00 in.
Reflector Focal Length 14.50 in.
F/D 0.302
Parabolic Equation $y^2 = 58x$
Feedhorn Aperture 3.577 in.
Feedhorn/Subreflector Spacing 7.32 in.
Hyperboloid Diameter 6.30 in.
Hyperboloid Focal Length 13.72 in.
Hyperboloid Equation $x = 5.1431 \left[\left(1 + \frac{y^2}{4.5393^2} \right)^{1/2} - 1 \right]$

diameters results in a lessening of achievable efficiency. Both the subreflector and reflector diameters of 7.2λ and 55λ are substantially less than the minimum values. Effects of smaller diameters result primarily in greater spillover and edge diffraction, smaller allowable horn/subreflector spacing, Smax, and greater blockage ratio. An increase of reflector diameter, therefore, would increase several of the efficiency factors. As will be seen in the results achieved, performance degradation due to this cause appears to be slight, except for the effective blockage ratio.

2.2.4 Feed Network

The advantages to be derived from the use of a near-field multimode feed are threefold:

A. Beam-collimating properties of the near field, which results in reduced spillover and, hence, higher efficiency.

B. Beam-shaping properties provided by use of higher-order waveguide modes in addition to the basic lowest order mode. Utilization of these modes allows tapering of the normal $TE_{1,0}$ mode E-plane aperture distribution to increase illumination efficiency, as well as providing odd-order modes for development of monopulse tracking signals.

C. Simplicity and compactness of the single-aperture feed which decreases aperture blocking, and lack of much of the usual sum and difference monopulse circuitry and its associated losses and bandwidth limitations.

The first two of these advantages are shown graphically in Figure 6, which depicts the typical efficiency improvement available through the use of this type of feed (Reference 8).

In this section, the analysis and development of the near-field multimode feed are described.

2.2.4.1 Near-Field Characteristics

It has been shown (Reference 11) that the energy radiated from an aperture of diameter D is constrained within an imaginary "tube" of the same diameter as the transmitting aperture out to a distance of approximately $D^2/2\lambda$. In this radiating near field, which extends from several aperture diameters to somewhat less than $2\ D^2/\lambda$, the radiated energy is collimated; i.e., it does not exhibit the typical $1/R^2$ spatial dispersion encountered in the far field. The radiation pattern is essentially a reproduction of the electric field distribution within the aperture, and the intensity is cyclically variable with axial distance. By placing the feed horn with respect to the subreflector such that the subreflector fills the collimated beam, spillover efficiency can be significantly increased over that obtainable with more conventional feeding methods, and by tailoring the distribution in the aperture, optimum illumination of the subreflector can be achieved for high illumination efficiency. The inclusion of capability of propagation and coupling of odd-order modes also provides the difference patterns for monopulse tracking. These functions are all performed in a single-aperture feed which is inherently broadband and relatively small for reduced aperture blocking.

The aperture efficiency which can be achieved with near-field feeds has been determined by Fresnel field analysis (Reference 10). The portion of interest of the curves of efficiency degradation, α, versus horn/subreflector spacing

as determined in that analysis are given in Figure 7. The spacing is given in terms of Raleigh distance, or fraction of $2D^2/\lambda$, and curves are presented for several aperture distributions.

Aperture distributions used in the Fresnel analysis are of the form

$$E = B + (1 - r)^k \tag{13}$$

where r is the normalized aperture radius $\rho/_{d/2}$, and B is the illumination edge-taper, or pedestal height. The curve labeled η_{max} represents the maximum efficiency that can be achieved with a given set of parameters as determined by Kay's (Reference 12) formula for the ratio of maximum power transmitted through a given area of space to the total power radiated from the aperture. The curves of Figure 7 have been normalized to η_{max} in Figure 8, which gives the aperture efficiency achievable for the various distributions*. The general characteristic of these curves outside the region shown is a rapid asymptotic approach to the well-established far-field values as the spacing is increased beyond 0.4. For the two tapered distributions shown, which are indicative of all reasonable aperture tapers, the efficiency decrease attendant to spacings greater than 0.2 to 0.25 illustrates one factor leading to the establishment of an Smax of $d^2/2\lambda$. It is interesting to note that uniform illumination (B=K=0) does not provide maximum efficiency in the near field as it does in the far field.

As will be shown in the following section, the aperture distribution obtained with the multimode horn has approximately a 10-db edge taper and a pattern shape very nearly given by $E = 0.462 + (1 - \gamma)^{0.75}$, with a spacing equivalent to 0.29 in Figure 8. Using a linear extrapolation for the value of K with the curve given for the 10 db, K = 1 distribution, an illumination efficiency of 92 percent is determined. If the spacing had been $d^2/2\lambda$ as mandated in the system design process of the previous section, an illumination efficiency of approximately 96 percent would have been obtained. This is a fairly drastic example of the Smax criteria.

*The efficiency term as used here includes only that due to illumination distribution and spillover at the subreflector.

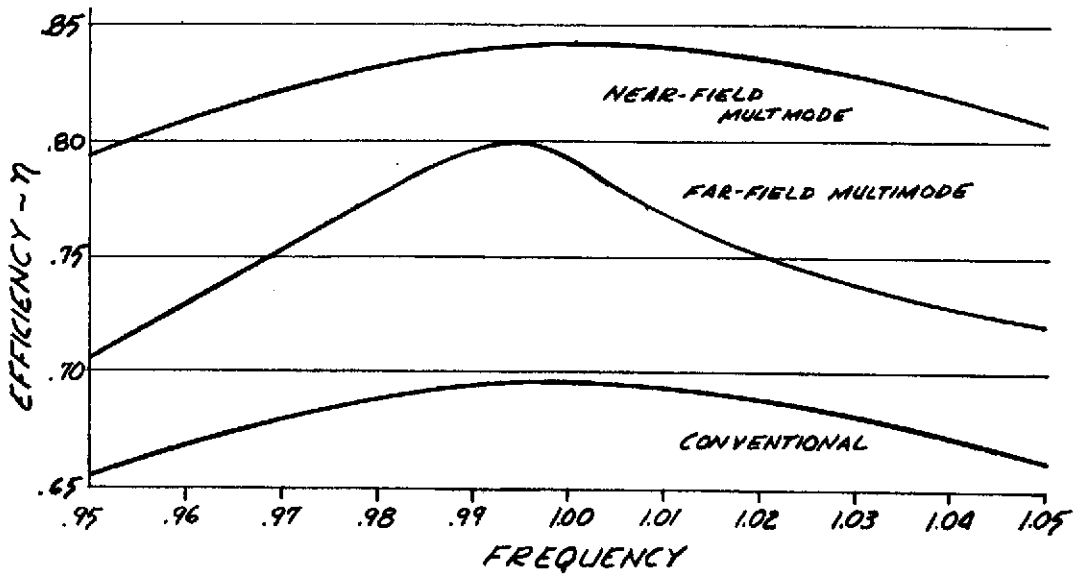

FIG. 6 RELATIVE FEED EFFICIENCY

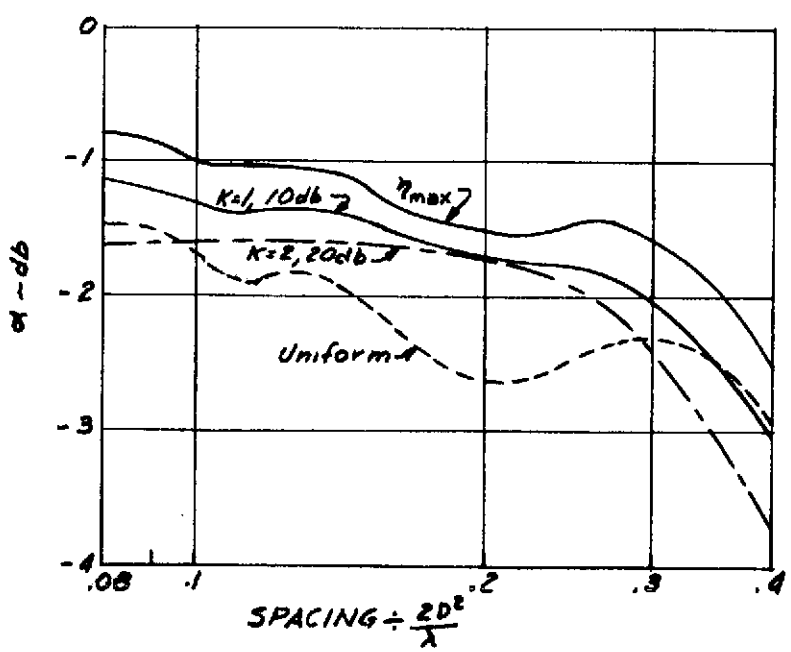

FIG 7 EFFICIENCY DEGRADATION

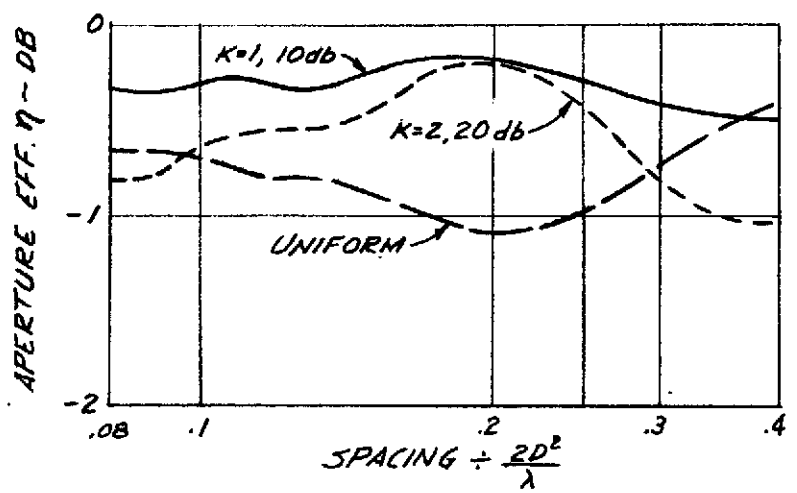

FIG. 8 NEAR-FIELD EFFICIENCY

2.2.4.2 Multimode Feed Network

The use of the near-field technique for improved feed efficiency requires that the feed pattern be rotationally symmetric and virtually sidelobe free. These feed attributes are extremely beneficial in any feed system, but are perhaps more critical in the near-field arrangement and must be achieved if the expected efficiency is to be attained. A dominant-mode (single, lowest-order) feed does not possess these characteristics; beamwidths are considerably different in the E and H planes, and sidelobes are relatively high, particularly in the E-plane.

Typical near-field dominant-mode horn patterns are shown in Figure 9, where the rotational asymmetry and E-plane pattern distortions are quite evident. The aperture field distribution which gives rise to the radiation patterns are shown in Figure 10. It can be seen that the H-plane distribution is tapered in a cosinusoidal fashion, producing the narrow and smooth H-plane pattern, while the E-plane distribution is uniform, providing the broader, scalloped pattern with appreciable sidelobes.

The E-plane aperture distribution can be modified by the addition of higher-order modes to closely approximate the H-plane distribution, resulting in the desired pattern rotational symmetry and elimination of sidelobes. This can be accomplished with a variety of mode configurations, constrained only by the required waveguide cross section for mode propagation and waveguide lengths for appropriate mode phasing. The simplest mode configuration which accomplishes the desired effect requires the inclusion of $TE_{1,2}$ and $TM_{1,2}$ modes in addition to the $TE_{1,0}$ mode. As will be seen from the pattern results achieved, this combination provides adequate pattern-shaping capability, and inclusion of higher-order modes would only increase feed dimensions and complexity. The combination of $TE_{1,2}$ and $TM_{1,2}$ modes, designated the $LSE_{1,2}$ mode, are shown in Figure 11, as are the results of combining the $LSE_{1,2}$ mode with the $TE_{1,0}$. One characteristic of LSE type modes which must be considered is that there is an axial component of the field which does not exist with the more common TE and TM type modes. This will be discussed in a later section.

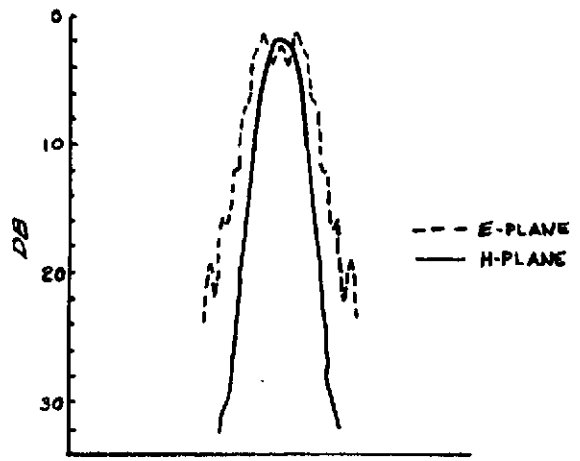

Fig. 9 Dominant Mode Near-Field Patterns

Fig. 10 Dominant Mode Aperture Distributions

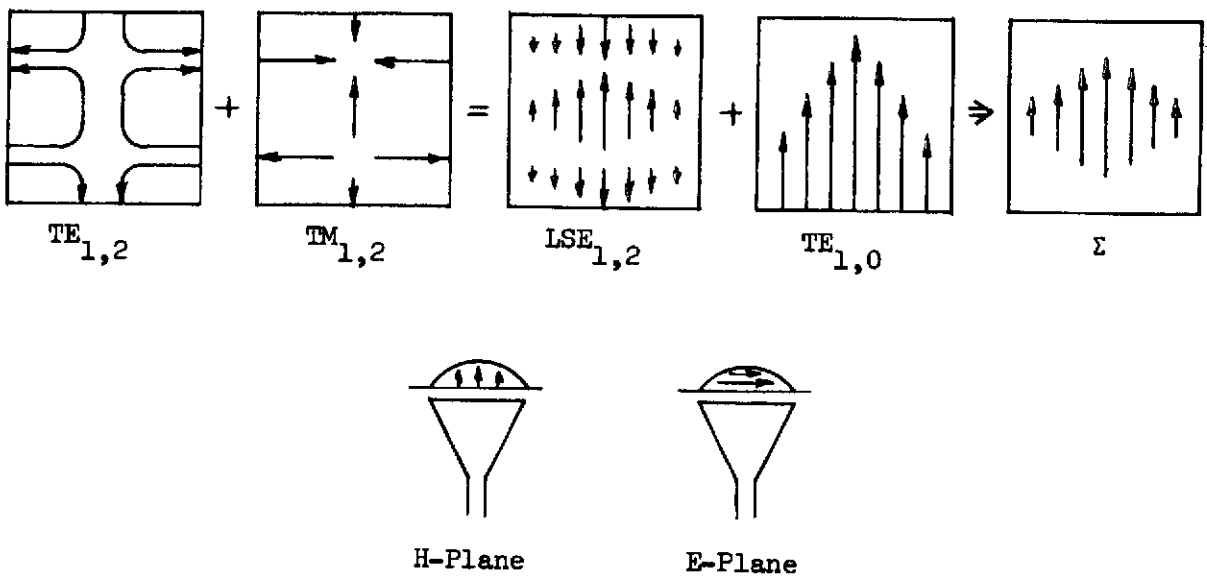

Fig. 11 Mode Development

The feed pattern distribution of the combined $TE_{1,0}$ and $LSE_{1,2}$ modes is given by (for θ - polarization)

$$E_{1,0\ +\ 1,2}(\theta,\phi) = \mathrm{Cos}\frac{\pi\phi}{2\phi_{max}} + \beta\ \mathrm{Cos}\left[\frac{\pi\phi}{2\phi_{max}}\right]\left[\mathrm{Cos}\ \frac{\pi\theta}{\theta_{max}}\right] e^{iX} \tag{14}$$

where β is the ratio of $LSE_{1,2}$ to $TE_{1,0}$ mode amplitudes and X is the phase difference between the modes at the feed aperture. Calculated E-plane patterns, for several values of β, are shown in Figure 12, along with an H-plane pattern for comparison. It can be seen that $\beta = 0.5$ results in an almost perfect match between E- and H-planes. The patterns of Figure 12 were calculated on the basis of an optimum phase relationship between the modes. Figure 13 shows the effects of varying the relative phase, X, on pattern shape. X is given in terms of length of the waveguide phasing section. Relatively small changes of guide length are seen to produce fairly large alterations of pattern shape. Variations of guide length at a fixed frequency are analogous to variations of frequency with a fixed length when considering phasing characteristics, so that the data of Figure 13 are indicative of feed bandwidth. Converting the phase length variable to frequency results in a bandwidth expression, as depicted in Figure 14. Naturally, bandwidth of the feed is limited by the overall length of the feed, and Figure 14 was based on an estimate of the length required for inclusion of monopulse tracking couplers. A nontracking feed, or one which required less space for tracking couplers, would exhibit considerably greater bandwidth.

A generalized block diagram of the multimode feed network is shown in Figure 15. The orthomode transducer is a convenient way of introducing two orthogonal linearly polarized fields into a single waveguide, while maintaining excellent isolation between the two. All desired polarization within the feed network is linear, with circular polarizations being developed by a network external to the feed. For purposes of discussion, the internal fields of the transmit channel will be considered as horizontally polarized, and the receive channel as vertical. The output of the transducer is a square guide, and the square shape is maintained throughout the remainder of the feed so

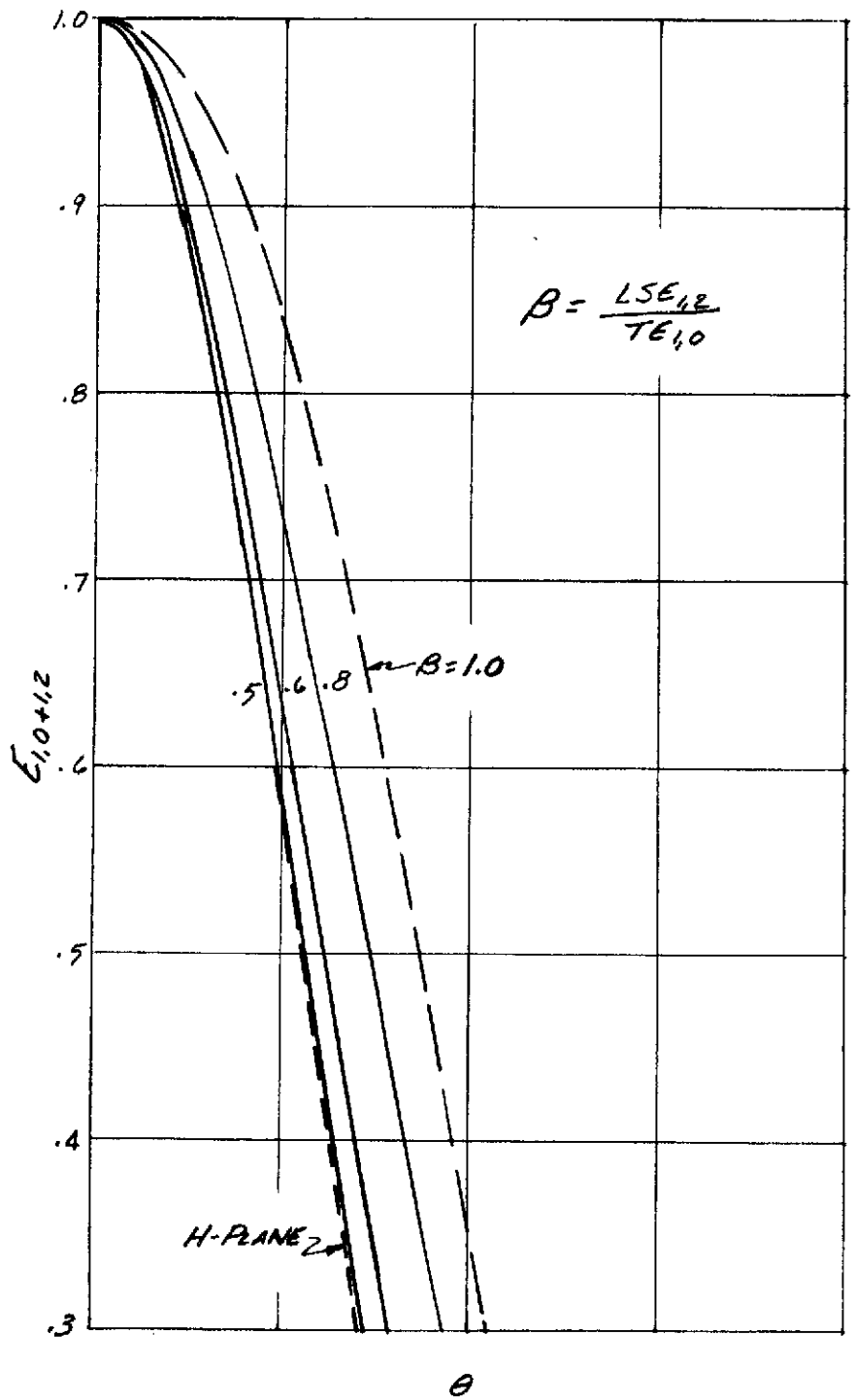

EFFECTS OF MODE RATIO - β

FIG. 12

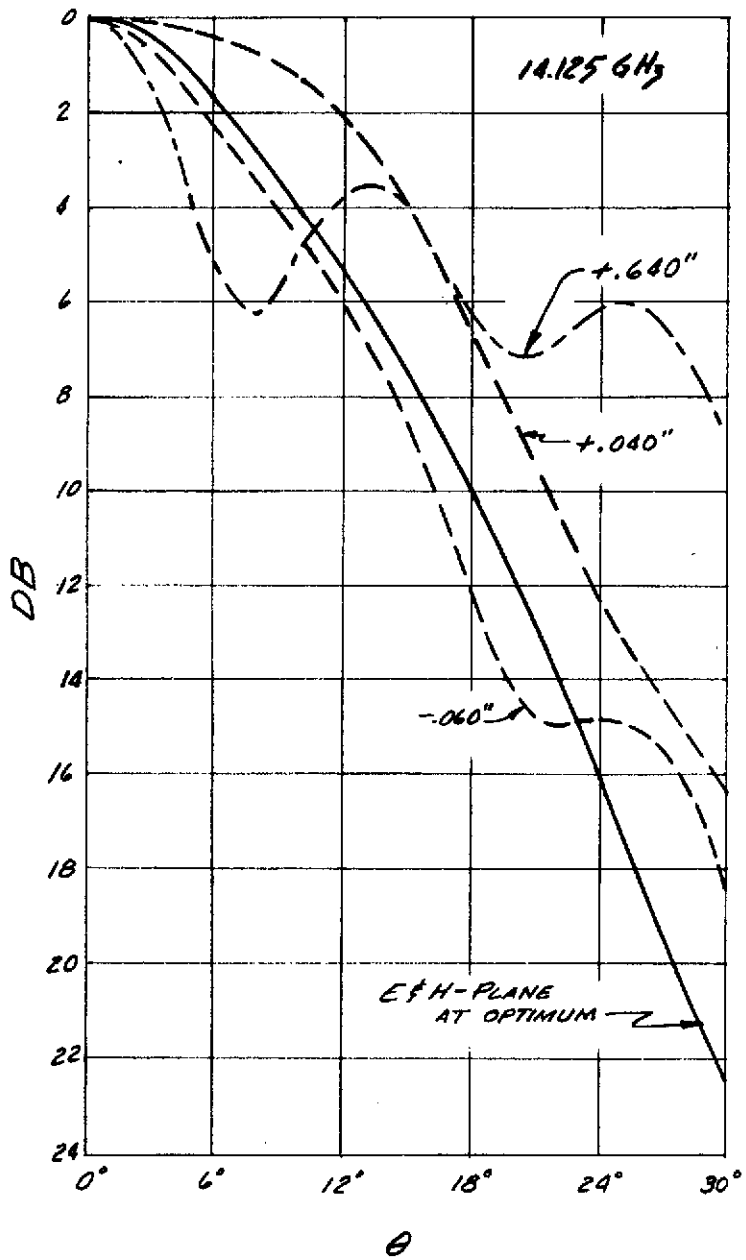

PHASING LENGTH EFFECTS

FIG. 13

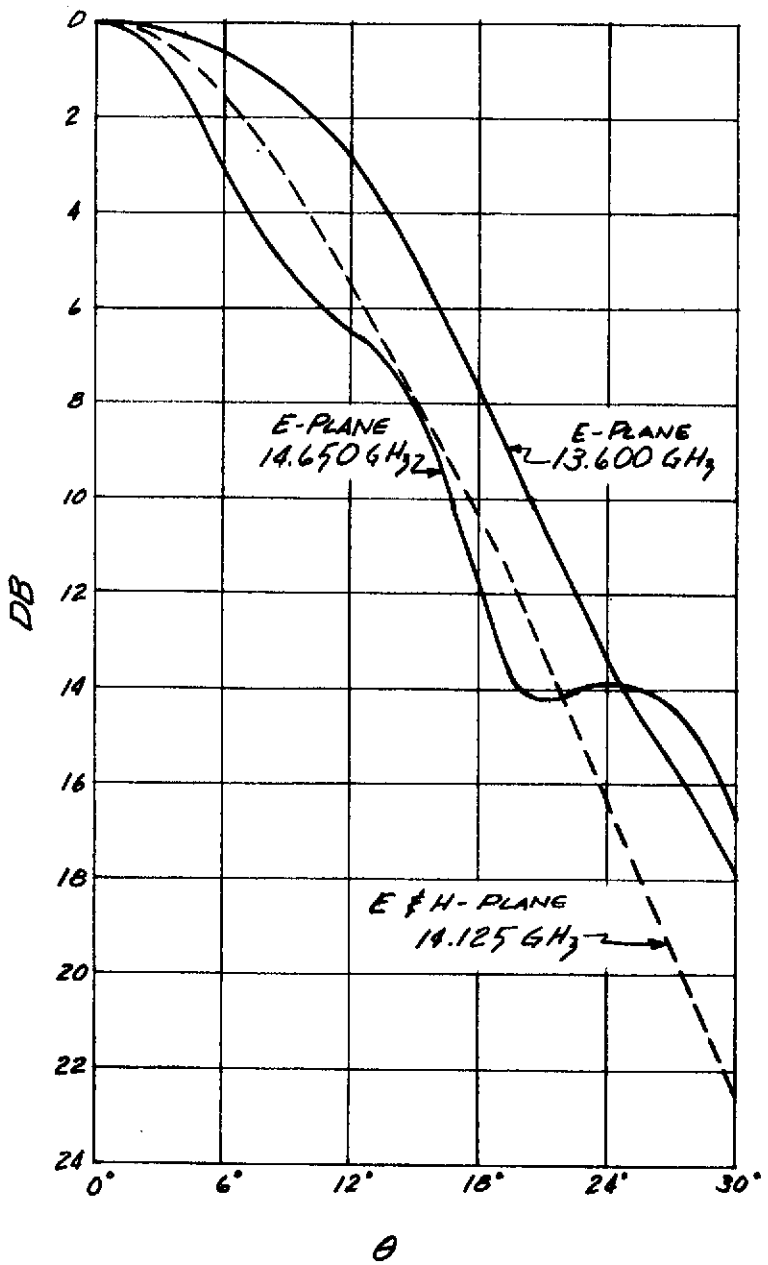

SUM PATTERN BANDWIDTH

FIG. 14

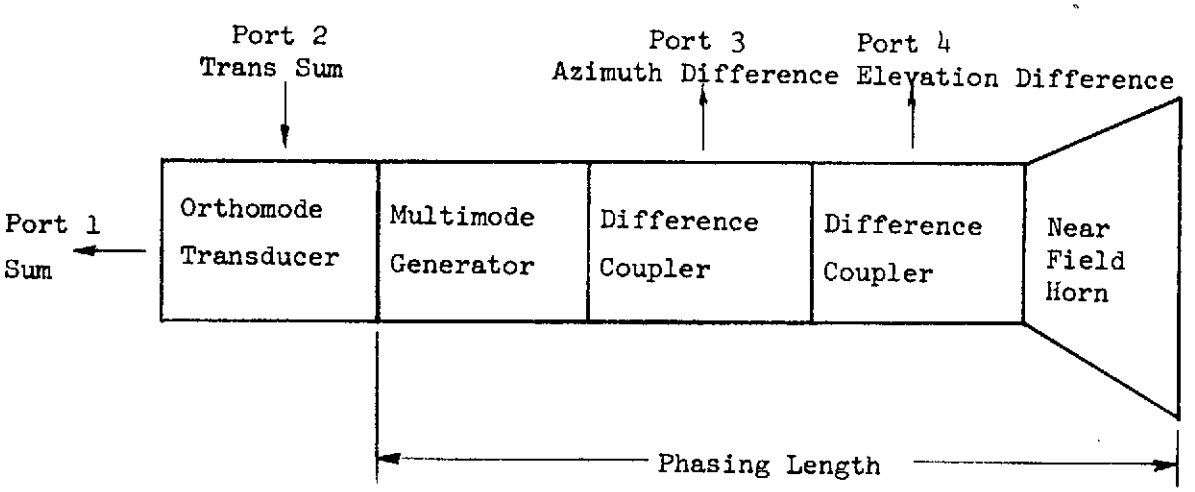

GENERALIZED FEED NETWORK

Fig. 15

that orthogonal linear polarizations are available for polarization flexibility and transmit-receive isolation. The square dimensions have now been determined for each end of the feed network; the horn aperture, h, was determined in the system geometry design, and the network entrance, a_1, by the aperture of a commercially available orthomode transducer, which in this case is 0.562 inch.

Generation of the $LSE_{1,2}$ mode is conveniently accomplished with a symmetrical step discontinuity in guide size. A Fourier analysis of the fields in the region of the discontinuity (Reference 13) provides a method of determining the ratio of the mode amplitudes, the results of which are shown in Figure 16. Generation of the desired value of $\beta = 0.5$ requires a step discontinuity ratio a_2/a_3 of 0.78.

Constraints on the implementation of the discontinuity ratio are governed by the waveguide size required for propagation of desired modes and cutoff of any higher order undesired modes. The desired modes include the $TE_{1,0}$, $TE_{1,2}$, and $TM_{1,2}$ for the sum patterns and $TE_{2,0}$, $TE_{1,1}$, and $TM_{1,1}$ for the tracking functions. Included in the lowest-order undesired modes, those whose cutoff wavelength is only slightly greater than the cutoff of desired modes, are primarily the $TE_{2,2}$, $TE_{3,0}$*, $TE_{1,3}$, and $TM_{1,3}$. The cutoff wavelength λ_c for modes m, n in a square waveguide of dimension a is given by

$$\lambda_{c_{m,n}} = \frac{2}{\sqrt{\frac{m^2 + n^2}{a^2}}} \tag{15}$$

and is shown in Figure 17. The minimum value of a_3 is determined by $\lambda_{c_{1,2}}$ at the longest wavelength of interest (0.875 inch), and is 0.975 inch. The maximum size, set by $\lambda_{c_{2,2}}$ at the shortest wavelength (0.801 inch), is 1.132 inches.

*In some applications, the $TE_{3,0}$ mode may be beneficial. It may be used to widen the peak of the H-plane beamwidth appreciably, which results in a smaller value of k in Equation (13) and somewhat greater possible aperture efficiency. However, inclusion of this mode increases complexity and severely limits bandwidth to the extent that its use did not appear appropriate for this application.

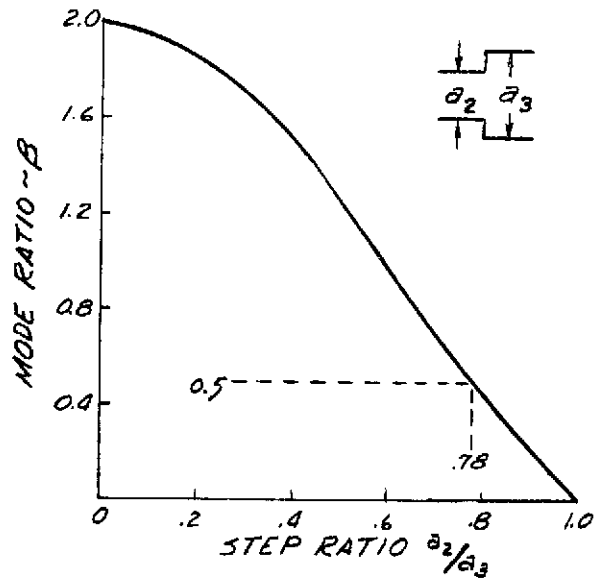

FIG. 16 MODE GEOMETRY

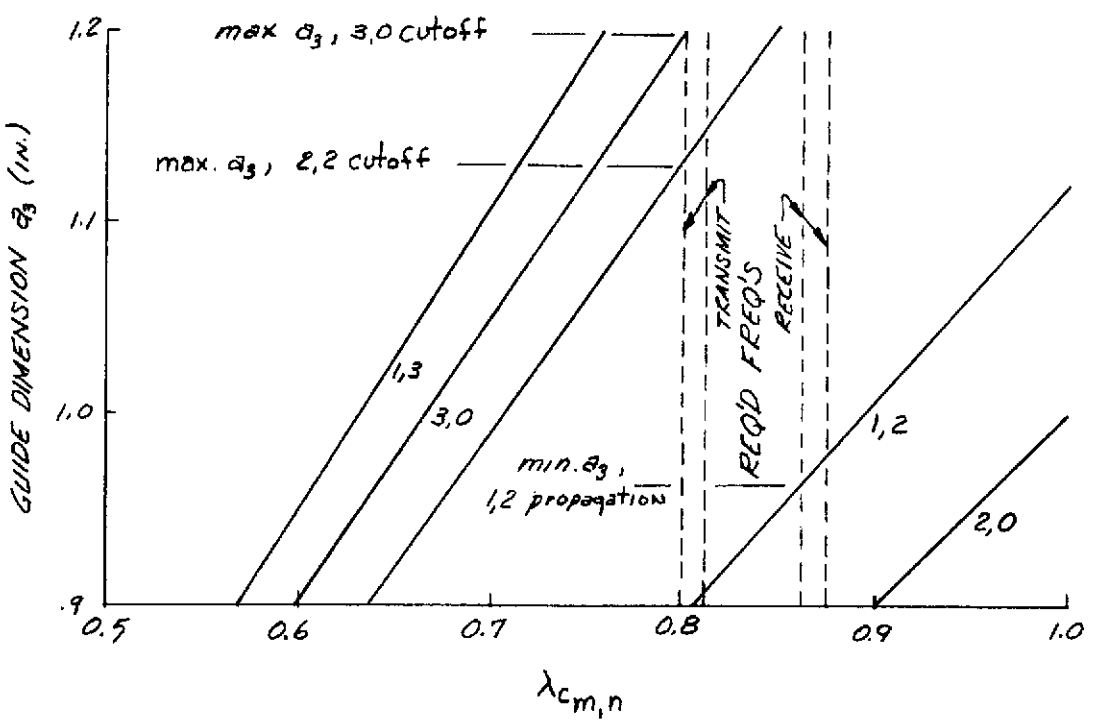

FIG. 17 λ_c vs. a_3

Several factors affect the selection of guide dimension a_3 within the range determined above, but in the interest of bandwidth and attenuation the largest possible value (a_3 = 1.132 inches) was selected. A tapered waveguide section is then required between the exit aperture of the orthomode transducer (0.562 inch) and the horn throat (1.132 inches). Then $a_2 = 0.78a_3 = 0.884$ inch.

The remaining feed network dimension to be determined is the length of the phasing section required to achieve the proper, in-phase condition of the 1,0 and 1,2 modes at the horn aperture. Ignoring for the moment any relative phase shift introduced by the tracking couplers, the relative phase velocity of the 1,0 and 1,2 modes in the square guide and horn sections of the network must be determined. The phase shift $\Delta\phi_{m,n}$ incurred as the mode traverses the horn is given by the expression

$$\Delta\phi_{m,n} = \frac{\pi\sqrt{m^2+n^2}\,\mathrm{Cot}\theta}{2}\left[\sqrt{\left(\frac{2h}{\lambda\sqrt{m^2+n^2}}\right)^2 - 1} - \sqrt{\left(\frac{2a_3}{\lambda\sqrt{m^2+n^2}}\right)^2 - 1}\right.$$
$$\left. - \tan\sqrt{\left(\frac{2h}{\lambda\sqrt{m^2+n^2}}\right)^2 - 1} + \tan\sqrt{\left(\frac{2a_3}{\lambda\sqrt{m^2+n^2}}\right)^2 - 1}\right] \qquad (16)$$

$\Delta\phi$ values for the 1,0 and 1,2 modes, and the relative phase shift between them, $\Delta\phi_{1,0-1,2}$, are given in Table 4 for the previously determined network parameters. At the center frequency, there is a phase difference of 180 degrees, with approximately a ±10 degree variation at the band edges. This requires a relative phase shift of 90 degrees within the phasing section to achieve the desired mode phase characteristics, since the two modes originate in phase quadrature at the step discontinuity, with the higher-order mode lagging the fundamental mode.

Length of the required phasing section can then be determined from

$$\Delta\phi_{1,0-1,2} = 2\pi z\left(\frac{1}{\lambda g_{1,0}} - \frac{1}{\lambda g_{1,2}}\right) = 90^\circ \qquad (17)$$

Table 4

HORN INSERTION PHASE

Mode	Frequency (GHz)				
	13.5	13.7	14.125	14.55	14.75
1,0	1726.3°	1753.1°	1810.1°	1867.0°	1893.8°
1,2	1535.2°	1565.8°	1630.3°	1694.0°	1723.8°
$\Delta\phi_{1,0-1,2}$	191.1°	187.3°	179.8°	173.0°	170.0°

where z is the length of guide between the step discontinuity and horn. The two shortest values for z are 0.575 and 2.874 inches. These values neglect any insertion phase characteristics of the tracking mode couplers which must be located in this region. These effects and the required length adjustments were determined experimentally. While it is desirable to keep the network as short as possible for bandwidth consideration, it was doubtful that the shorter length could physically accommodate the necessary tracking ports or allow for their insertion phase.

Figure 18 summarizes the analytically derived dimensions for the feed network, which were used for fabrication of a prototype unit. The prototype was built in modular form, as shown in Figure 19, so that the length of the phasing section and location of the tracking couplers could be varied in an optimization process. In the foreground are shown several configurations of tracking couplers which were investigated during this development, and which are described in Section 2.2.4.4.

2.2.4.3 Phase Center Determination

Precise determination of the feed horn phase center is required for proper location of the horn in the near-field Cassegrainian geometry in order to achieve maximum efficiency. Substantial difficulty was encountered in obtaining the phase measurements with the desired degree of accuracy, primarily due to the use of commercial antenna positioners and inclement weather. Extensive modification and realignment of the positioners satisfactorily overcame the mechanical problems, and resulted in an estimated phase measurement accuracy of approximately ±2 degrees. Measured phase countours

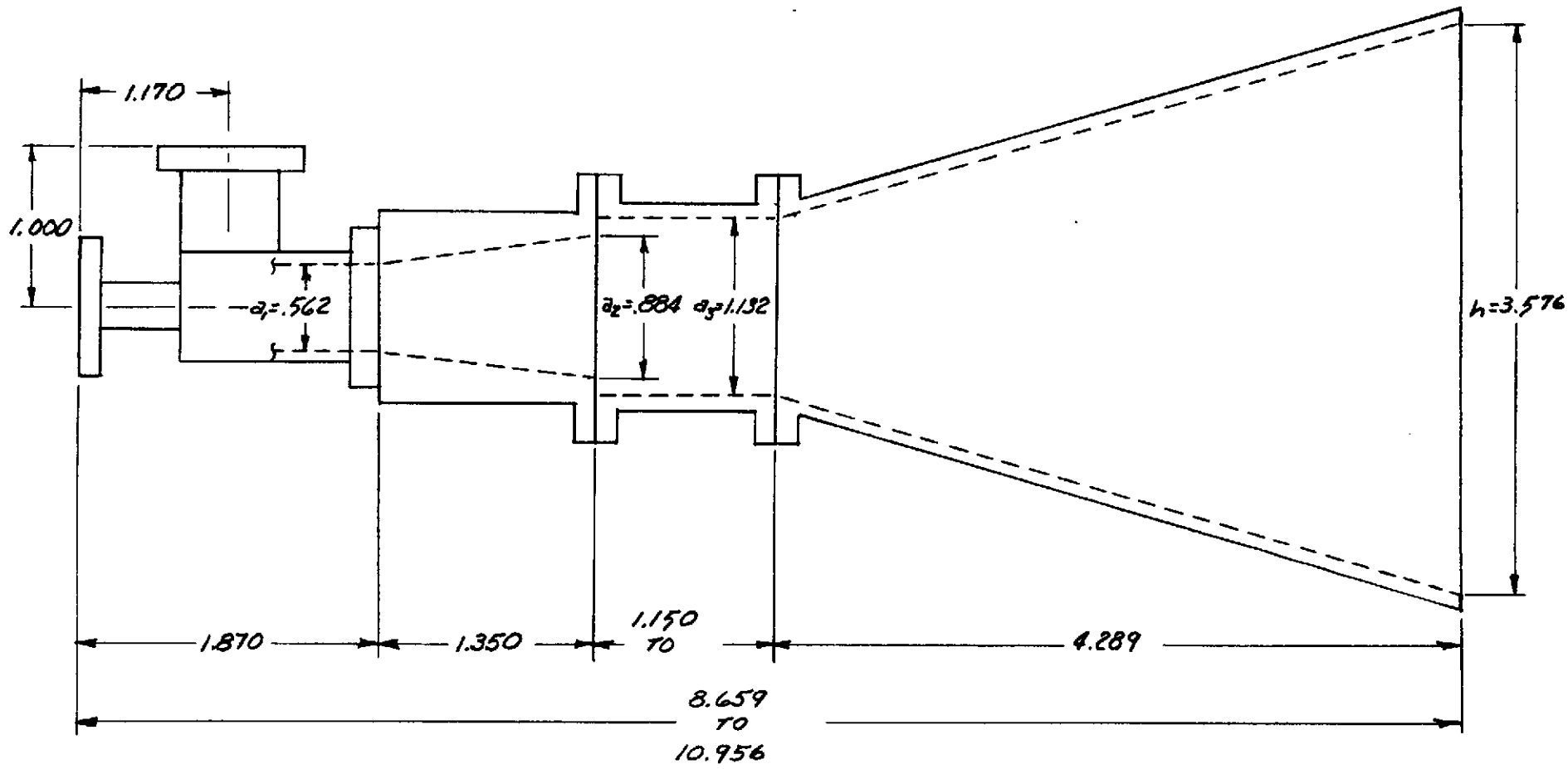

FIG. 18 PROTOTYPE FEED NETWORK

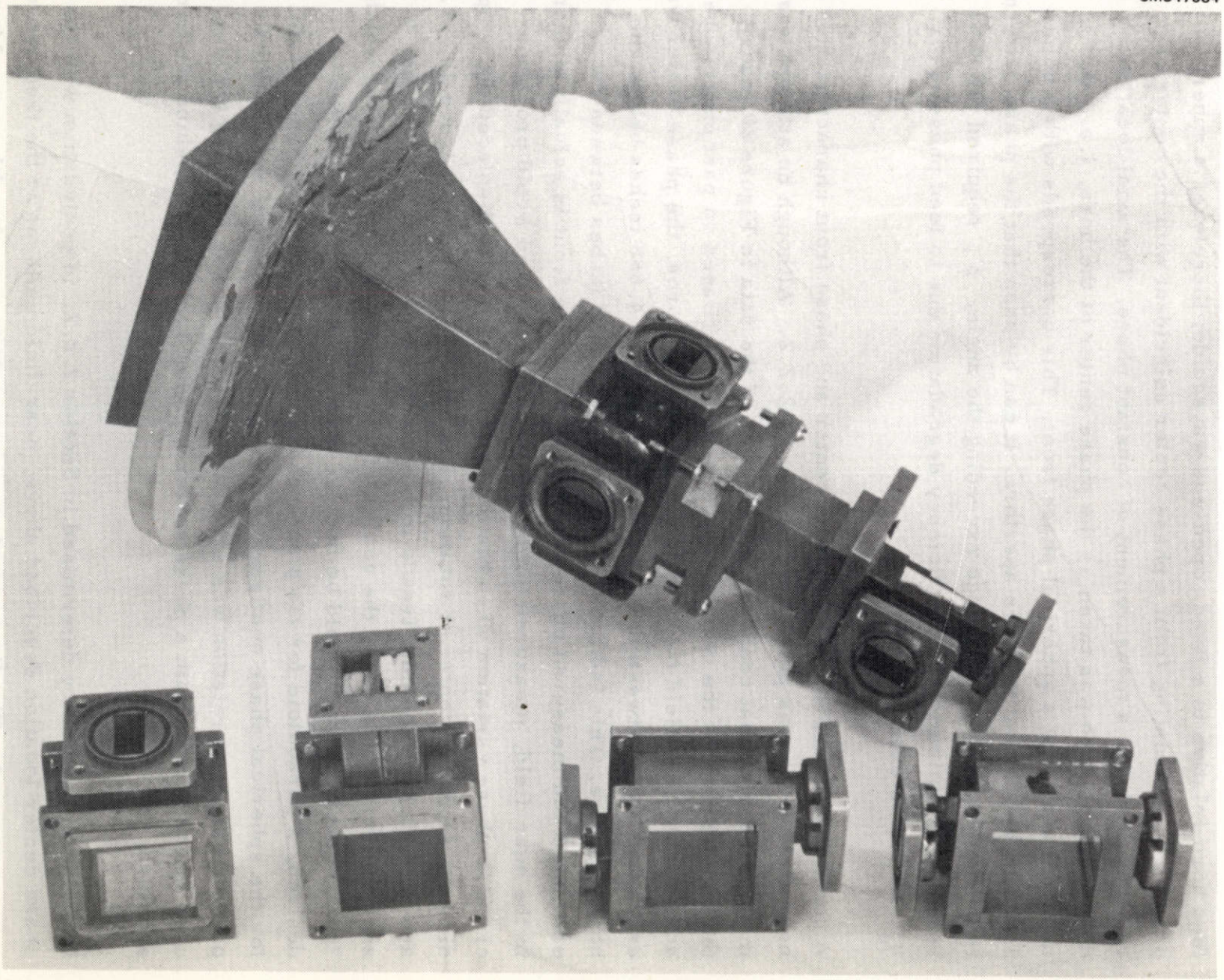

Figure 19. Prototype Feed Network

versus axial displacement with respect to center of rotation is shown in Figure 20. The near-field measurements were performed by rotating the feed horn relative to a fixed, open-end waveguide; therefore, a spherical phase front emanating from a phase center coincident with the center of rotation produces a measurement of constant phase. The axial location designated as zero was taken as the phase center of the horn, i.e., the apparent center of a spherical phase front. This corresponds with a point 3.250 inches behind the horn aperture. It can be seen that the phase pattern is quite spherical over a range exceeding the angle, α, required for subreflector illumination, and efficiency degradation due to feed phase error, η_{ϕ}, should be extremely small.

A conflict in interpretation of phase center and phase front characteristics for near-field feeds was pointed out in Section 2.2.2. Although no attempt was made to resolve that conflict, examination of the data in Figure 20 leads to the conclusion that the two views are compatible. Based on past experience and previous far-field measurements on similar horns, the phase center was estimated to be between the horn throat and apex, 4.688 inches behind the horn aperture. This indicates a difference of 1.438 inches between the estimated and measured phase centers. If the phase front is actually planar in the near field, measurement by the technique utilized would produce circular phase variation when the phase center is axially displaced the proper distance from the center of rotation. The extreme curves of Figure 20, -1.5 and +1.1 inches, indicate trends toward such circular phase variations. If such is actually the case, the conflict does not exist and the choice of which "phase center" to use would be decided by which type of subreflector is desired, a paraboloid for the planar phase configuration or an hyperboloid for the spherical phase configuration. As previously stated, the spherical phase front interpretation was accepted and a hyperbolic subreflector was used in conjunction with a phase center location 3.250 inches behind the horn aperture.

Utilizing the geometry determined in Section 2.2.2, in conjunction with the phase center location described above, near-field patterns of the feed network were measured. The first set of measurements was made with no tracking couplers in the network so the data are comparable to values determined by

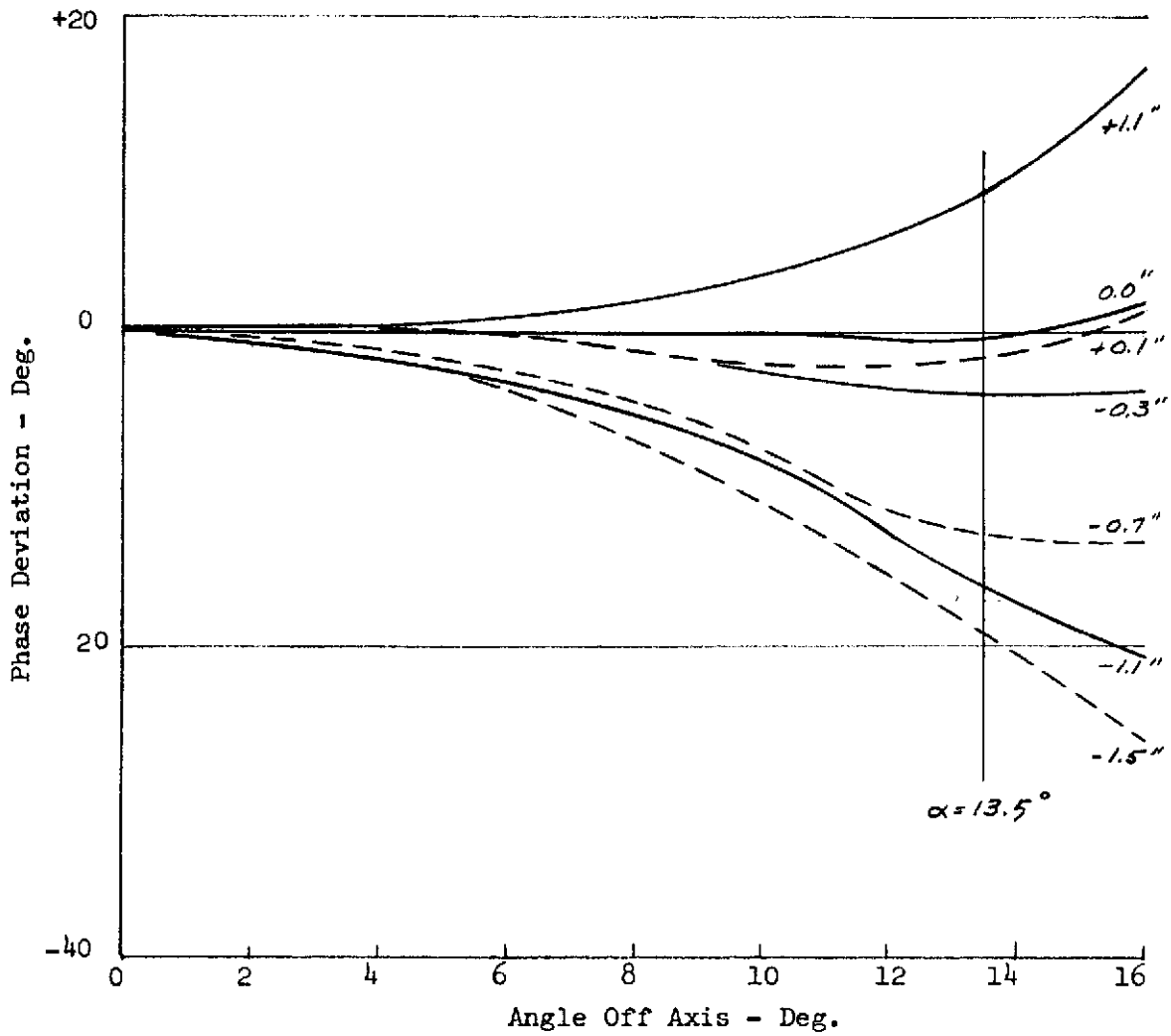

Fig. 20 Phase Center Determination

Equation (17). Results of these measurements are summarized in Figure 21, which shows the effects of varying the length of the phasing section on E-plane patterns of port 1. Assuming that the optimum-mode ratio, β, has been achieved, proper phasing length provides an E-plane pattern identical to the H-plane. The data of Figure 21 show the proper length to be between 2.70 and 2.85 inches; a linear interpolation of magnitudes at the subreflector edge indicate an optimum value of 2.80 inches. Insertion of this value for z in Equation (17) results in a phase shift of 78.5 degrees, which is considered excellent agreement with the analytically derived value. The 11.5-degree discrepancy is attributed to tolerances in waveguide dimensions, insertion phase of the horn, and discontinuities within the waveguide due to the modular elements utilized.

As discussed earlier, the tracking couplers will introduce phase shifts in the network which have so far been neglected and which will require adjustment of length of the phasing section for optimum performance. Therefore, the configuration of the tracking couplers must be determined before the network length can be finalized. It will be seen, however, that the relative insertion phase of the tracking couplers, particularly the $LSE_{1,1}$ coupler, is dependent on axial position of the couplers, while the optimum coupler location is also dependent upon overall length of the network, requiring extensive iterative measurements to determine the optimum configuration.

2.2.4.4 Tracking Couplers

Conventional monopulse tracking feeds use a four-horn cluster, or more complex equivalent, to derive the tracking function. The four horns separate the received signal into four parts from which two orthogonal angle tracking signals are developed in microwave summing and subtracting networks. It has been shown (Reference 14) that, in a suitably sized feed network, the odd-order (unsymmetrical) field distributions required for angle tracking are excited in any feed which is illuminated by an off-axis source. The two modes of interest for tracking are the $TE_{0,2}$ and the $LSE_{1,1}$ ($TE_{1,1} + TM_{1,1}$) modes. Each of these are lower order than the $LSE_{1,2}$ modes which the network was sized to accommodate for pattern shaping reasons, so the tracking modes will also exist in the network. The field distributions of the two modes are shown

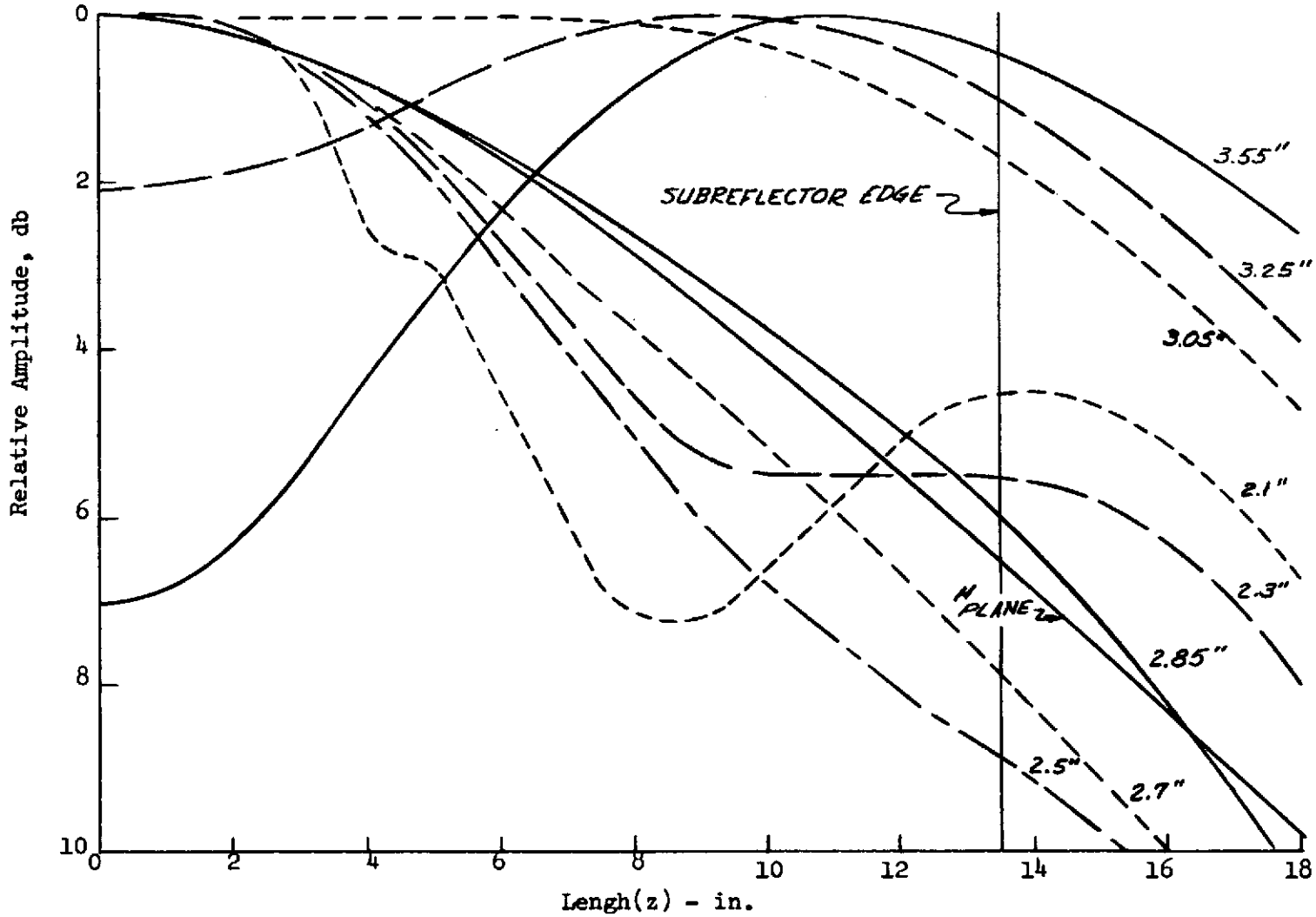

Fig. 21 Phasing Length Effects

in Figure 22. A variety of couplers would appear to be suitable for extraction of each of these modes. Shunt, or axially oriented, slots are the type most commonly preferred due to their lesser impact on the fields within the network as compared to series, or transverse, slots. Therefore, all original prototype designs utilized shunt coupling slots. Several of these coupling sections were shown in Figure 18. Consideration of the desired modes shown in Figure 22 would indicate minimal difficulty in satisfactorily coupling to those modes, but inclusion of the sum modes (Figure 10) which exist in both polarizations, and cross-polarized difference modes which may be excited due to illumination polarization, polarizer imperfections, or any discontinuity within the feed network, considerably complicate the issue. Also, it was determined early in the development process that axial location of the difference mode couplers was quite critical. This is to be expected, since the step discontinuity appears as a short circuit to all but dominant-order modes, and the higher modes all propagate at different velocities within the larger guide section, creating interference patterns among any of these modes which are coupled.

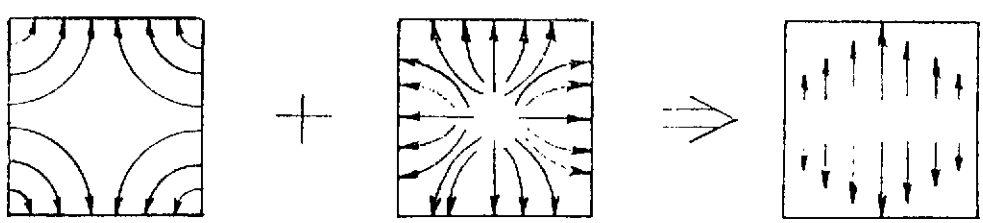

$TE_{1,1}$ $TM_{1,1}$ $LSE_{1,1}$

Elevation Difference

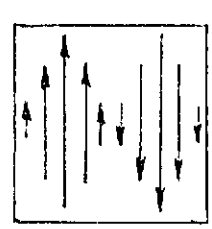

$TE_{0,2}$

Azimuth Difference

TRACKING MODE FIELD DISTRIBUTIONS

Fig. 22

The $TE_{0,2}$ coupler is reasonably straightforward. A dual, shunt-slot on the waveguide centerline, as shown in Figure 23, was utilized in the IRAD version of the feed network. This dual-slot configuration, connected through a hybrid tee, has the advantage of separation of the desired signals from any even-mode signals present. Even-mode signals are coupled to the unused and terminated port of the hybrid tee. Excellent azimuth difference plane patterns were obtained with this configuration; however, use of the dual slots, with the attendant requirement for the hybrid tee and interconnecting waveguides, considerably and unnecessarily increases the mechanical complexity of the device. Several of the couplers intended for use with the $LSE_{1,1}$ modes also provided satisfactory azimuth difference patterns when rotated 90 degrees from their normal position but these also required the undesirable combining hardware. The single-slot configuration of Figure 23 provides equally good difference patterns, as long as the slot is kept reasonably narrow and precisely on the guide centerline, and eliminates the need for combining hardware. The resulting difference pattern is shown in Figures 24 and 25. The digital contour plots, such as Figure 25, are maps of the radiated field over a solid angle, with field intensity shown in decibels. Taken in half-degree incremental steps (and occasionally in tenth-degree steps for very fine grain data), they proved extremely useful during the development effort, particularly for the $LSE_{1,1}$ coupler. These fine-grain data readily showed pattern perturbations which indicated undesirable mode coupling and which might have easily been missed with only principal plane or more widely spaced analog patterns. An indication of the axial-spacing dependence is shown in Figure 26. These data, taken with only the $TE_{0,2}$ coupler in the network, show the limits of the values of on-axis port 1 sum magnitude to port 3 azimuth difference peak ratios. The scatter of the data points was due to varying overall network length and frequency throughout the receive band. These data clearly show the requirement for careful location of the difference couplers. No discernible effects of this difference coupler on sum channel characteristics were found, other than a minor relative phase shift which requires only a change in length of the phasing section of the network.

Satisfactory performance of the $LSE_{1,1}$ coupler was considerably more difficult to achieve than was the case with the $TE_{0,2}$ coupler. The difficulties

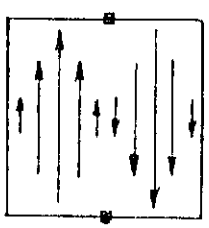

Dual Slot
(a)

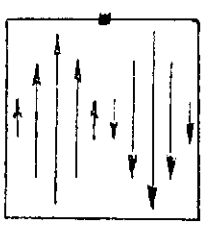

Single Slot
(b)

$TE_{0,2}$ DIFFERENCE COUPLERS

Fig. 23

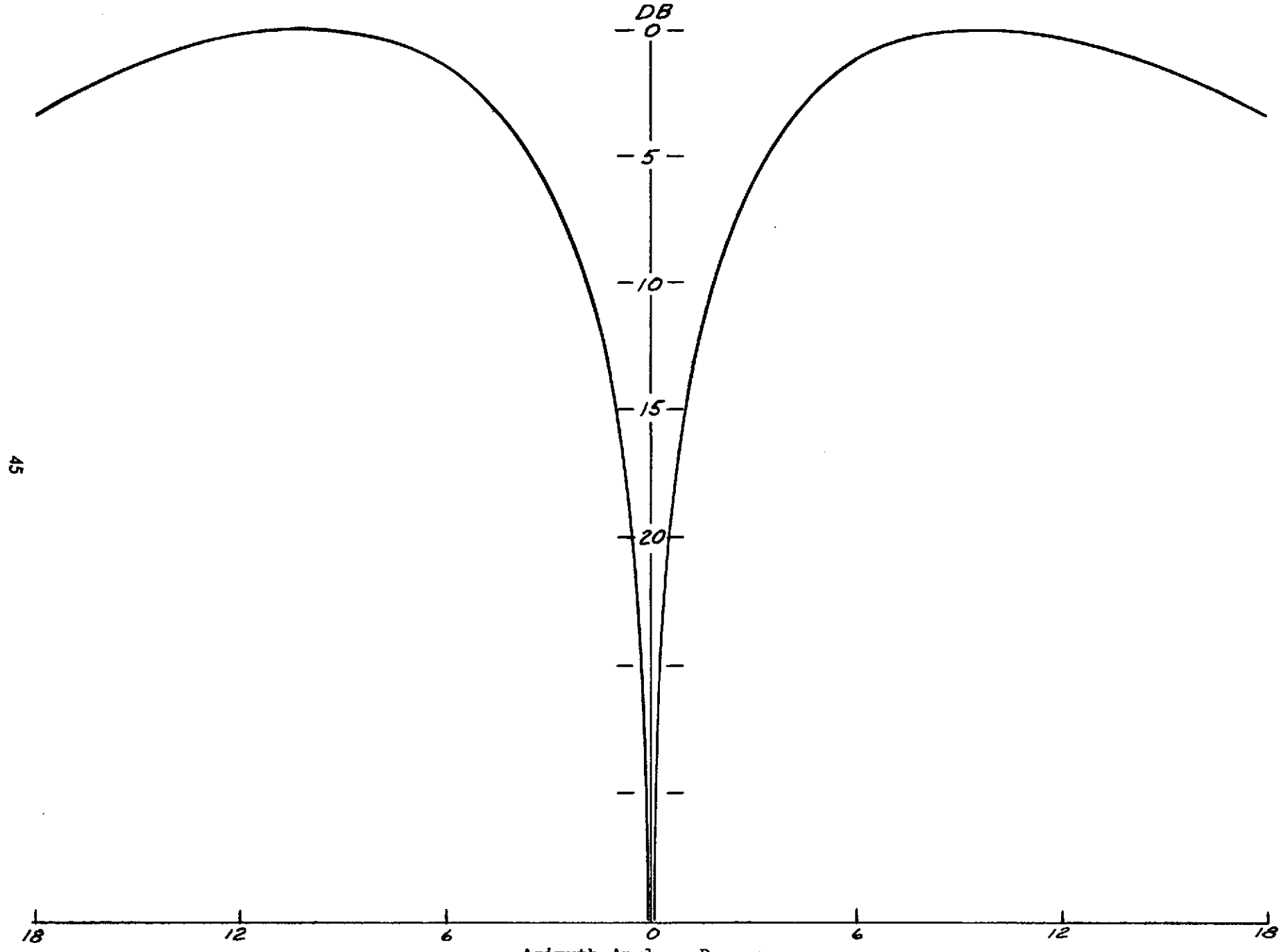

Fig. 24 $TE_{0,2}$ Difference Pattern

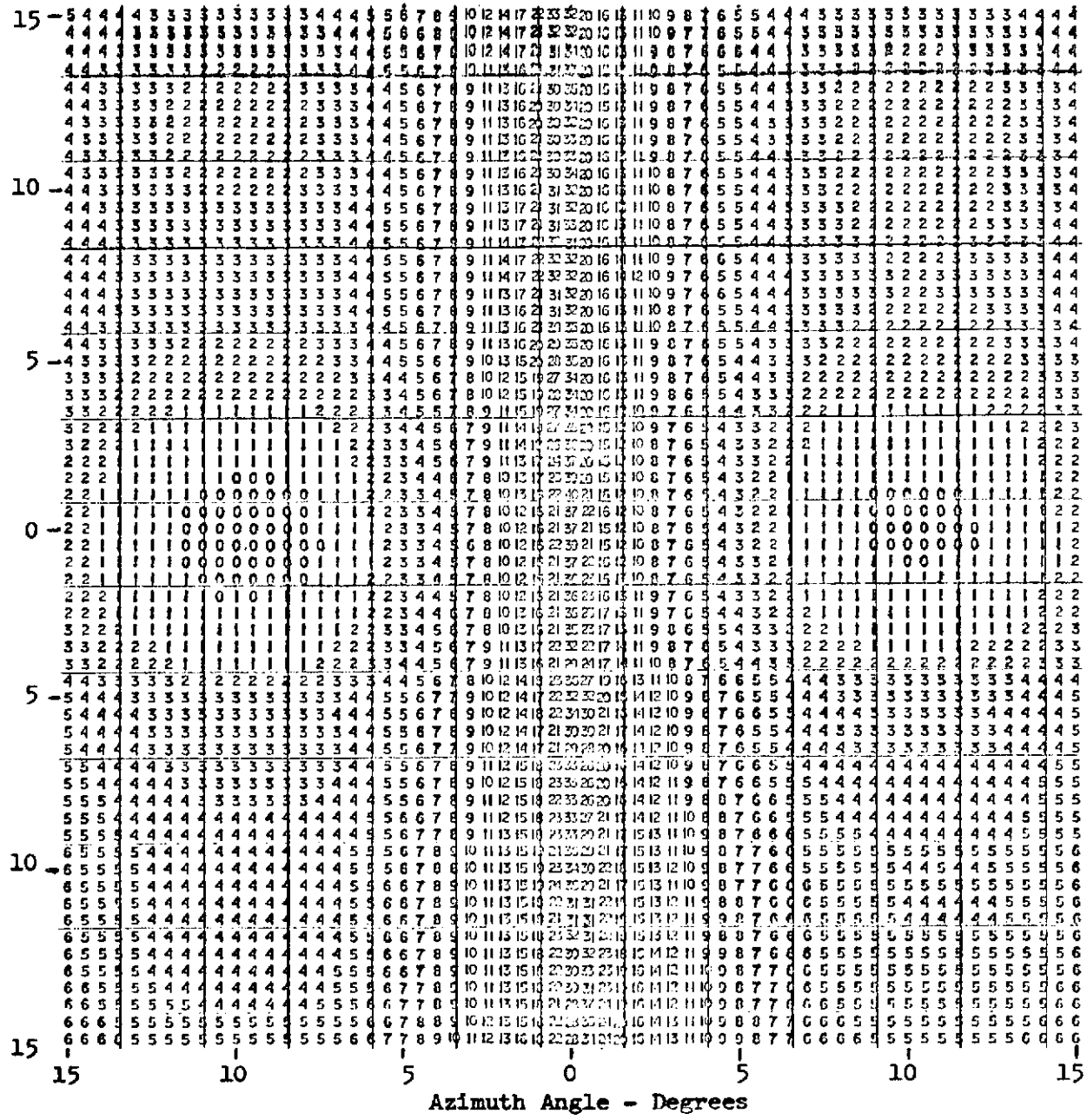

Fig. 25 $TE_{0,2}$ Difference Pattern

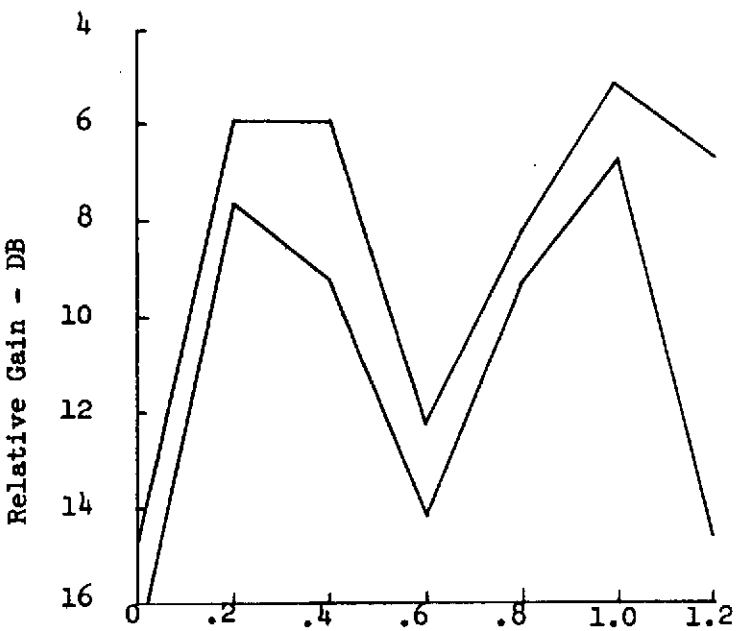

$TE_{0,2}$ COUPLER LOCATION

Fig. 26

encountered were due to the inability to find a coupler which responded only to the mode desired. The shunt-slot couplers investigated are shown in Figure 27. These couplers, together with several variations and combining networks, failed to produce the required difference patterns. Interaction with other modes and polarizations caused a variety of pattern characteristics which made the patterns unacceptable. An example of interaction of the $LSE_{1,1}$ and $TE_{0,2}$ modes with indications of weak coupling to 1, 0 and/or 1, 2 modes in a single coupler is shown in Figure 28. Four and even more, lobed patterns were commonly produced by the shunt couplers.

The hesitancy to adopt transverse slot couplers, as Figure 27c, for the $LSE_{1,1}$ mode was due to the fact that such slots couple equally well to the $LSE_{1,2}$ mode utilized in shaping of the sum patterns as they do the desired difference modes. This results in a strong dependency of both transmit and receive sum patterns on difference coupler properties.

Elevation-difference patterns obtained with the transverse slot coupler of Figure 27c combined through the H arm of an E-plane folded hybrid tee are shown in Figures 29 and 30. Effects of axial location of this coupler were much less than those encountered with the $TE_{0,2}$ coupler, as shown in Figure 31. On the basis of the difference patterns only, this coupler configuration appeared quite satisfactory.

It quickly became evident that port 2 sum pattern characteristics were being affected quite seriously by this difference coupler, due primarily to undesired coupling to the $LSE_{1,2}$ mode. Such sum pattern dependence multiplied greatly the number of measurements and considerations required for determination of the final configuration. An E-plane folded hybrid tee is used to combine the energy from the two transverse coupling slots and produce the required difference pattern. This tee has two output ports; one port, the H or side port, produces the difference of the two incident signals and the other, E or straight port, produces the sum. The H arm is the port which is used for the pattern. Measurements made on previous difference coupler configurations

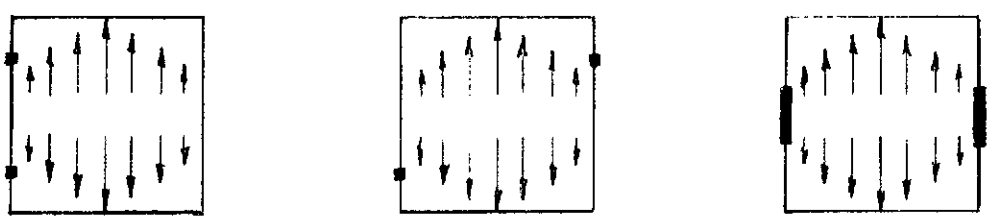

Fig. 27 $LSE_{1,1}$ Difference Couplers

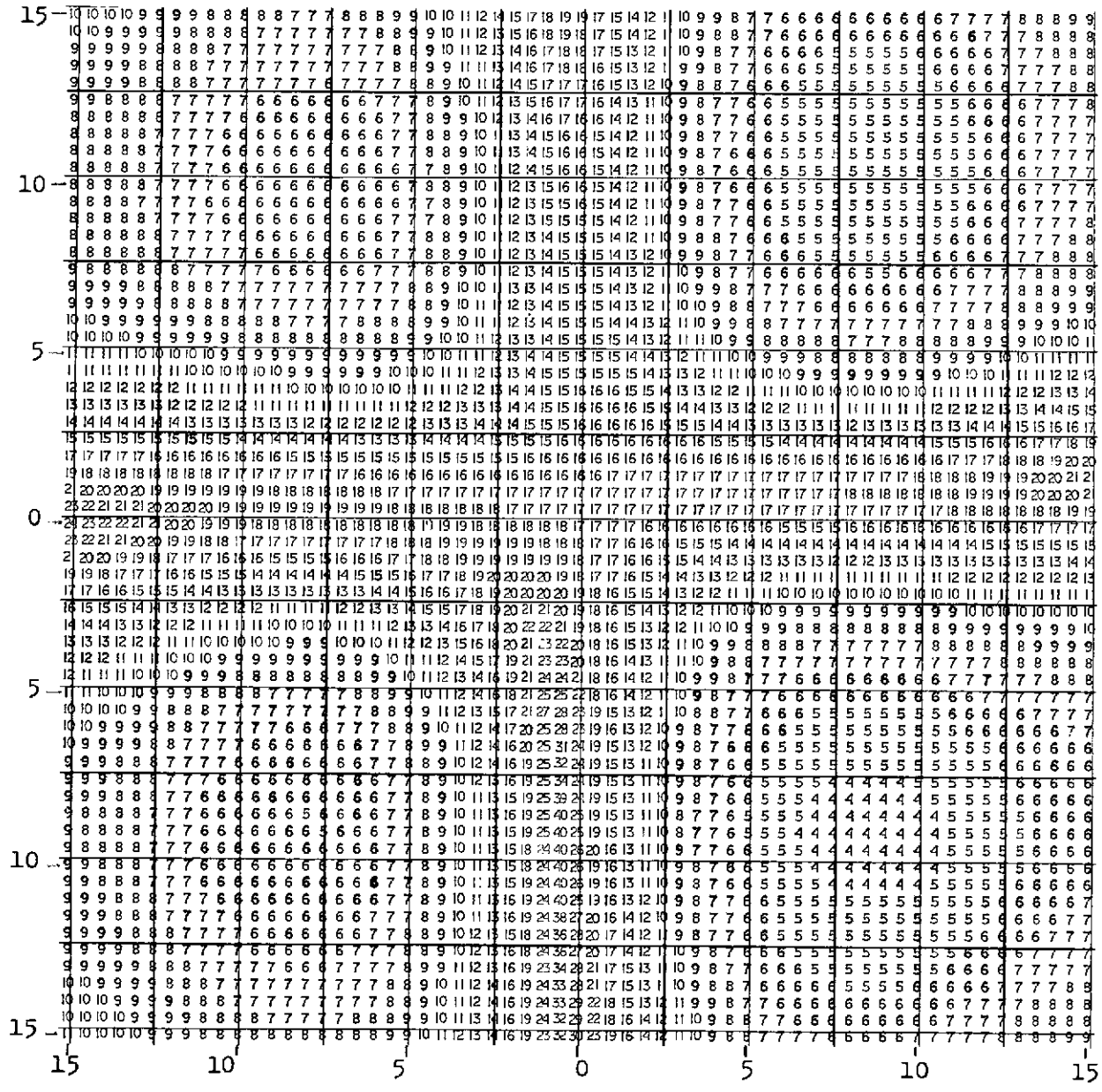

Fig. 28 Effects of Mode Interaction

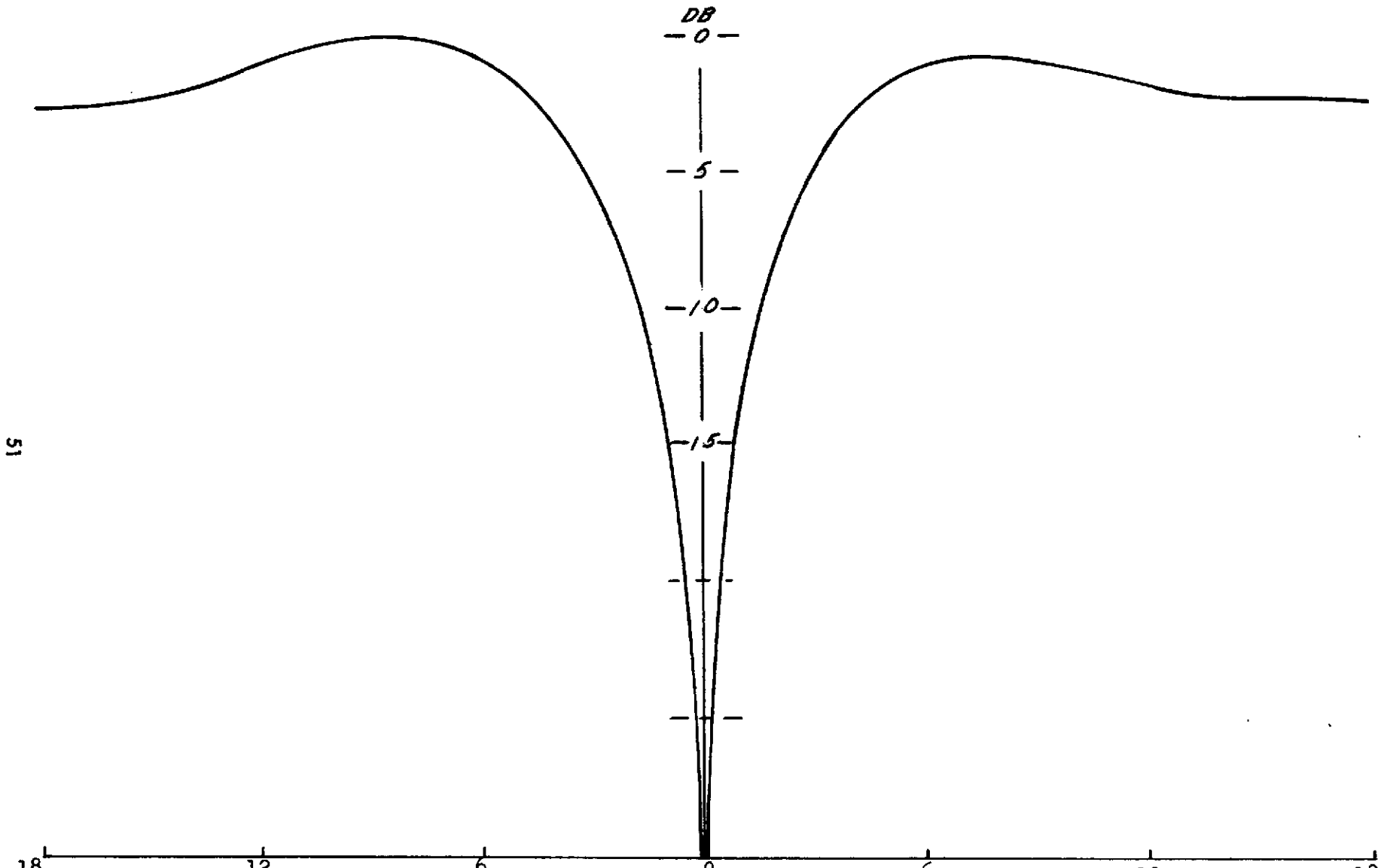

Fig. 29 $LSE_{1,1}$ Difference Pattern

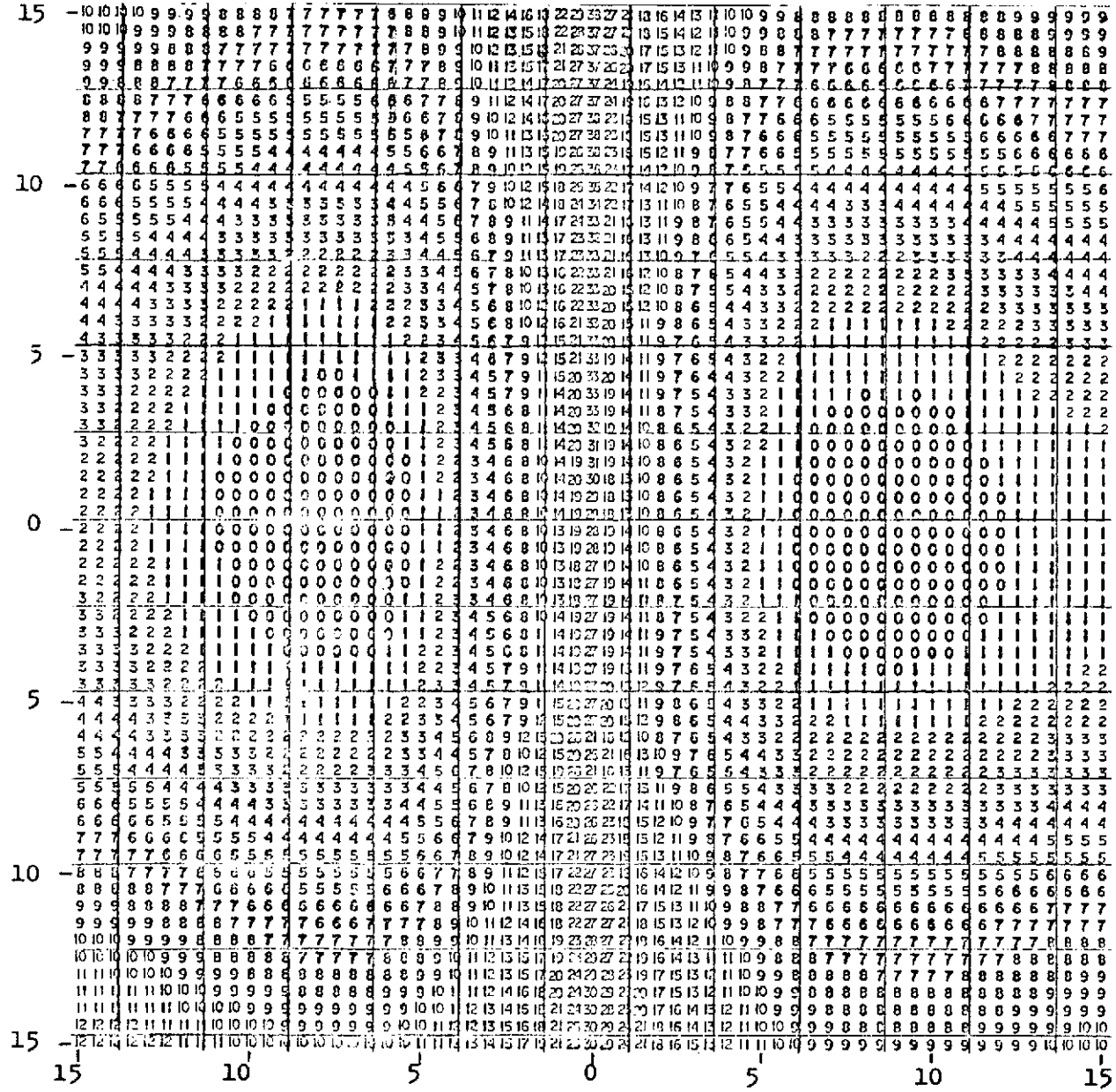

Fig. 30 $LSE_{1,1}$ Difference Pattern

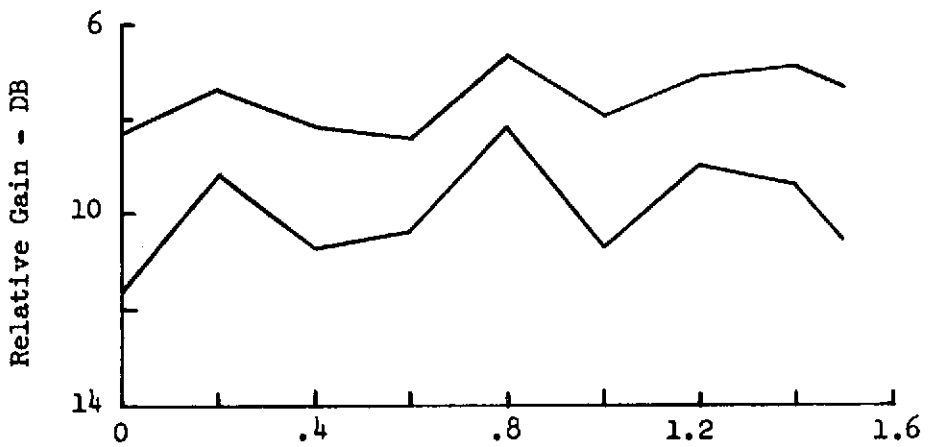

Fig. 31 $LSE_{1,1}$ Coupler Location

showed only negligible energy at the E arm and, therefore that arm was terminated and rarely sampled. Measurements on the network with the transverse slot coupler showed a degradation of sum pattern shape at the transmit frequencies and also a drop in efficiency of that channel. It was determined that appreciable transmit channel energy from the $LSE_{1,2}$ mode, which is cross-polarized to the receive channels, was being coupled to the E arm of the tee and wasted in the load. The effect of this $LSE_{1,2}$ coupling on port 2 patterns is presented in Figure 32.

The signals of the transmit $LSE_{1,2}$ and receive $LSE_{1,1}$ modes have phase characteristics such that all $LSE_{1,2}$ mode energy appears at the E arm of the tee, while $LSE_{1,1}$ energy appears at the H arm, as depicted in Figure 33. This results not only in the transmit channel efficiency drop but also the disturbance of the sum patterns, and requires that the E arm of the tee be treated as a major consideration in further development. While this condition is undesirable in that is presents another variable and further complicates the development effort, it does not, as will be seen below, degrade performance of the final feed network.

By placing a waveguide short at the proper position on the H arm, the $LSE_{1,2}$ energy can be reflected back through the tee and reintroduced into the feed network in the proper phase without disturbing the $LSE_{1,1}$ difference pattern characteristics. Figure 34 is a plot of port 2 gain versus the position of a variable waveguide short on the H arm of the tee. While the absolute value of the short location depends upon axial position of the difference coupler, this plot serves to depict the substantial impact of short position on port 2 pattern characteristics. No interaction of the variable short with port 1 or port 3 patterns was found.

Construction of the difference couplers utilized to this point precluded simultaneous placement in their individually optimum locations, as determined from Figures 24 and 31. A combined coupler, with both sets of slots, was therefore

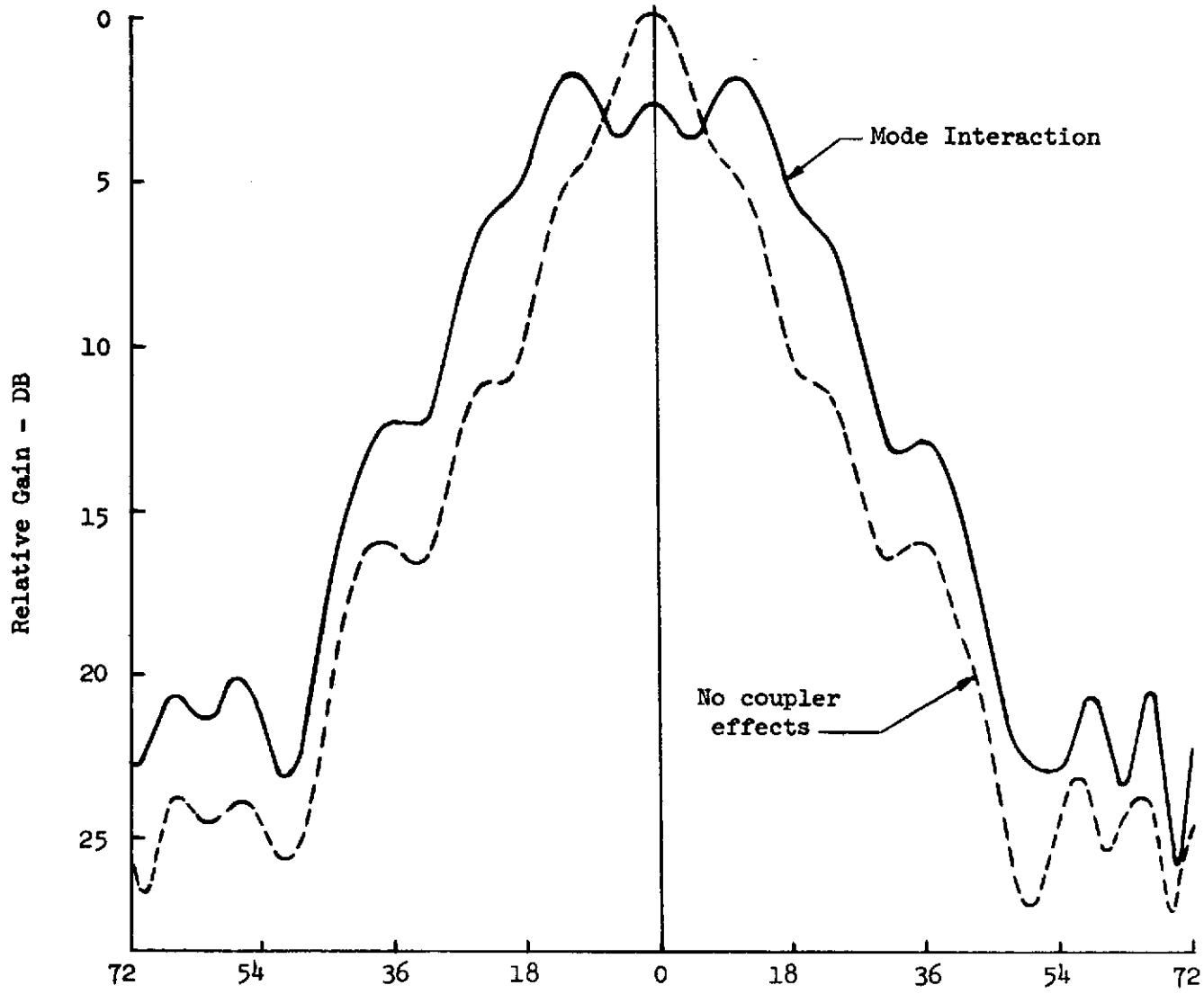

Fig. 32 Mode Coupling Effects on Transmitter Port

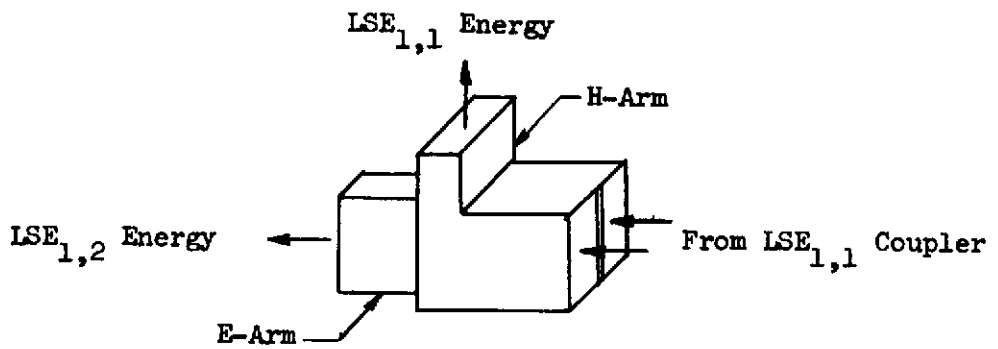

Fig. 33 Mode Energy in hybrid tee

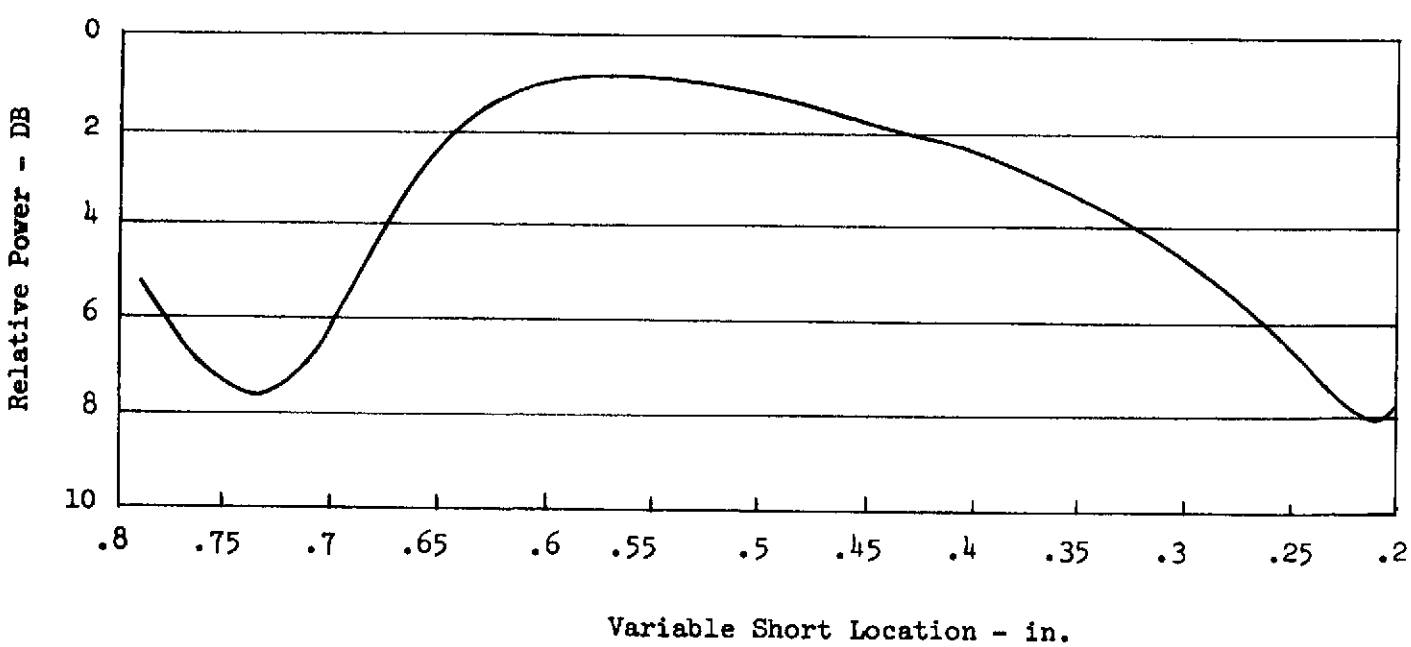

Fig. 34 Coupler Shorting Effects on Part 2 Gain

fabricated. Measurements were then made, varying overall length, coupler location and the position of the short on the $LSE_{1,1}$ combiner tee. The optimum feed network geometry, as depicted in Figure 35, was determined from these measurements.

Patterns of each port of the final configuration are presented in Figures 36 to 39, for the center and band edges of the respective frequency bands. In Figure 36, the H-plane pattern is included for comparison with the E-plane patterns. It can be seen that at the lower edge of the transmit frequency band, 14.550 GHz, the E-plane pattern closely matches the H-plane pattern as desired, while at the higher frequencies there is appreciable pattern mismatch. This would appear to require merely a shorter phasing length to accomplish pattern balance, but such a change only aggravated the situation on the transmitter port and also degraded the receive sum port patterns. This characteristic was observed to a greater or lesser degree, in all patterns of feed network configurations which included the $LSE_{1,1}$ tracking coupler, suggesting some form of interactive mode coupling in the transverse slot pair. This appears to indicate a bandwidth limitation (in terms of efficiency) for configurations utilizing this type of tracking coupler, but that limitation falls beyond the 1.25-GHz bandwidth for which this network was designed. The phasing length was selected, in this case, to produce equal dispersion of the 14.650- and 14.750-GHz E-plane patterns from the H-plane pattern at the edge of the subreflector ($\alpha = 13.5$ degrees).

The receive sum patterns, port 1 shown in Figure 37, demonstrate a good match between E- and H-plane patterns across the receive frequency band. The H-plane pattern is identical to the E-plane at the center frequency of 13.600 GHz and remains within approximately 1 db throughout the frequency band and well beyond the subreflector illumination angle.

The elevation difference pattern, port 3, which is produced by the $LSE_{1,1}$ coupler, is seen in Figure 38 to be virtually frequency invariant, the only

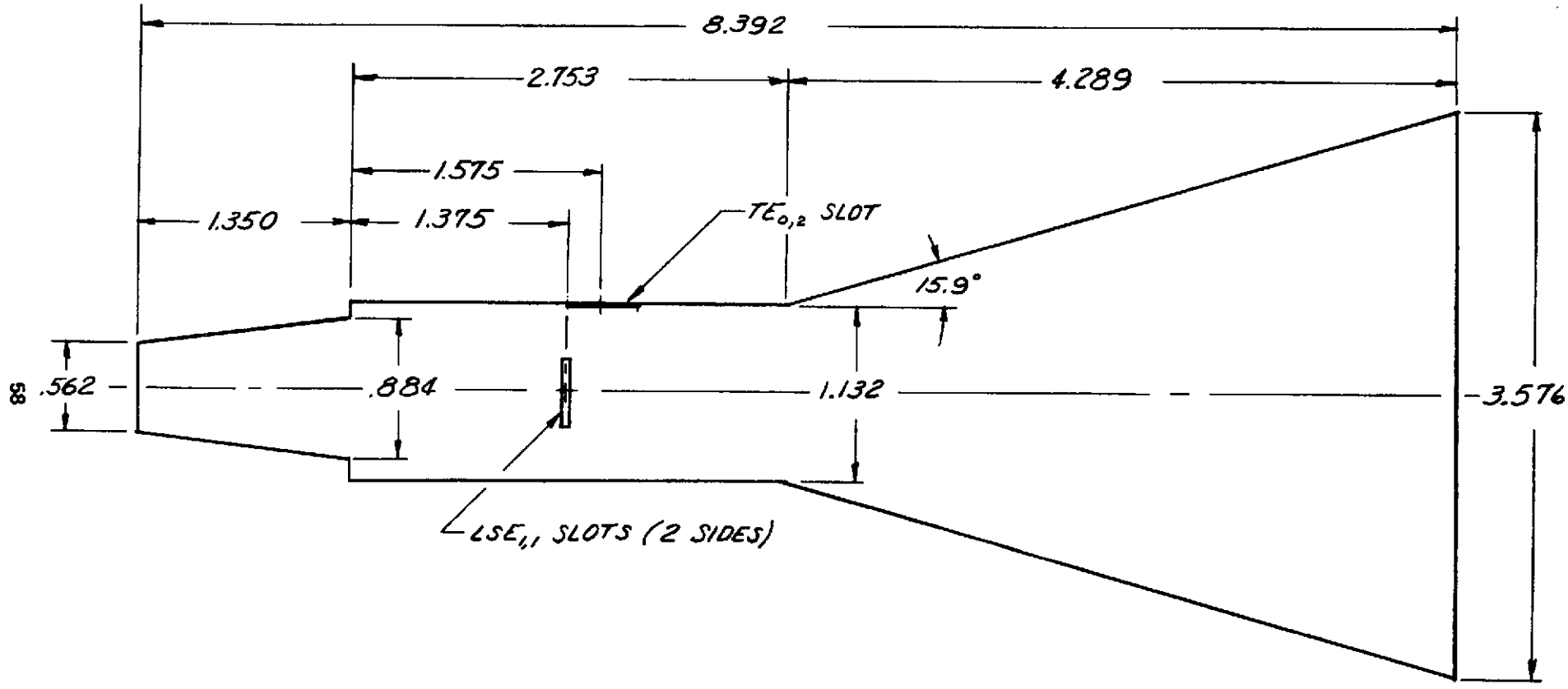

Fig. 35 Optimum Feed Network Geometry

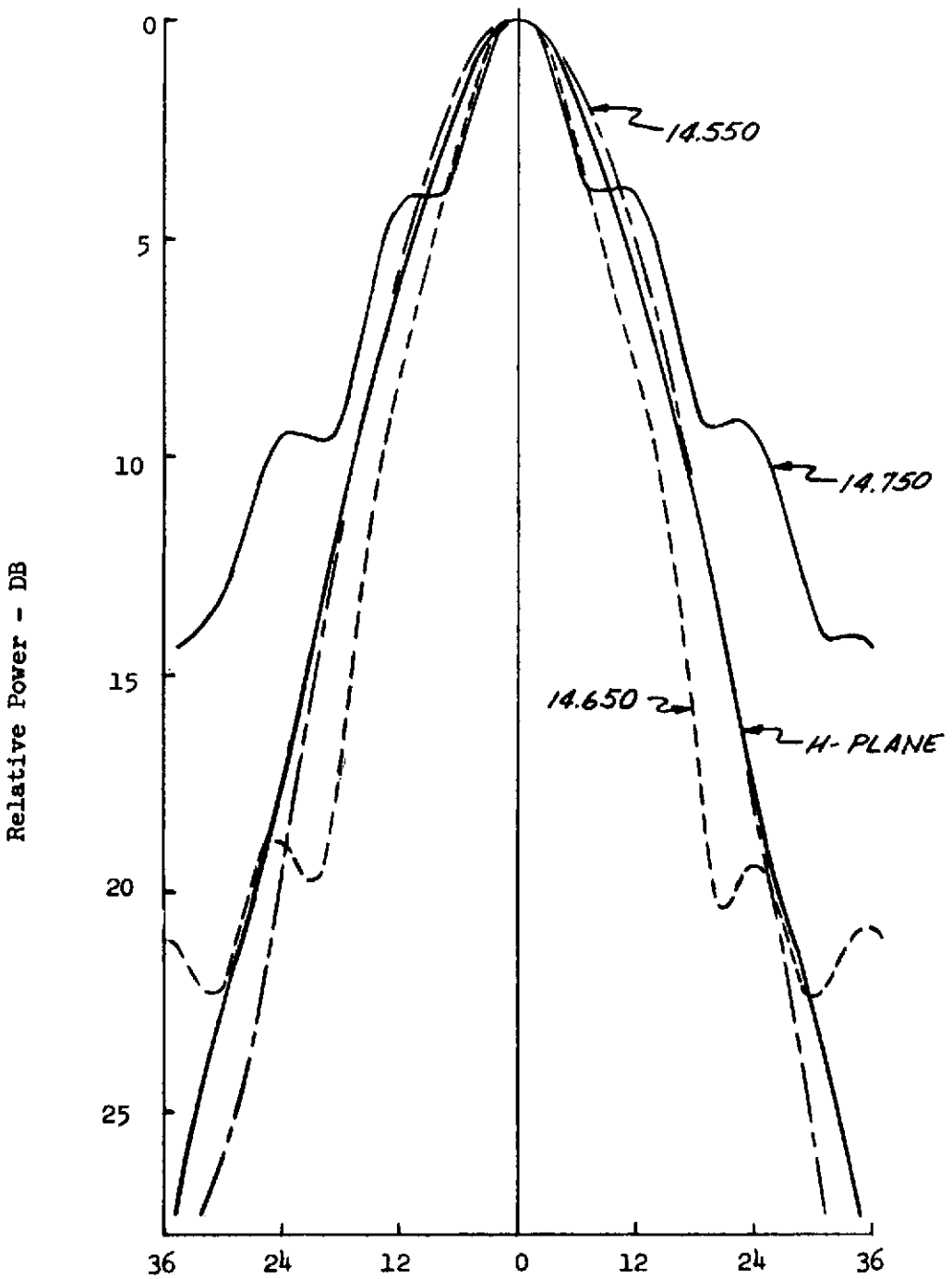

Fig. 36 Port 2 Sum Patterns

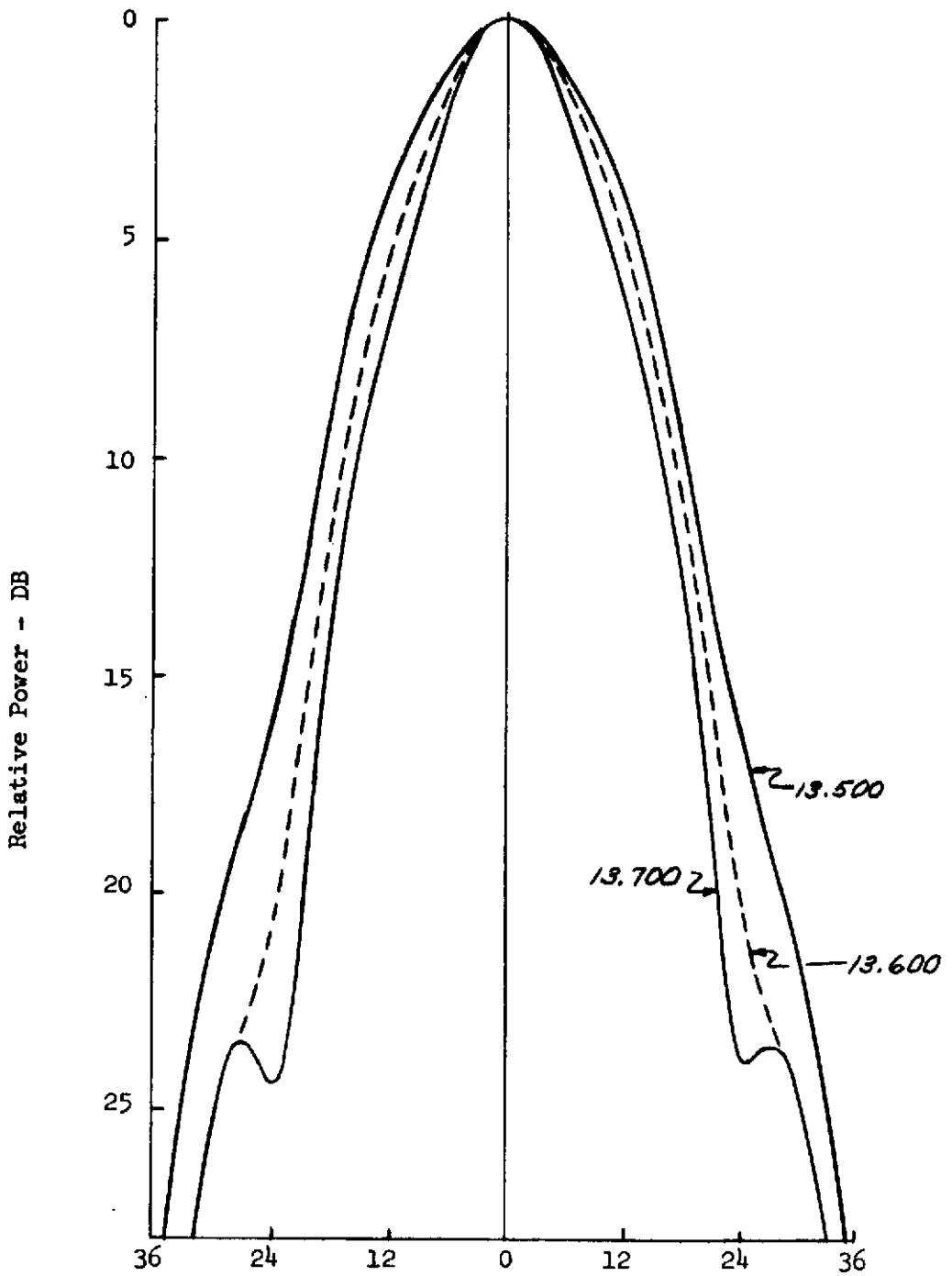

Fig. 37 Port 1 Sum Patterns

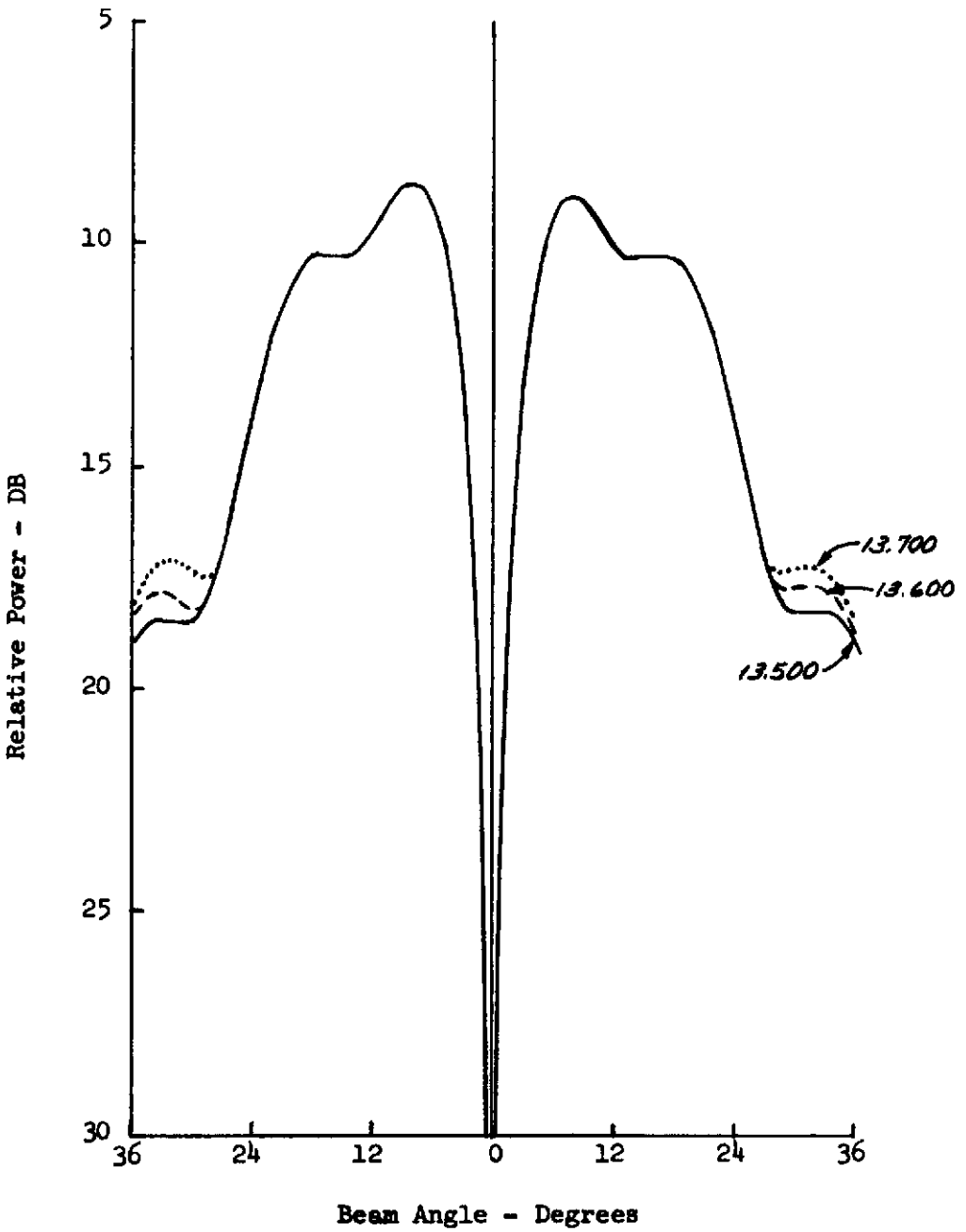

Fig. 38 Port 3 - $LSE_{1,1}$ Difference Pattern

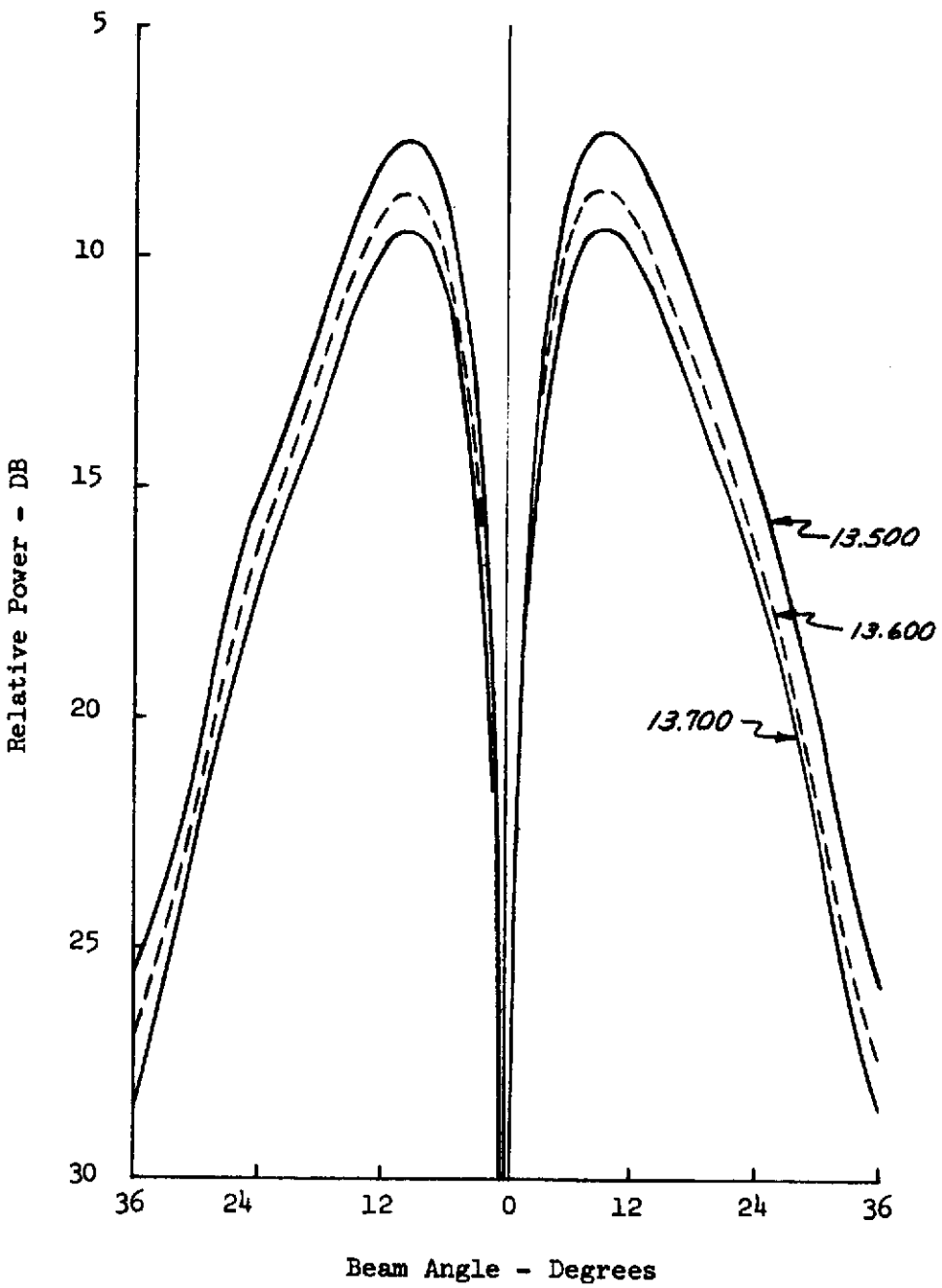

Fig. 39 Port 4 - $TE_{0,2}$ Difference Pattern

dissimilarity occurring is the height of the shoulder which appears around 30 degrees off axis. The azimuth difference patterns, port 4, produced by the $TE_{0,2}$ single-slot coupler, are seen to vary in gain but not pattern shape across this frequency band. The pattern nulls of both couplers are totally frequency invariant, within measurement accuracy, throughout the bandwidth, a characteristic not often found in tracking networks of other types. The peak magnitudes of both sets of difference patterns are slightly lower than those obtained with separate couplers; this could most likely be improved with further effort on coupler location. The difference pattern levels achieved, however, are quite adequate for the desired sum-to-difference ratios. This configuration was selected as the design for the deliverable feed network.

2.2.4.5 Deliverable Network Implementation

A brief survey of techniques appropriate for fabrication of the feed network was performed upon determination of the final configuration. Internal intricacy and required tolerances substantially limit the available approaches; investment casting and electroforming emerged as the two best methods. Even for a single unit fabrication, casting was the preferred approached from a technical point of view, but 16- to 18-week minimum delivery schedule for such a casting made that method unacceptable. Therefore, it was decided to electroform the feed hardware. Although the electromagnetic performance of the resulting network was excellent, the electroform process did not prove entirely satisfactory. The vendor encountered unexpected tooling and processing difficulties which resulted in nearly 7-week slip in delivery. Additionally, the part was comparatively heavy, and required several post-electroforming operations which resulted in local deformities in internal network dimensions. For these reasons, the investment casting approach would be highly recommended for any subsequent fabrication. Photographs of the electroformed network, with the orthomode transducer, $LSE_{1,1}$ combiner network and polarizer attachment lugs installed, are shown in Figure 40.

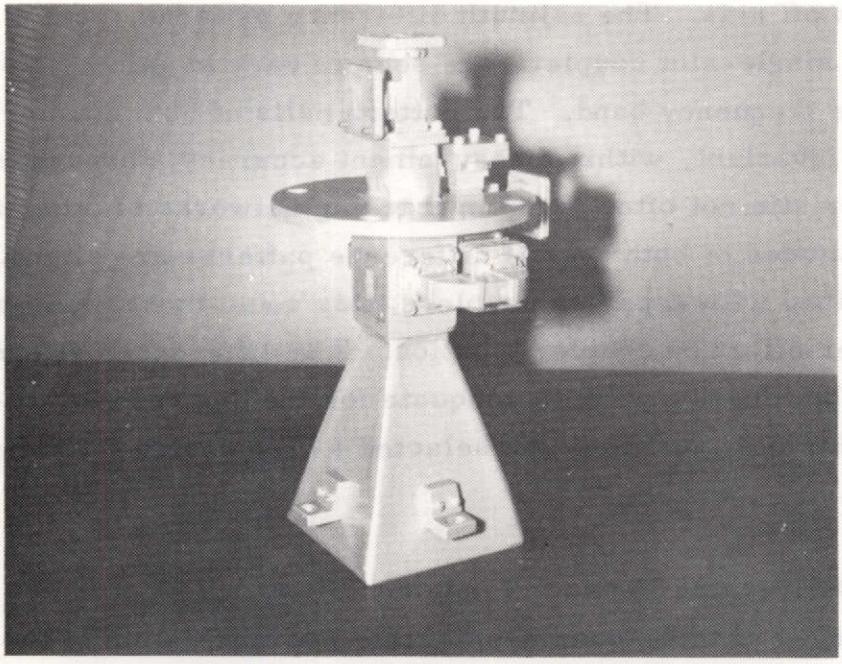

C-2

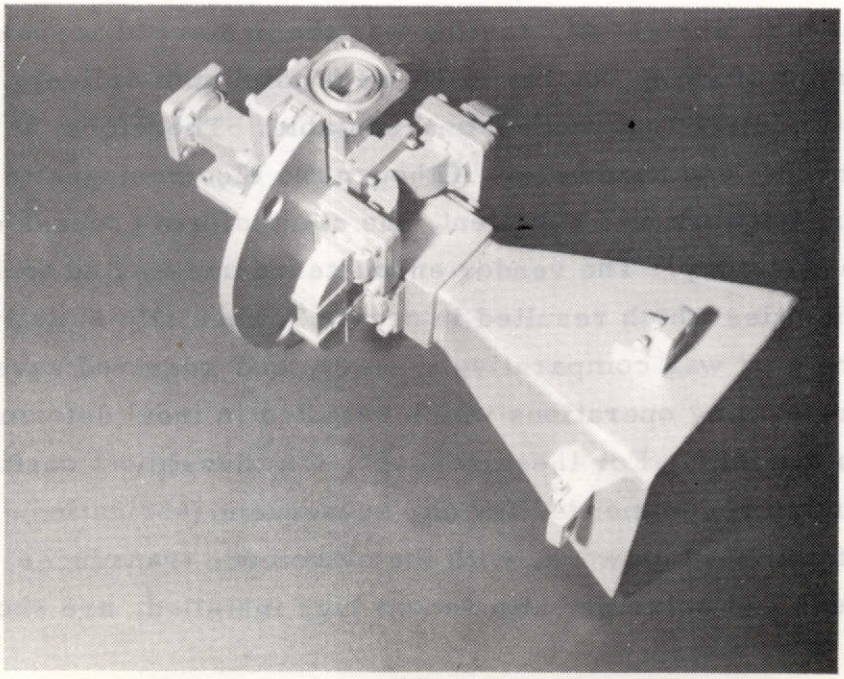

C-8

Figure 40. Electroformed Feed Network Assembly

Results of port 2 gain versus $LSE_{1,1}$ combiner short position measurements are presented in Figure 41. There is an obvious difference in the optimum short positions for each frequency, indicating that the $LSE_{1,1}$ coupler produces a prime limitation on the bandwidth of the network. The best compromise short position occurs at 0.337 on the variable short micrometer with a port 2 gain loss of 0.1 db at the center frequency and 0.5 db at the band edges. The variable short was then measured on a network analyzer to determine electrical length, and a fixed short was machined to provide that length.

Figure 42 depicts the VSWR characteristics of the various ports of the feed network. The VSWR achieved in the deliverable unit was somewhat poorer for each port, particularly ports 2 and 4, than those obtained with the prototype unit. This can likely be attributed to the internal deformations in the tapered section of the feed which occurred during brazing of the mounting ring. The VSWR of port 1 remained below 1.4:1 throughout the receive frequency band. Port 2 is 1.8:1 or less across the trasmit band, which is considerably higher than expected from earlier prototype measurements. The VSWR of this port was quite sensitive to location of the $LSE_{1,1}$ combiner short; as would be expected, the short location which optimized pattern characteristics also provide the best VSWR. VSWR's of the other three ports were essentially independent of the short location. The output port of the $LSE_{1,1}$ combiner shows a maximum of 3:1 at the lower edge of the band, dropping to nearly 1.5:1 at the upper edge, although the single-slot VSWR was reasonably good for each slot of the pair. The $TE_{0,2}$ output, port 4, approaches 2:1 at the lower band edge, appreciably worse than for the prototype unit. It is felt that the VSWR characteristics of each port could be improved considerably with further effort in that area.

The near-field patterns of the deliverable feed network (Figures 43 through 56) are nearly identical to those of the prototype unit, but do indicate a slight difference in mode phasing characteristics. The receive sum patterns of

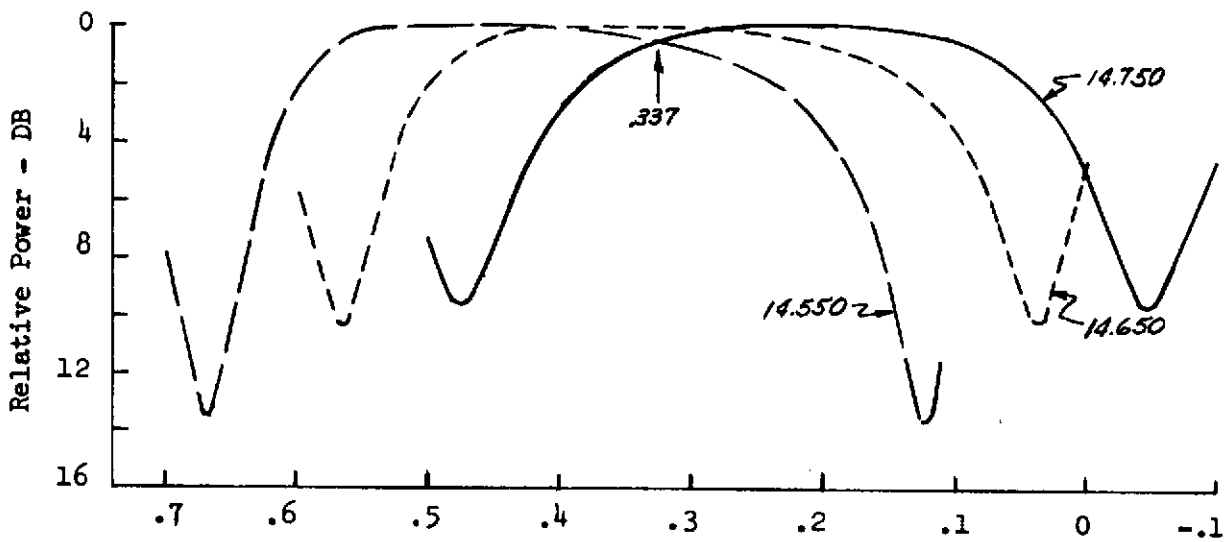

Variable Short Position - in.

Fig. 41 $LSE_{1,1}$ Combiner Short Optimization

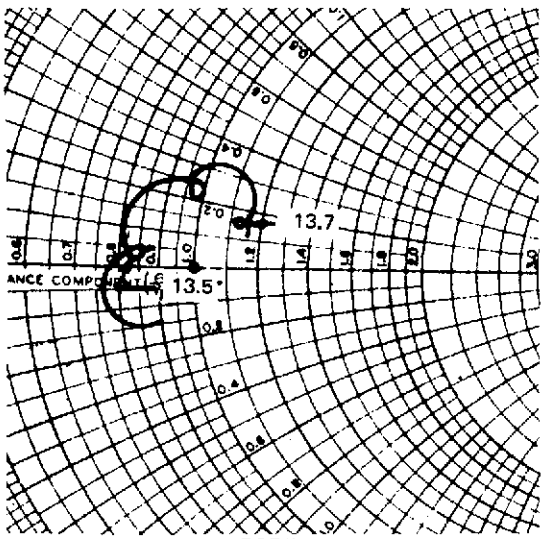

PORT 1

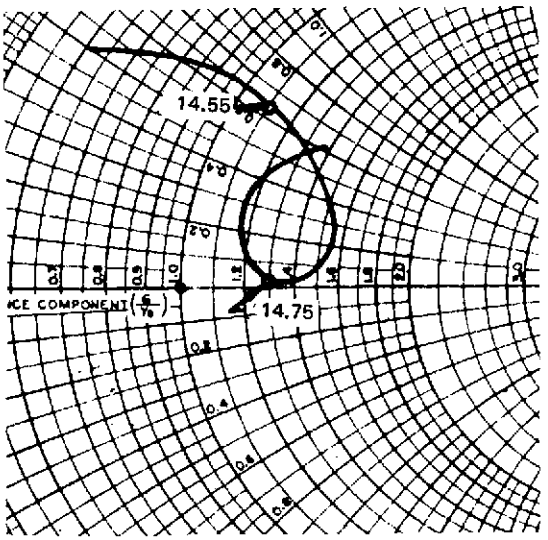

PORT 2

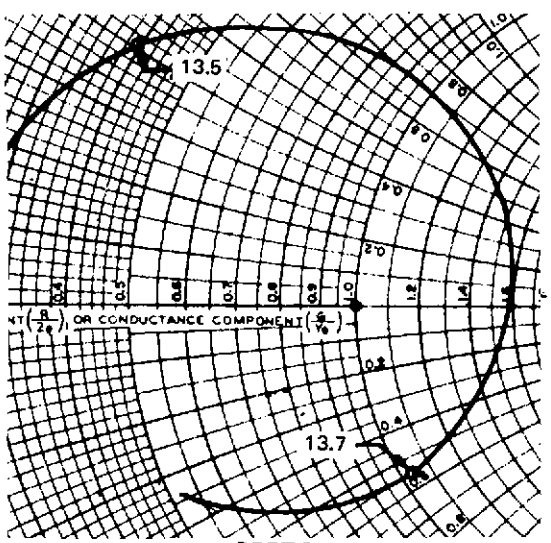

PORT 3

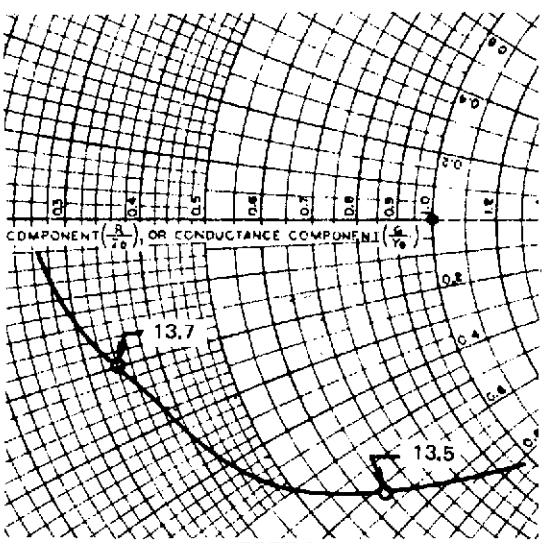

PORT 4

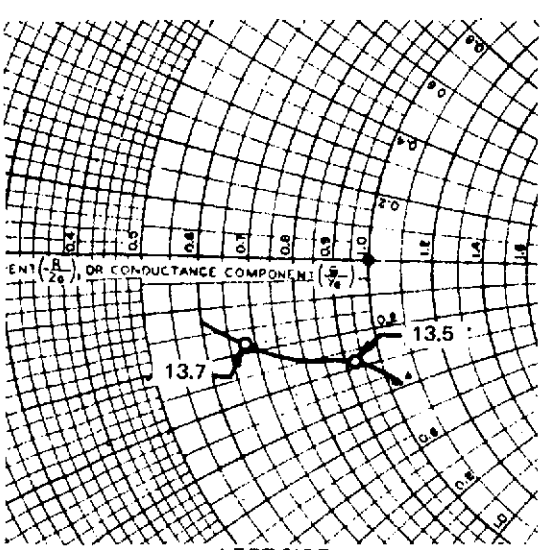

LEFT SIDE

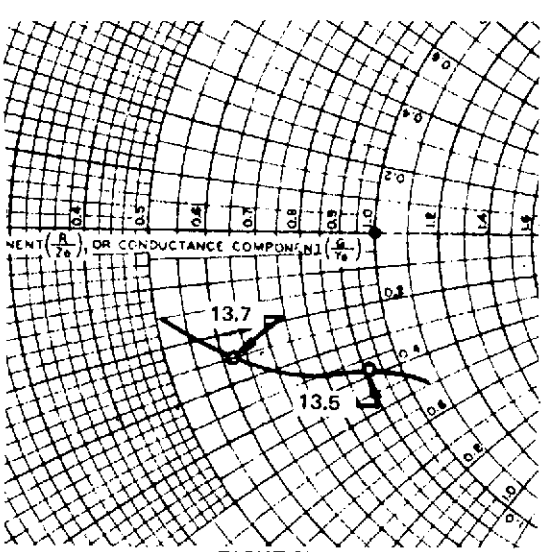

RIGHT SIDE

SINGLE LSE$_{1,1}$ SLOTS

Figure 42. Feed Network VSWR

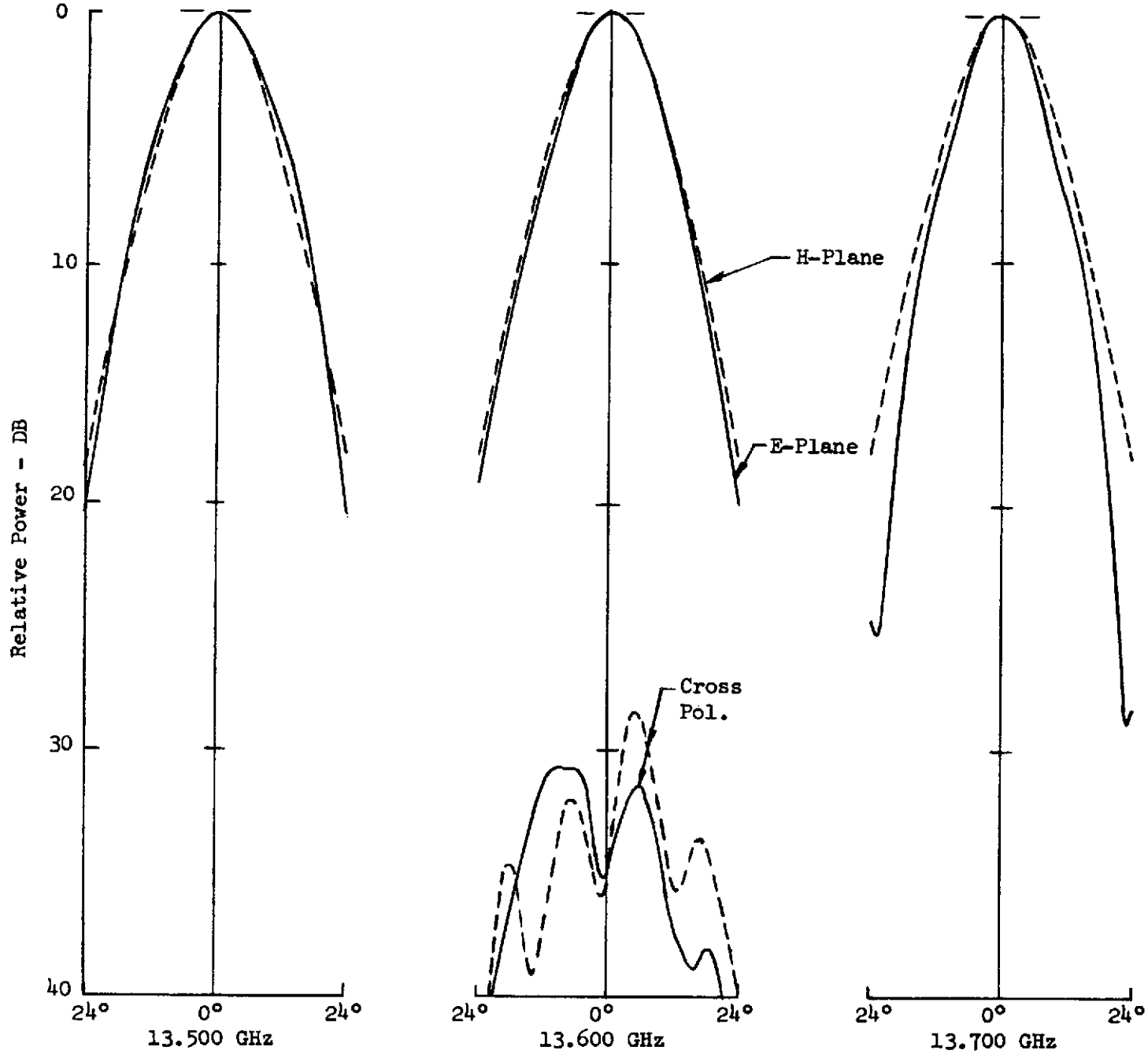

Fig. 43 Port 1 - Receive Sum Patterns

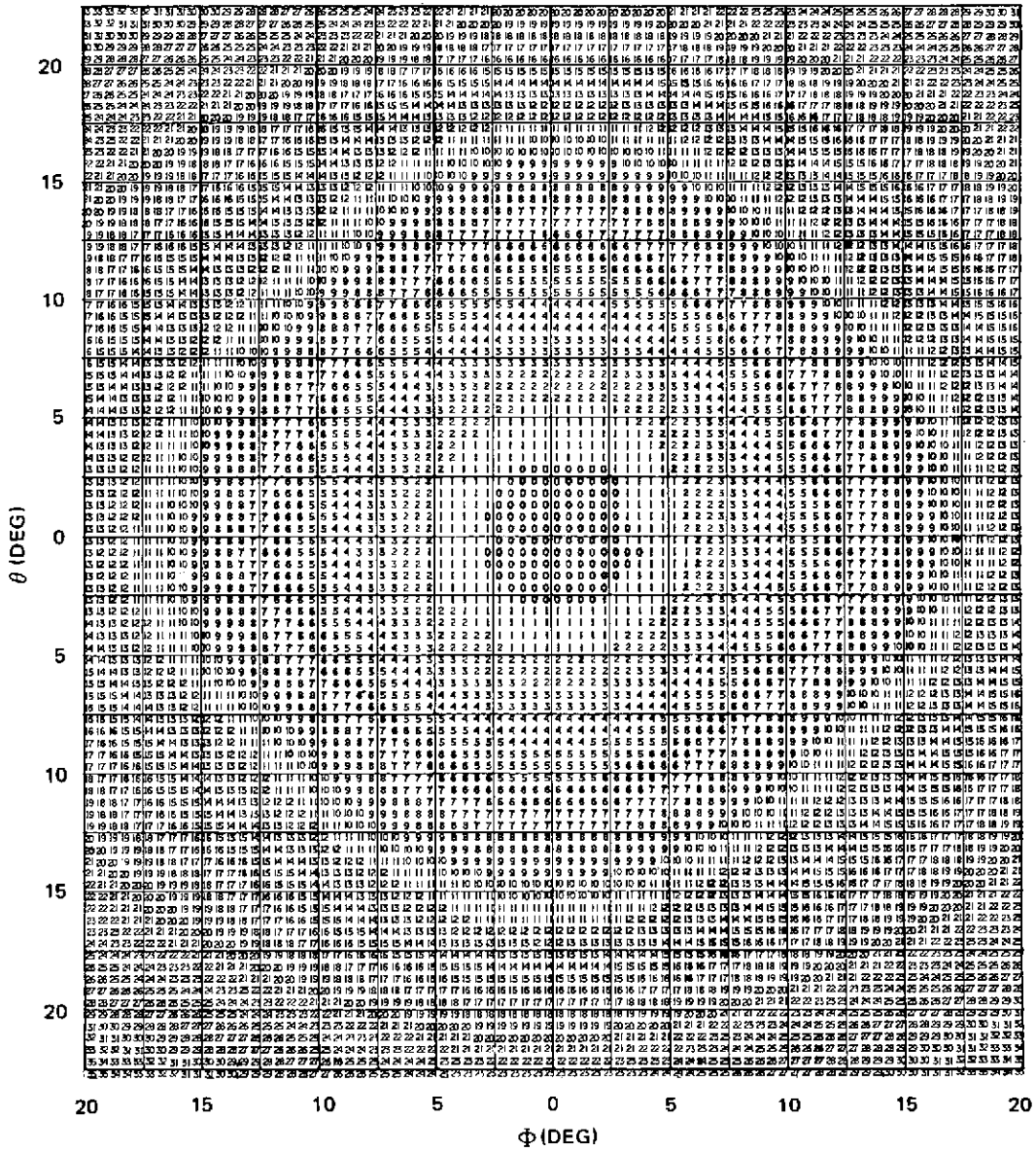

Figure 44. Port 1 Pattern Map

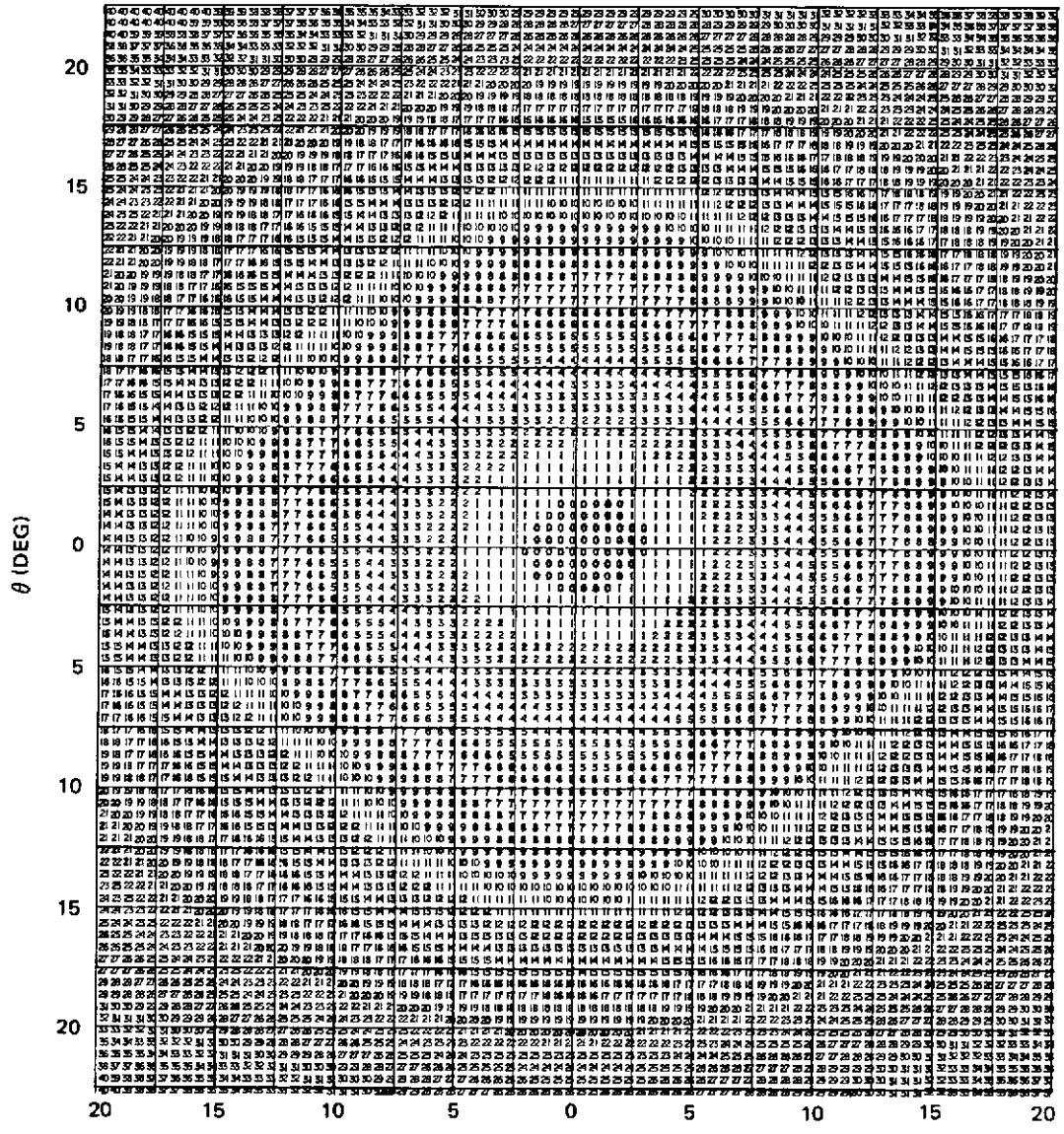

Figure 45. Port 1 - Band Edge Pattern Map

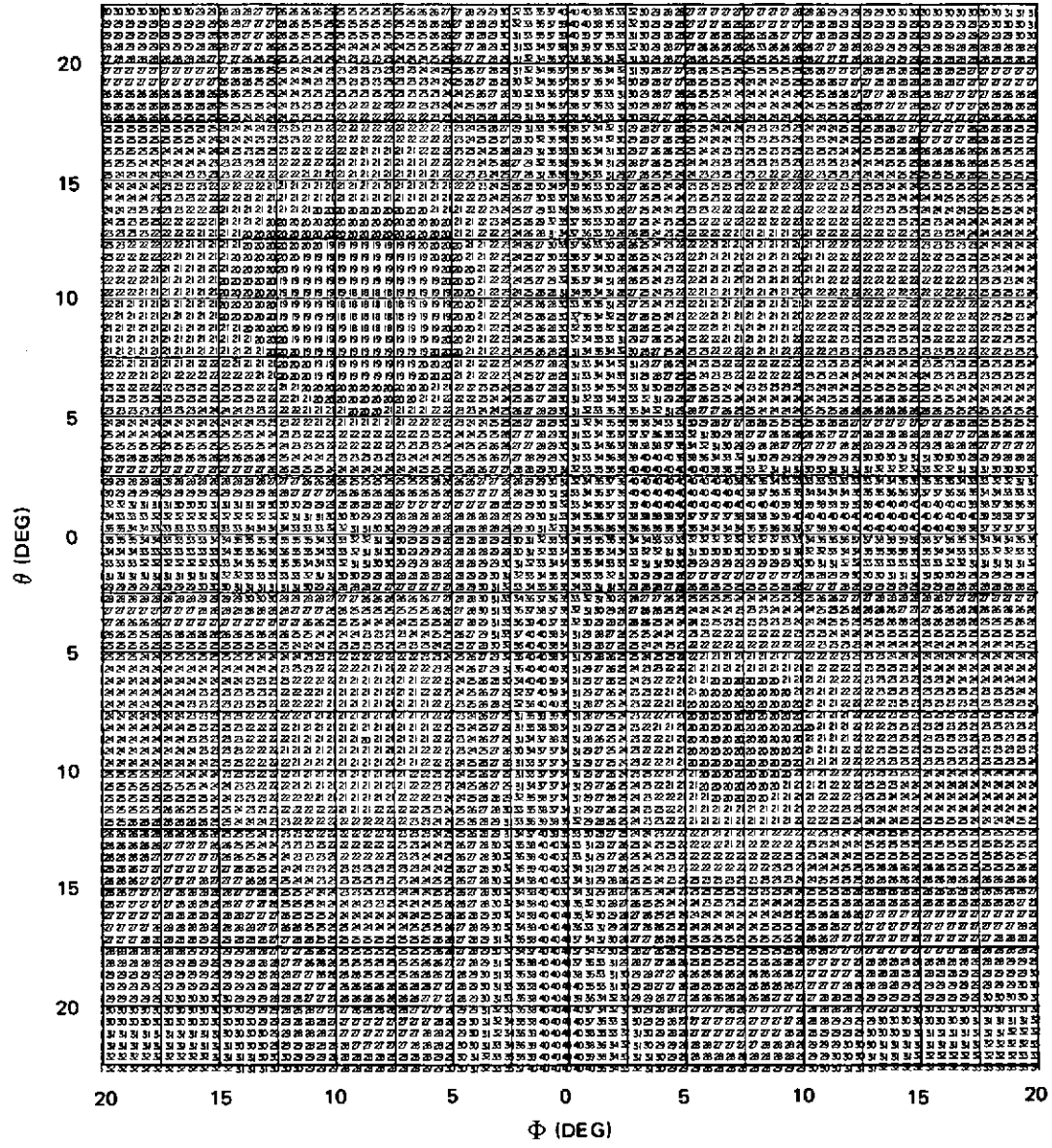

Figure 46. Port 1 - Cross Polarized Pattern Map

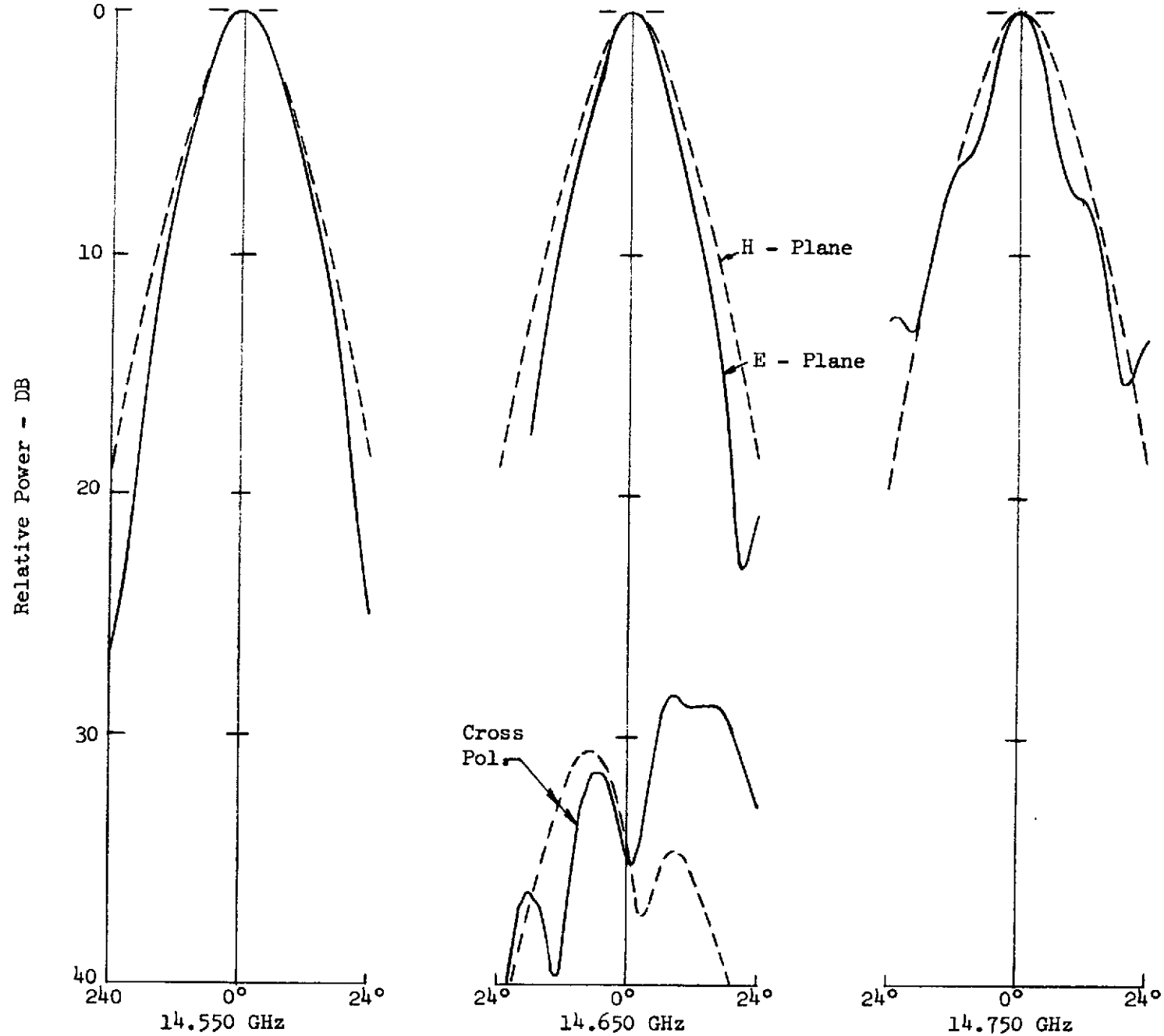

Fig. 47 Port 2 Transmit Patterns

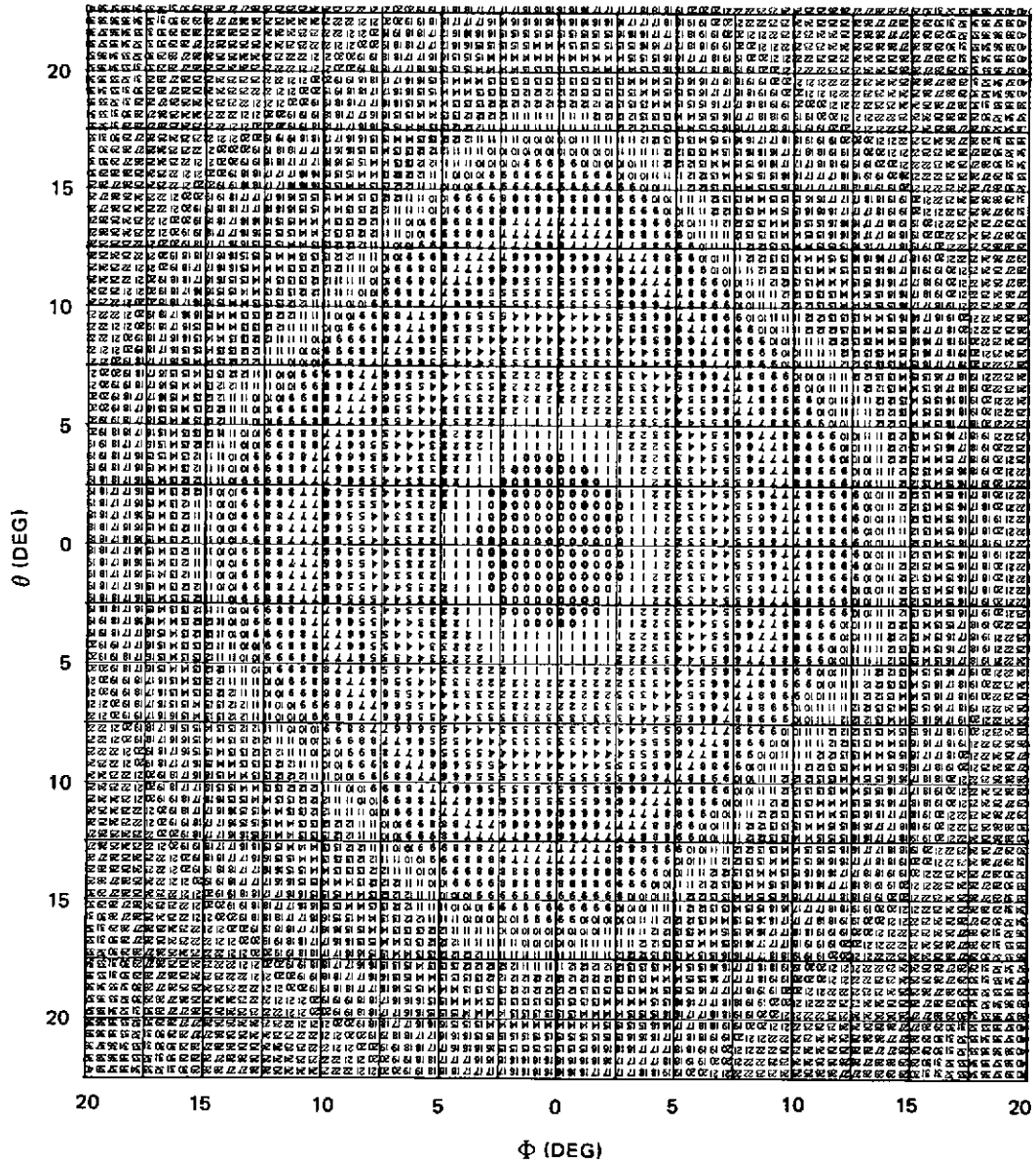

Figure 48. Port 2 Pattern Map

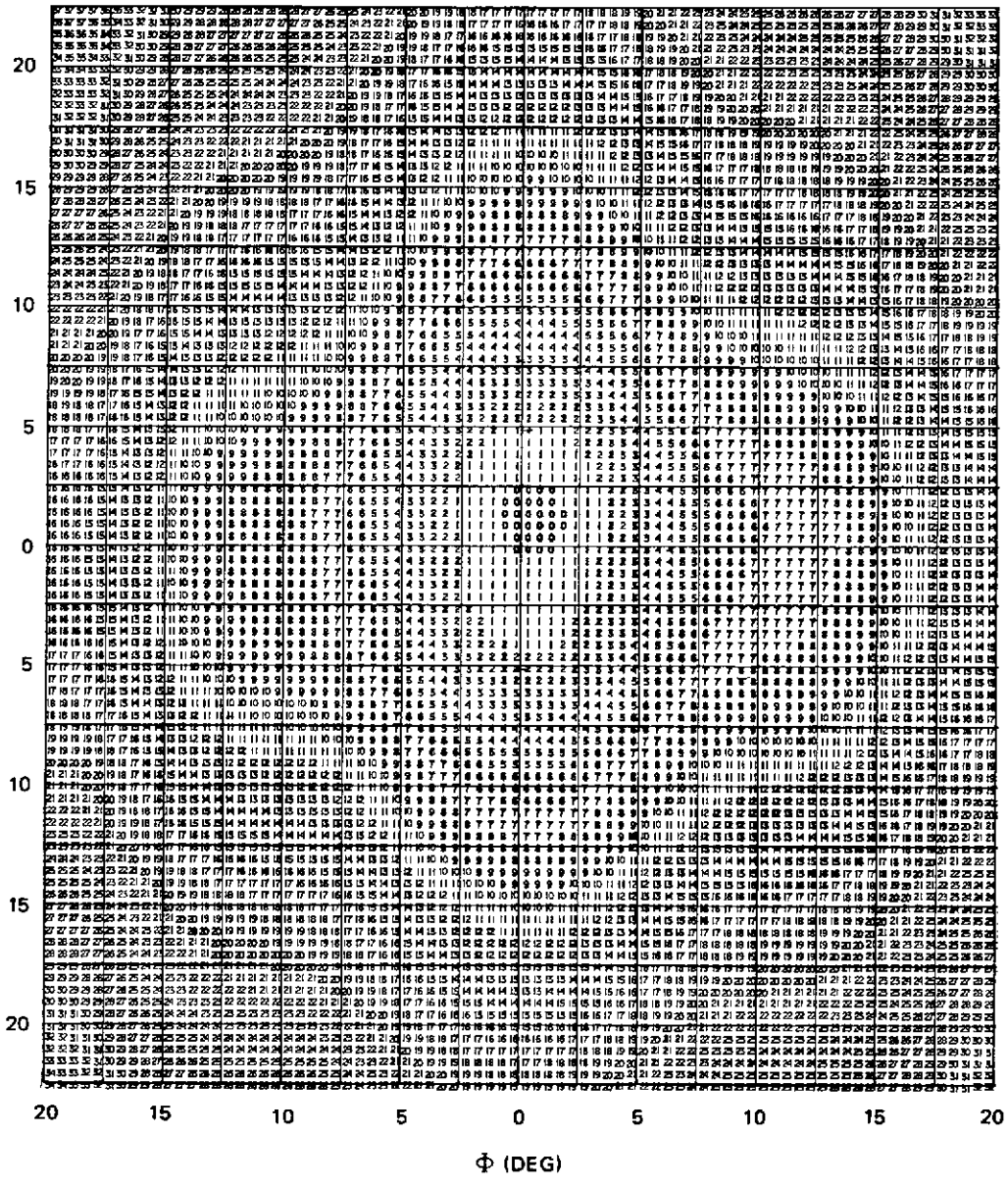

Figure 49. Band Edge Pattern Map

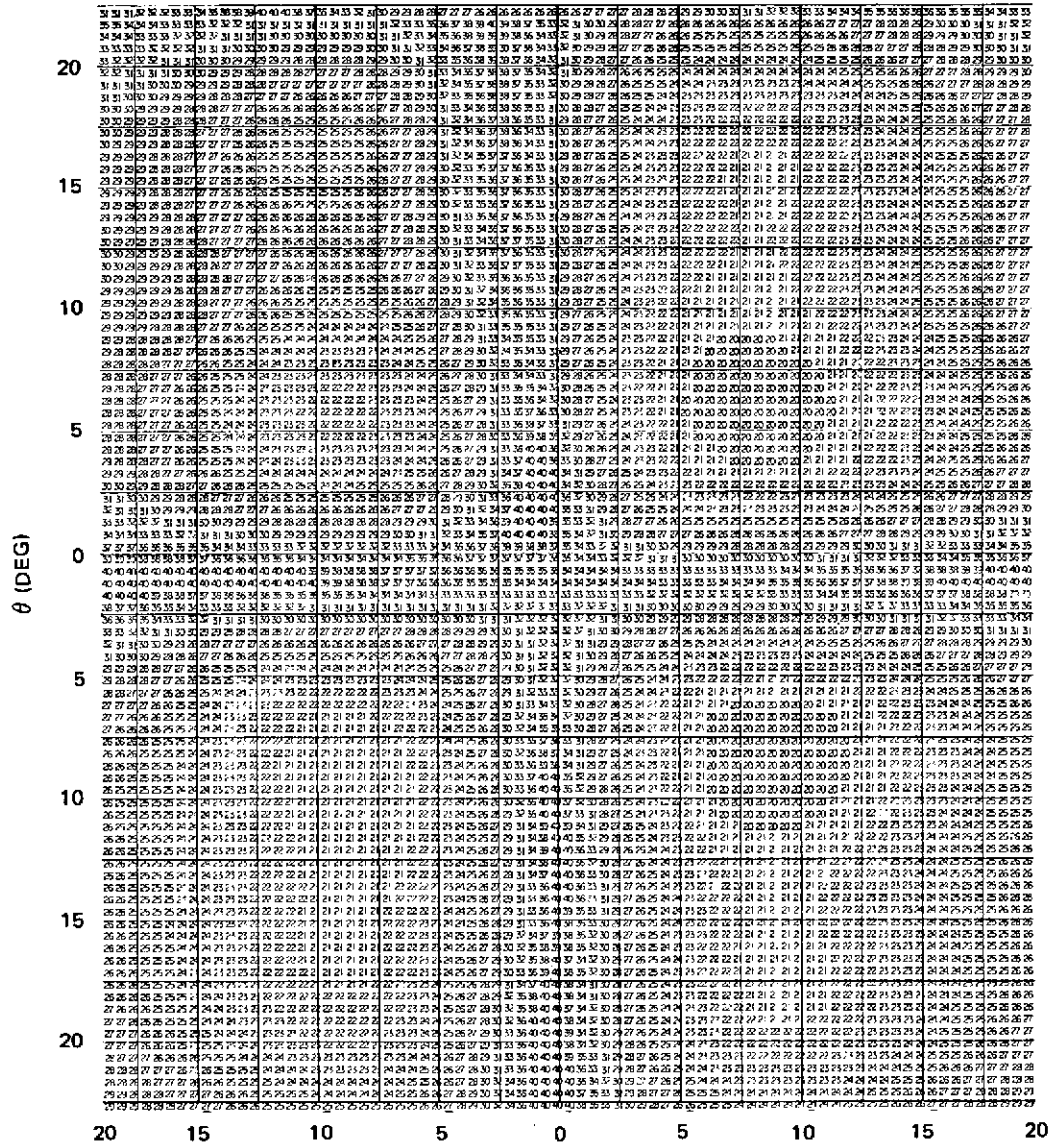

Figure 50. Port 2 Cross Polarized Pattern Map

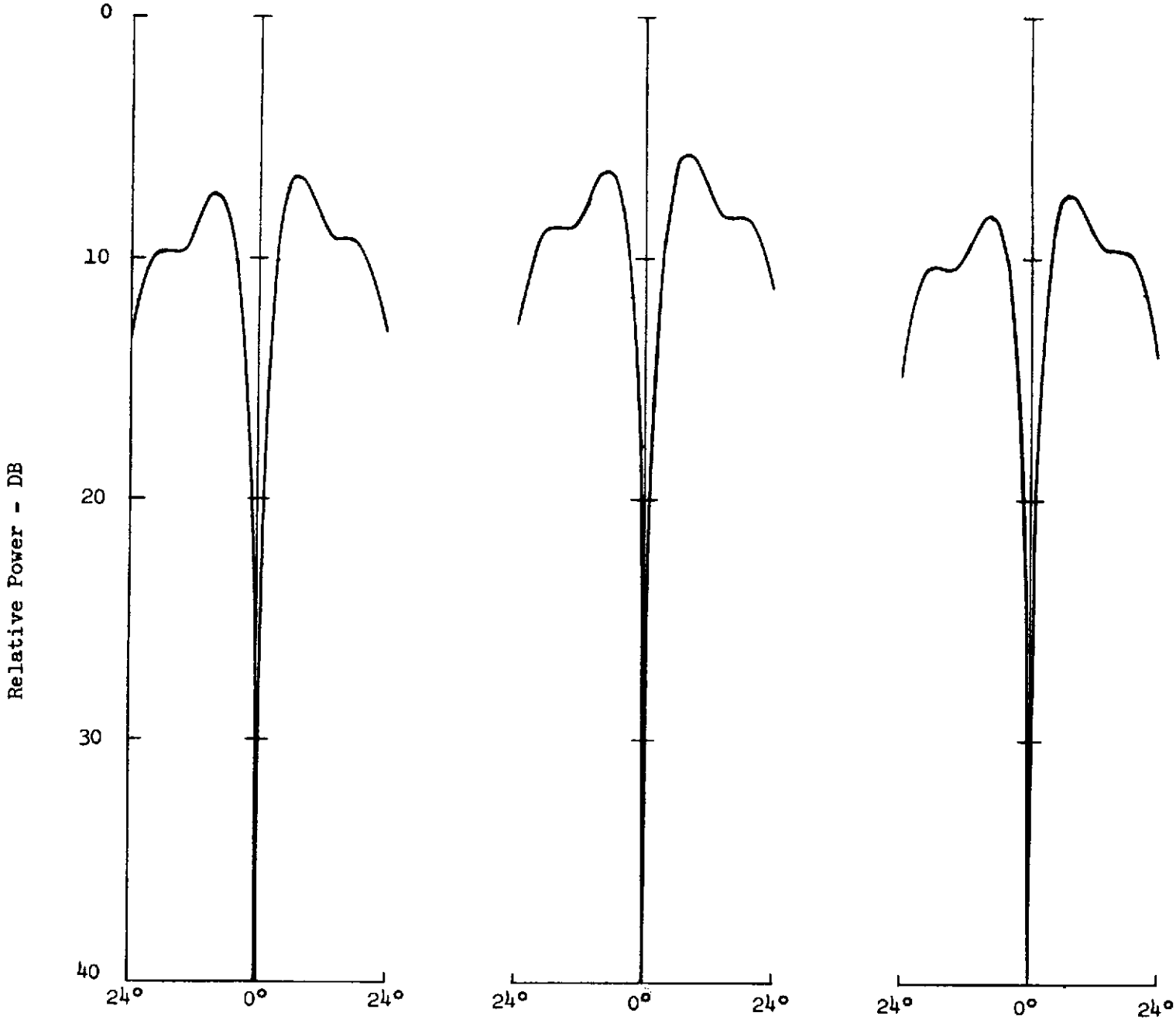

Fig. 51 Part 3 - $LSE_{1,1}$ Difference Patterns

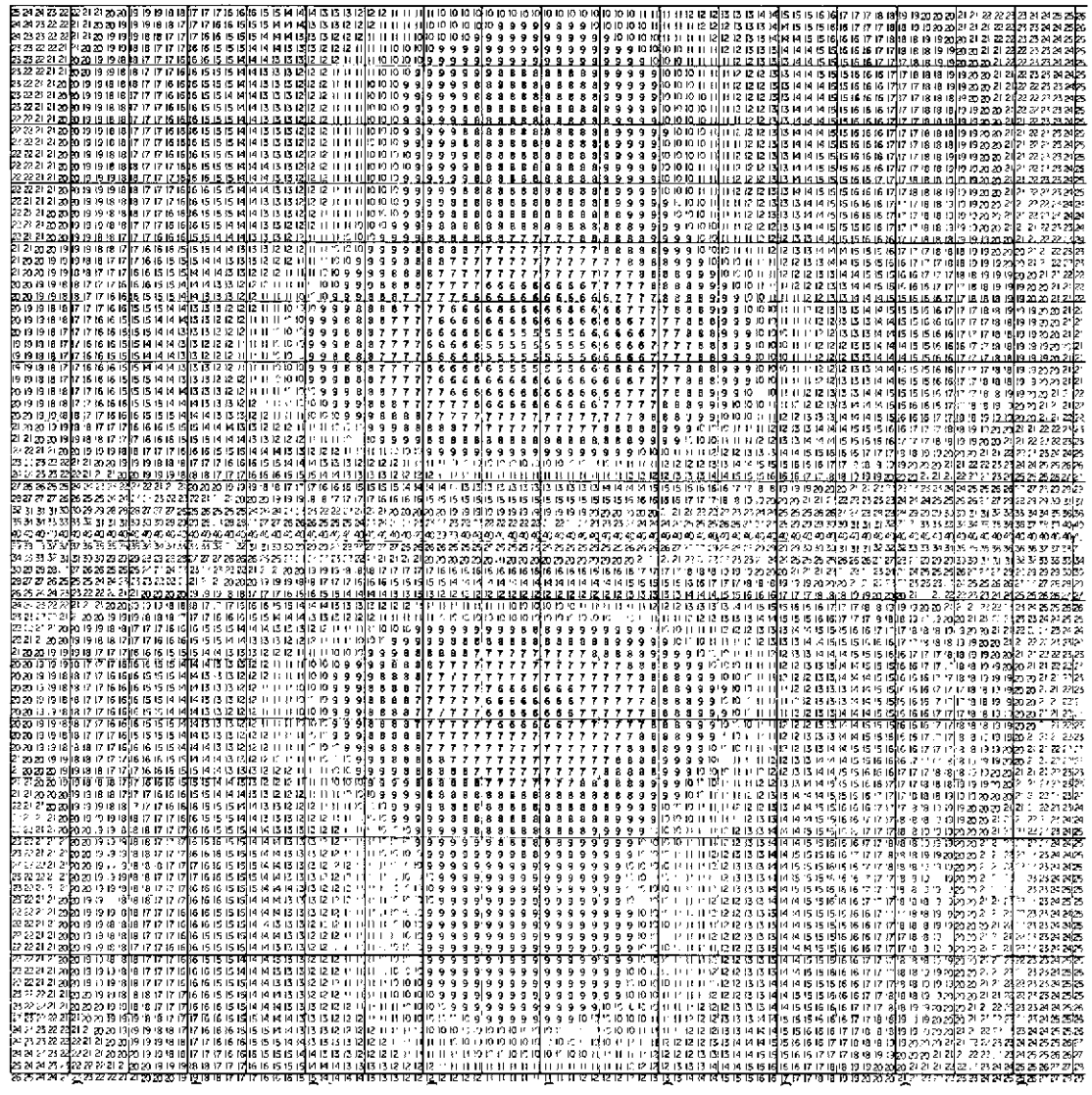

Figure 52. Port 3 Pattern Map

Figure 53. Cross Polarized Pattern Map

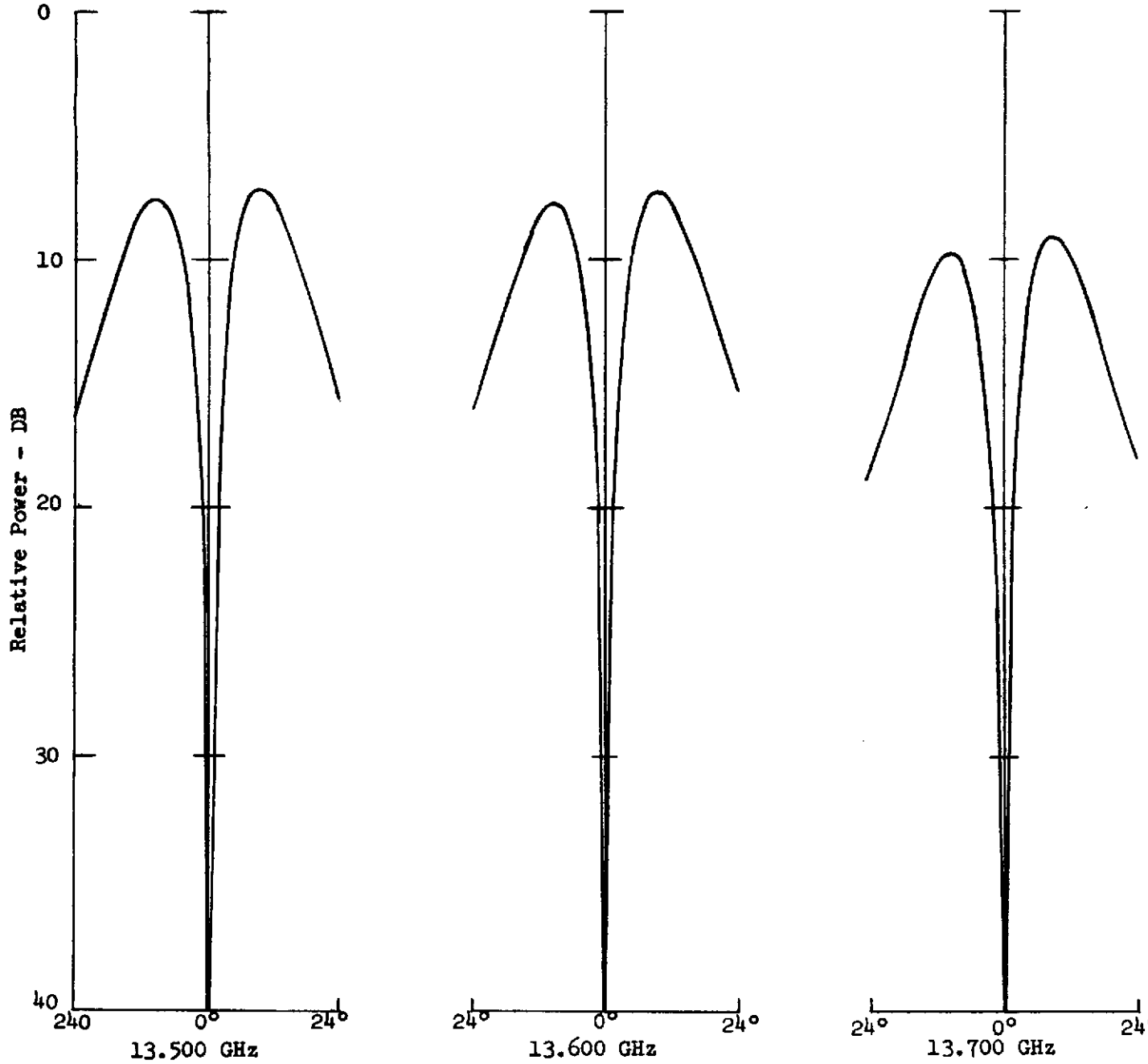

Fig. 54 Port 4 $TE_{0,2}$ Difference Patterns

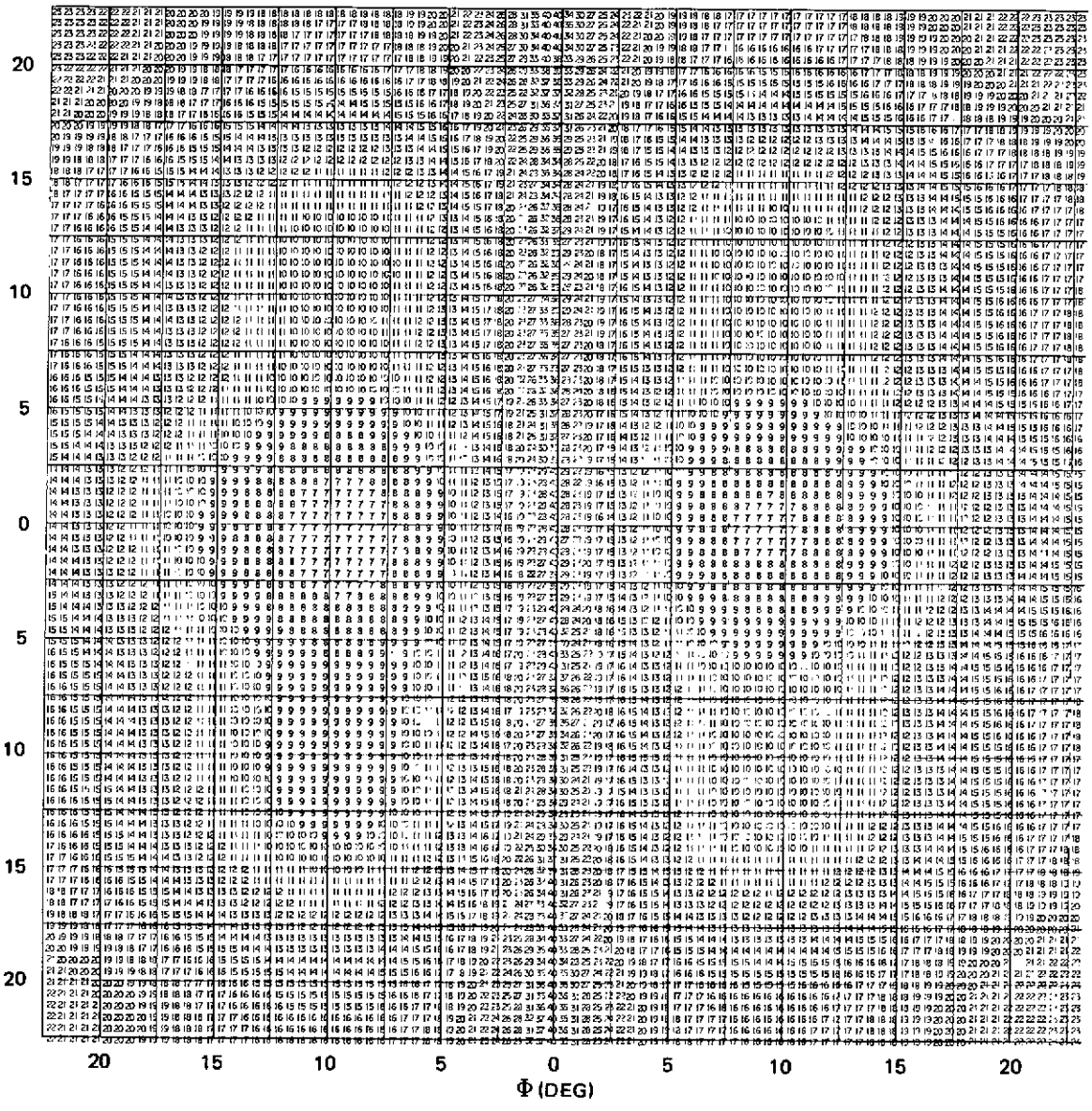

Figure 55. Port 4 Pattern Map

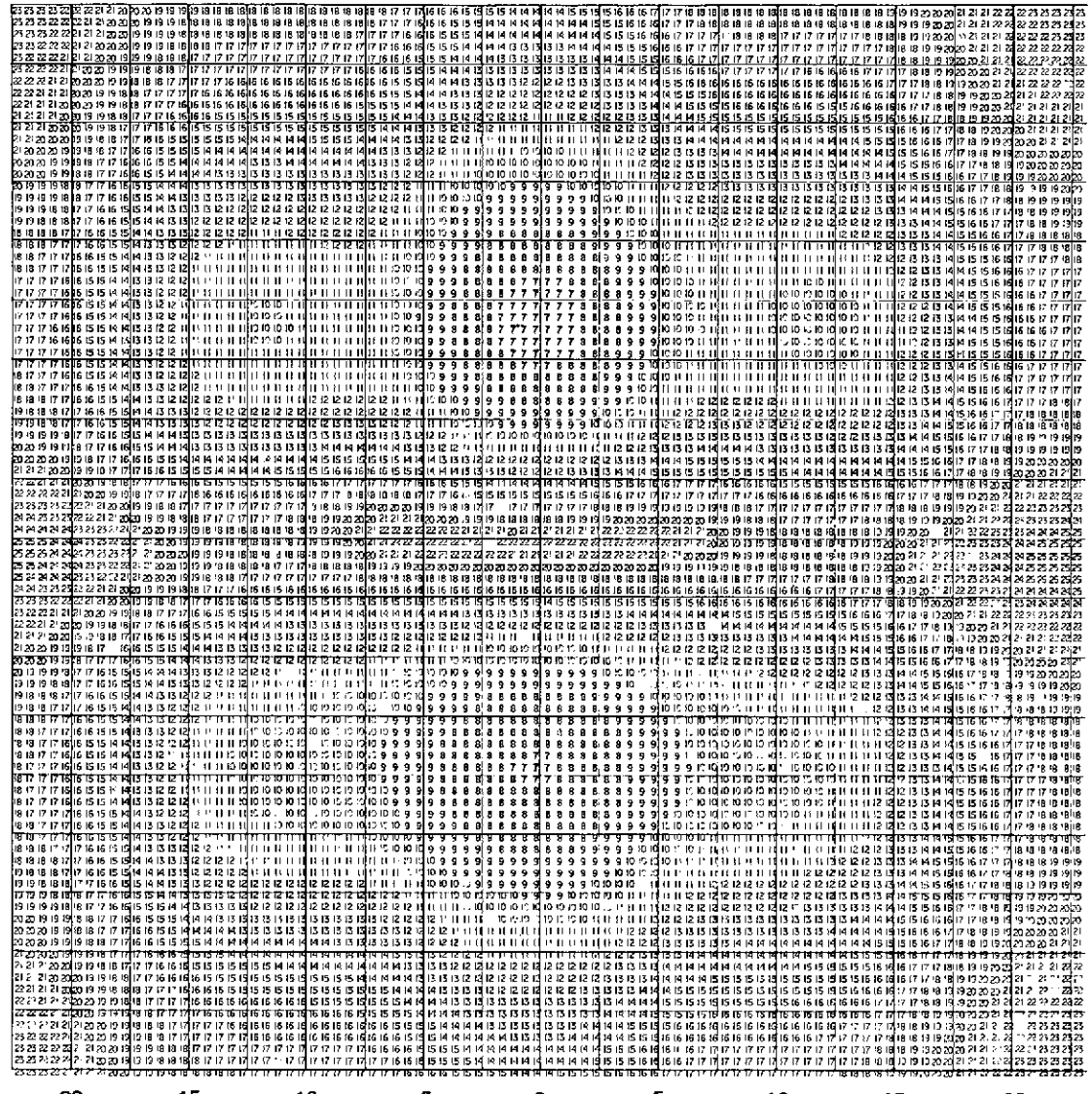

Figure 56. Port 4 Cross Polarized Pattern Map

Figure 43 demonstrate excellent matching of the E- and H- plane patterns throughout the frequency band. These patterns are essentially side lobe free as desired, with minor shoulders just beginning to appear at the higher end of the band. The cross-polarized patterns are typically greater than 30 db below the desired polarization in each pattern planes. A digital field map of the port 1 pattern, shown in Figure 44, demonstrates the high degree of rotational symmetry achieved at the center frequency, which is also typical of the lower portion of the band, while the higher frequency map of Figure 45 shows the pattern symmetry to be deteriorating. Figure 46 is typical of the port 1 cross-polarized patterns, showing the cross-polarized response to be greater than 30 db down in the principal planes and increasing to approximately 20 db down in the ± 45 degree planes.

The port 2 transmit patterns, shown in Figure 47, are slightly poorer than expected, showing the results of errors in mode phasing. The E-plane patterns are narrower than the H-planes throughout the band, and the side lobe level approaches -12 db at the upper frequency. The cross-polarized component is seen to be similar to that of port 1. The effects of the phasing error can be clearly seen in Figures 48 and 49, where the departure from rotational symmetry is quite evident. Some loss in illumination efficiency is naturally attendant to such pattern distortion, but, as will be seen in a later section, the reflectors tend to smooth out the primary patterns. The length of the phasing section should be increased by approximately 0.025 to 0.030 inch to improve the port 2 pattern characteristics.

Difference patterns of the $LSE_{1,1}$ coupler, port 3, are shown in Figure 51. These patterns, which provide for tracking in the elevation plane, are seen to be quite independent of frequency across the receive band, with a stationary deep null and only minor amplitude variation. The field map of Figure 52 shows the difference pattern to be well behaved considerably beyond the subreflector illumination area. The cross-polarized pattern shown in Figure 53 is worthy of comment, in that the cross-polarized characteristics

determine to a great extent the requirements to be placed on the polarizing network to be discussed in the following section. It is seen that the cross-polarized pattern is an azimuth difference pattern of nearly the same magnitude as the principal polarization. Therefore, any substantial cross-polarized energy in the feed network results in cross talk between the tracking channels. Such cross talk diminishes as an on-axis condition is approached, and only slowly degrades tracking stability as the polarization purity is compromised. An axial ratio of 0.5 db for the polarizer provides approximately 25 db rejection of the cross-polarized components, and is quite adequate for suppression of interchannel cross talk.

Azimuth plane tracking signals are derived from the $TE_{0,2}$ coupler, port 4. Patterns of this port, shown in Figure 54, are similar to those of the $LSE_{1,1}$ port, with stable, deep nulls across the frequency band and only minor amplitude variation. The preceding discussion of cross-polarization applies equally well to this port.

In general, the pattern characteristics of the deliverable feed network are considered excellent, and well within the goals of the contract effort.

2.2.5 Polarizing Network

The contractual statement of work requires that the design be capable of providing any combination of right and left circular polarizations for the transmitting and receiving channels. There are two primary considerations concerning performance of the polarizer. Very low ellipticity is required over the receive frequency band in order to maintain tracking nulls of satisfactory depth. An ellipticity of 0.5 db is an acceptable level in this context, while a value approaching 0.1 db is desirable. Ellipticities of 0.5 and 0.1 db result in cross-polarization levels of approximately -25 and -40 db, respectively. Ellipticity is directly proportional to loss in efficiency; therefore, it must be held as small as possible over both transmit and receive frequency bands.

A variety of techniques are available for producing a circularly polarized field, most of which are somewhat limited when a flexible, broadband device

is desired. Dielectric slabs or other phasing devices in waveguides or horns generally have limited bandwidth and are difficult to adapt for right and left sense changes. The optimum technique would involve a separable, external device which would impart circular polarization over a large bandwidth to a wave emanating from an arbitrary linear radiator. The characteristics of beam shaping would then be determined by the primary antenna and the circular polarization would be produced by an add-on device with minimal effect on other properties of the primary radiator.

Several such transmission polarizers have been reported in the literature (References 15 through 18), all based on the concept of a polarization-sensitive space filter which produces a 90-degree phase difference to orthogonal components of an incident linear field. The simplest configuration consists of several grids of parallel wires oriented at 45 degrees from the plane of the E-field. That component of E-field which is perpendicular to the wire grating passes essentially unperturbed, while that which is parallel to the grating experiences the required 90-degree phase shift. The more complex configurations utilize grids of meander lines (a square wave type of line) or of rectangles and straight wires. While the more complex configurations appear to offer the potential of better performance than the straight wire version, the published data available at the outset of the program showed the experimental results achieved with the straight wire configuration to be at least equal to those of other implementations. Therefore, the straight wire grid configuration was selected for development.

An experimental model of a wire grid polarizer (Figure 57) had previously been fabricated and tested under an MDAC IRAD program. Based on a somewhat limited analysis, a basic configuration of four grids with wire spacing (w) slightly greater than $\lambda/2$ and approximately $\lambda/4$ grid spacing (s) was selected. This model, designed for operation between 14 and 15 GHz, was fabricated to allow variations of these parameters about the basic values. Wire diameters (d) larger than 0.050 inch were found to cause unacceptable reflections back into the horn with small horn-to-grid spacings. Separation between horn and grid (h) also had a significant effect on performance. Data

CR10
SM544499

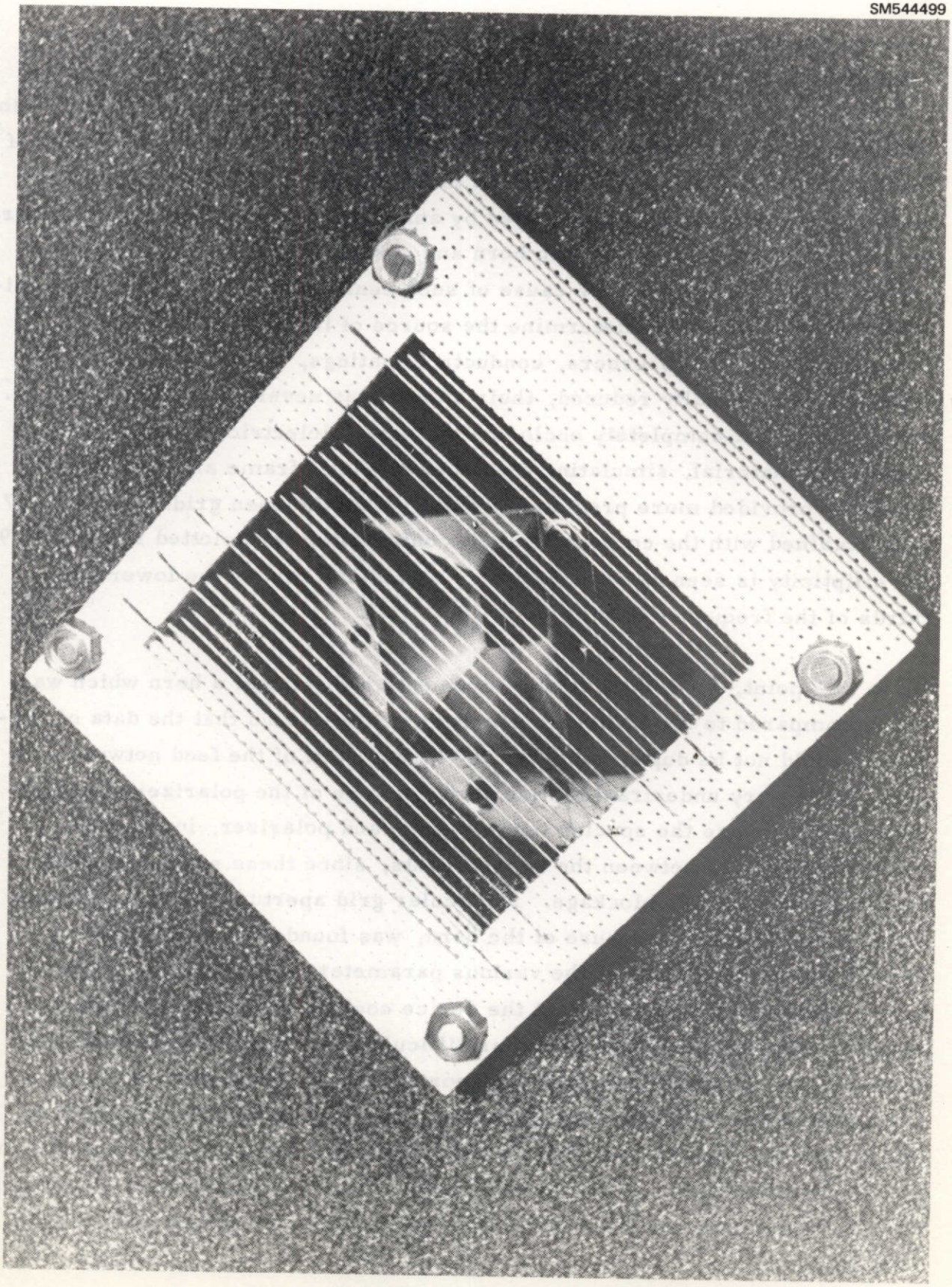

Figure 57. Prototype Polarizer

obtained with that model, shown in Figure 58, show an ellipticity less than 1 db over a bandwidth greater than 1 GHz is achievable, or a selected frequency band several hundred MHz wide could be held to approximately 0.1 db at the expense of increased ellipticity at other frequencies. Performance of the polarizer was extremely sensitive to minor changes in device geometry, to a far greater extent than indicated by analysis. Edge effects from the wire ends, strong interaction between horn and grids, or other resonance type effects were suspected as the cause of such sensitivity. A number of experiments was performed to determine the source of the disruptive effects, including the use of absorbers, conductive coatings, etc., but although the effects were gradually reduced, their source was never specifically located. It was found that completely enclosing the outer dielectric supports with a conductive material, simulating a continuous metal frame around the grid network, provided more predictable results than the open grids of Figure 57. Data obtained with the conductive shell configuration are plotted in Figure 59; the ellipticity is seen to be quite low, particularly across the lower two thirds of the frequency band.

Up to this point, all polarizer measurements had utilized a horn which was small compared to the polarizer aperture. It was found that the data of Figure 59 could not be duplicated when the larger horn of the feed network was used. It is very undesirable to increase the size of the polarizer or to substantially increase the spacing between horn and polarizer, in order to reduce interaction between the two elements, since these solutions would increase the aperture blockage. A circular grid aperture, with a diameter equal to the diagonal measure of the horn, was found to diminish (but not eliminate) the criticality of the various parameters. These effects were never overcome to the point that the device could be described analytically in more than gross terms. Another difficulty arose with usage of the feed network; the ellipticity achieved with ports 1 and 2 was slightly different for a particular polarizer configuration. This can readily be attributed to minor field perturbations in the vicinity of the difference coupler slots and to any slight deformation of the square guide or horn structure which might alter the local field polarization. While these differences were relatively small

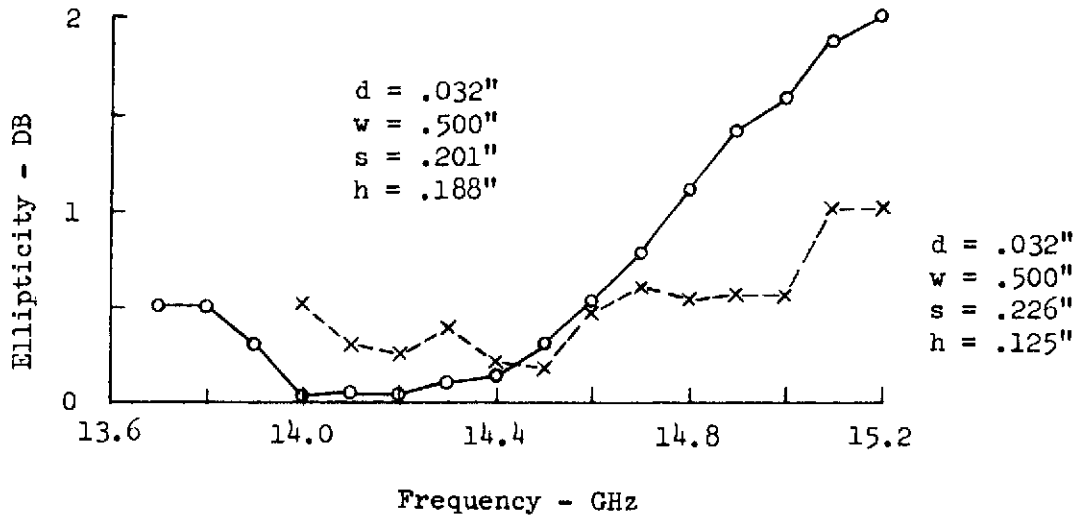

Fig. 58 Prototype Polarizer Ellipticity

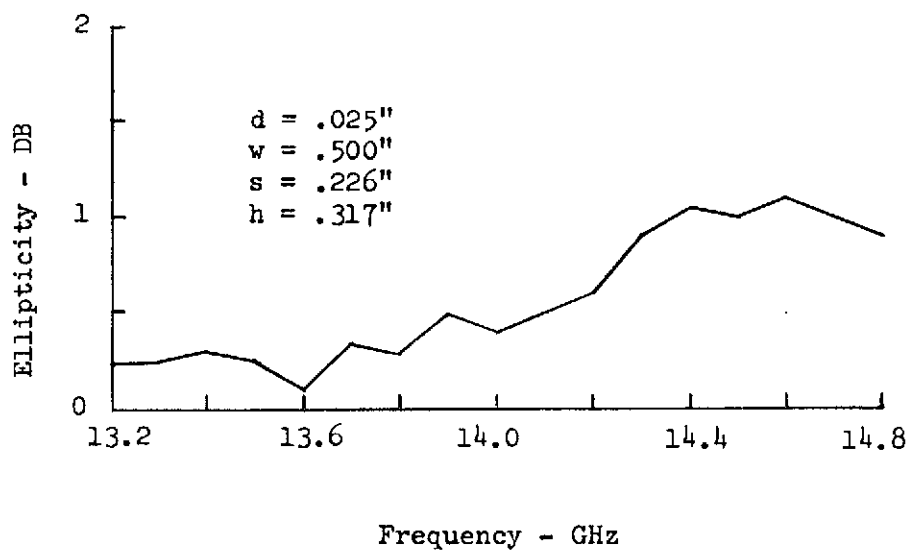

Fig. 59 Conducting Frame Polarizer

(on the order of 0.25 db), they required separate measurements and the ensuing compromise to determine optimum parameters for total subsystem operation.

The final polarizer configuration, mounted on the prototype feed network, is shown in Figure 60. This configuration used a tapered spacing between grids which seemed to improve the bandwidth characteristics. Drill rod was used as the wire elements in order to maintain the wire geometry to a satisfactory degree. Figure 61 depicts the network configuration, and the final eccentricity data are plotted in Figure 62. In order to facilitate handling and prevent damage to the wire structure, slabs of 2-lb/ft^3 foam dielectric were used to fill the spaces between rows of wires, and the entire unit was covered by a single ply of 4-mil fiberglass cloth. The final data are not as good as those achieved with the configuration of the prototype polarizer upon which the deliverable unit was based, which exhibited less than 0.5-db eccentricity from 13.2 to 14.0 GHz, and between 1.0 and 1.5 db across the transmit frequency band. This difference appears to be due only to manufacturing tolerances and indicates the remaining degree of geometrical sensitivity. Further effort toward optimization of the polarizer network would appear to be significantly beneficial.

Effects of the polarizer on the VSWR and isolation of the various ports of the feed network are negligible. Pattern change due to the polarizer was less than the pattern measurement accuracy in the principal polarizations; cross-polarization levels increased from the -30 db of the linear configurations to the area of -25 db for the circular version. Digital field maps did provide an indication of slight off-axis, nonprincipal plane pattern distortions due to the polarizer, resulting in small, local departures from the desired rotational symmetry. Tracking null depths remained essentially the same, some greater and some less than those of the linear network, but all better than -30 db which provides very accurate and stable tracking.

The deliverable circularly polarized feed assembly is shown in Figure 63. The feed assembly is presently configured for receiving right-hand circular and transmitting left. To adapt to left circular receiving and right circular

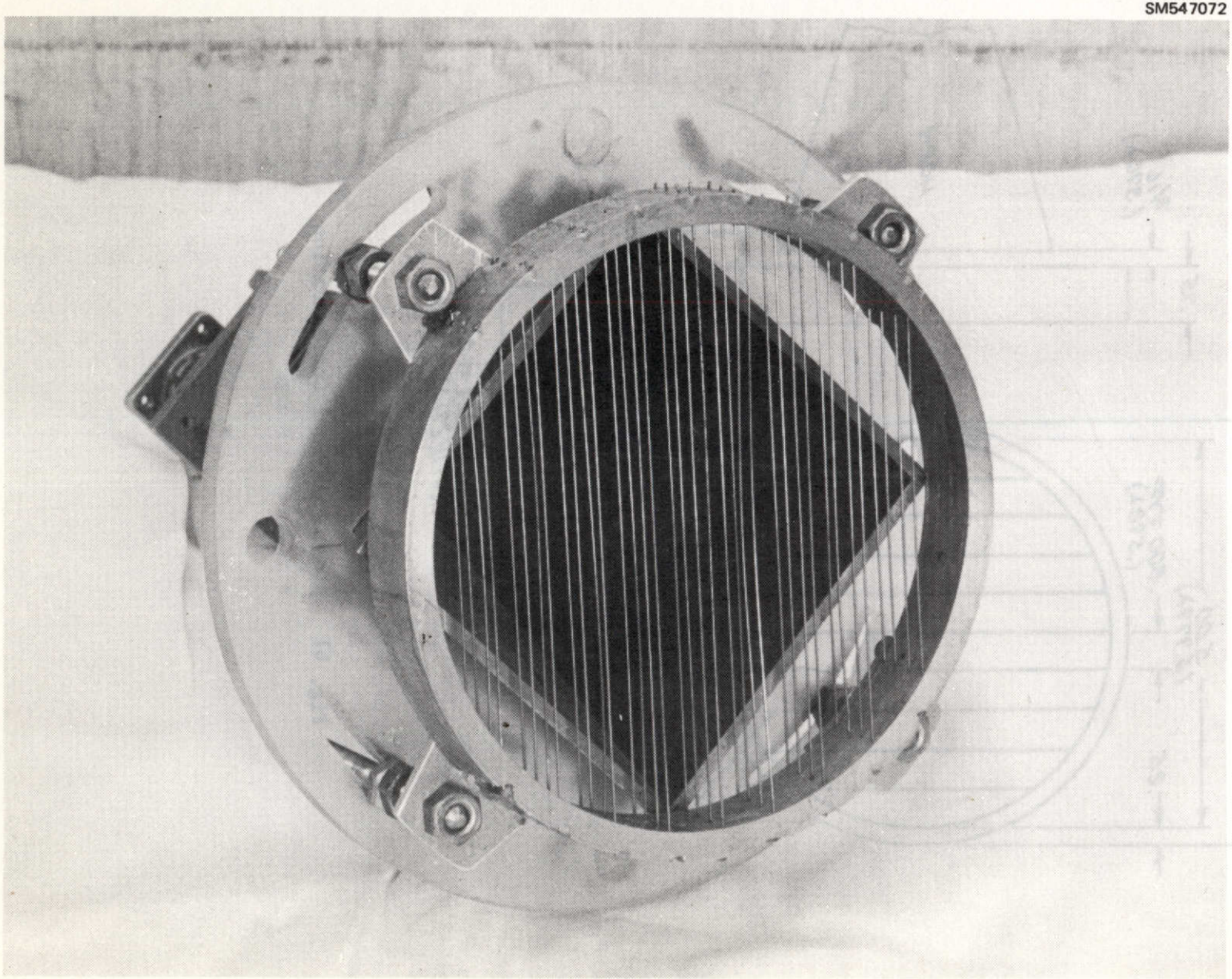

Figure 60. Final Polarizer Configuration

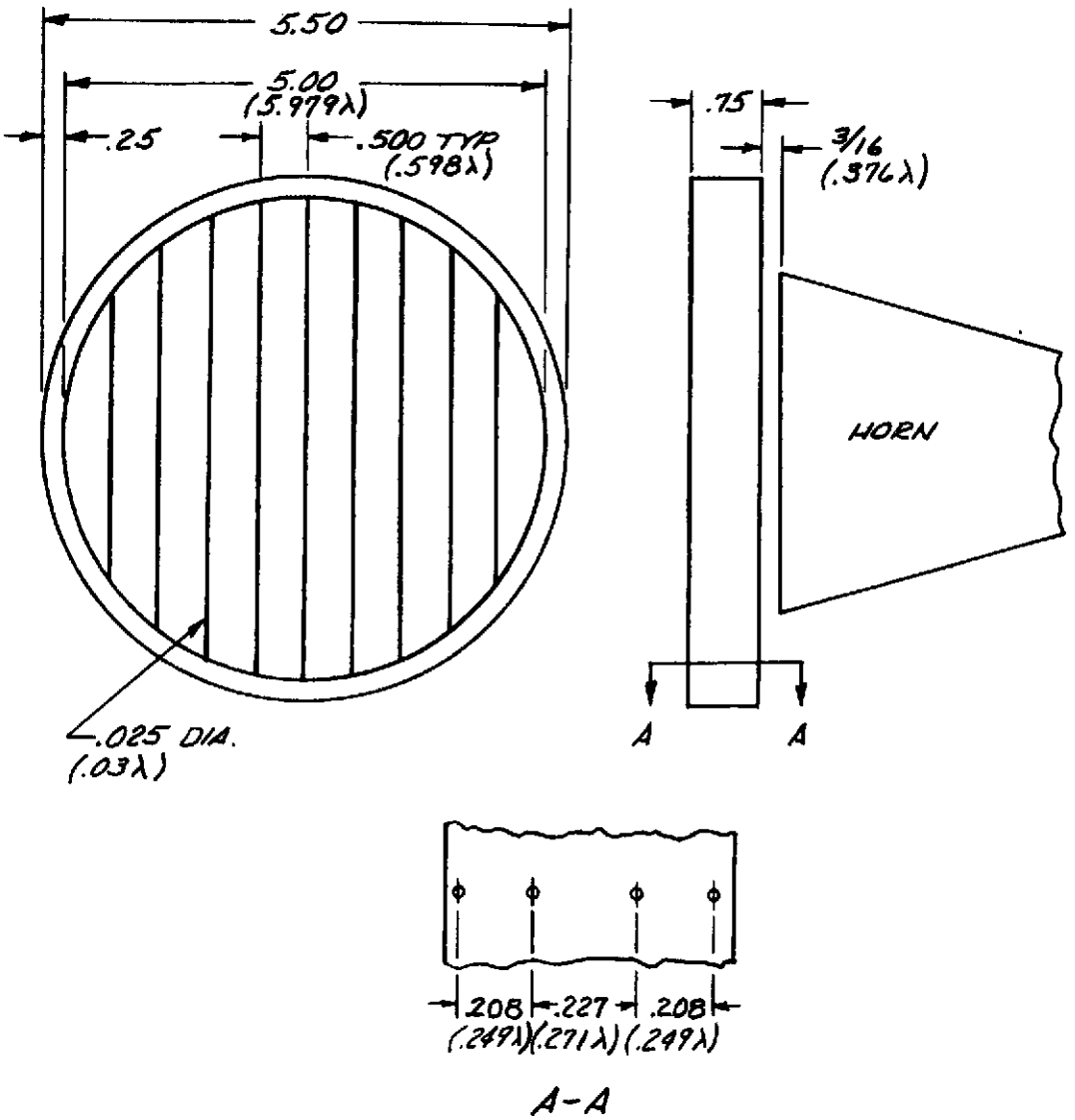

Fig. 61 Final Polarizer Configuration

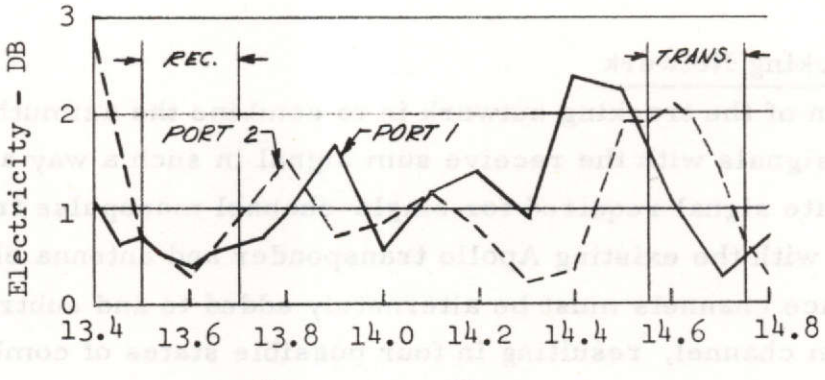

Fig. 62 Final Polarizer Data

CR10
POLAROID

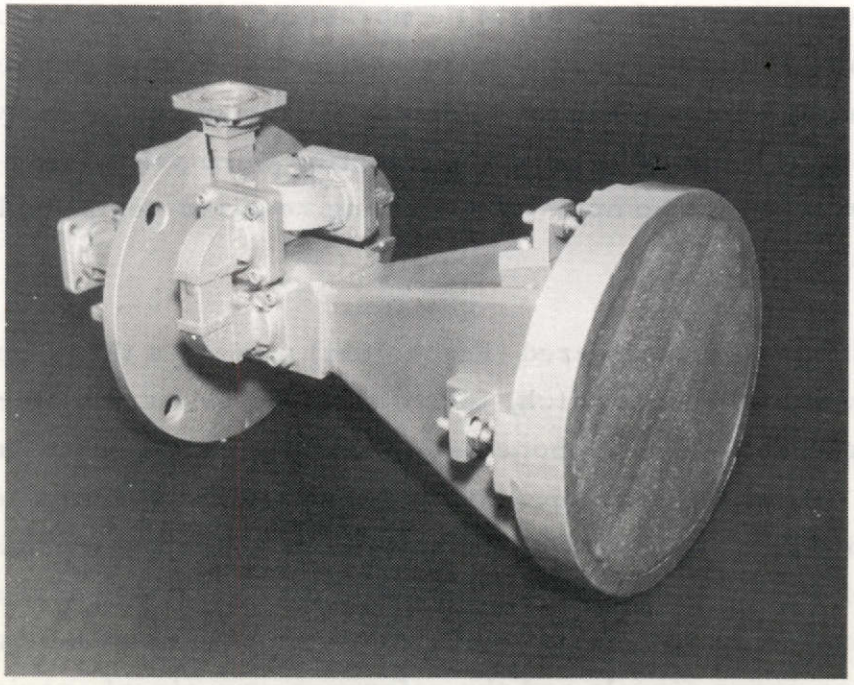

Figure 63. Feed Assembly with Polarizer

transmission requires only that the polarizer be rotated 90 degrees with respect to the feed network. Care should be exercised to maintain the 3/16-inch spacing of horn to polarizer after making this change.

2.2.6 Tracking Network

The function of the tracking network is to combine the azimuth and elevation difference signals with the receive sum signal in such a way as to provide the composite signal required for single-channel monopulse tracking. To be compatible with the existing Apollo transponder and antenna electronics, the RF difference channels must be alternately added to and subtracted from the receive sum channel, resulting in four possible states of combination: + elevation, + azimuth, - elevation, and - azimuth, in that sequence. Control signals for the sequence are provided from the NASA-MSC antenna electronics in the form of two 50 Hz, +3V to -50V square wave signals (FTD I and FTD II) in phase quadrature. The network required to perform this function is shown in Figure 64.

As originally conceived and proposed, the network was to be implemented with ferrite devices for the switching and phase-shifting elements. A survey of available components and complete networks and extensive discussions with device manufacturers resulted in several potential configurations, most of which would require some measure of device development for operation at our frequencies. The criteria used for selection were primarily cost of implementation, network complexity (including required peripheral hardware), and reliability.

The basic configuration considered (Figure 65a) utilizes a three-port switchable circulator as the switch, followed by either a circulator or a differential phase shifter. Components for this configuration are available with minimum component development, and the cost of RF components is on the order of $3,000. The major disadvantage encountered with this implementation involves the sensitivity of absolute insertion phase of the ferrite devices to temperature variation. Since relative phase must be maintained between tracking error signals and the reference sum signal, variations in

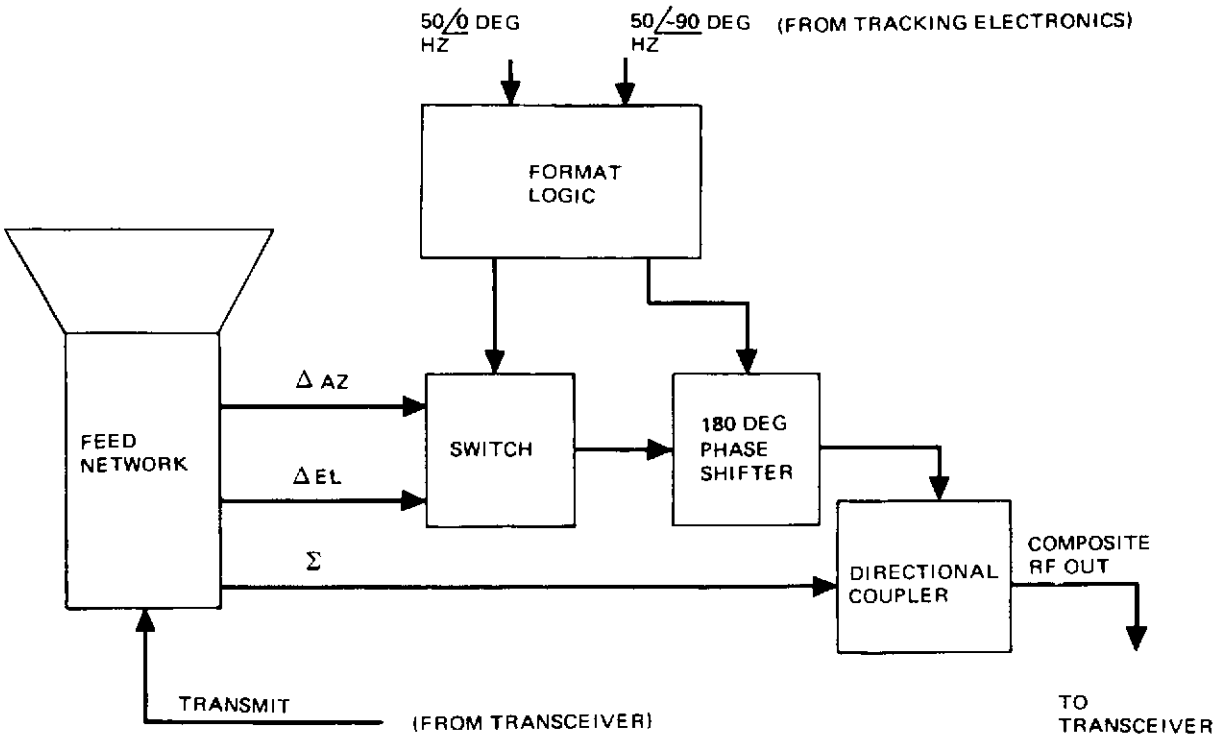

Figure 64. Tracking Network Configuration

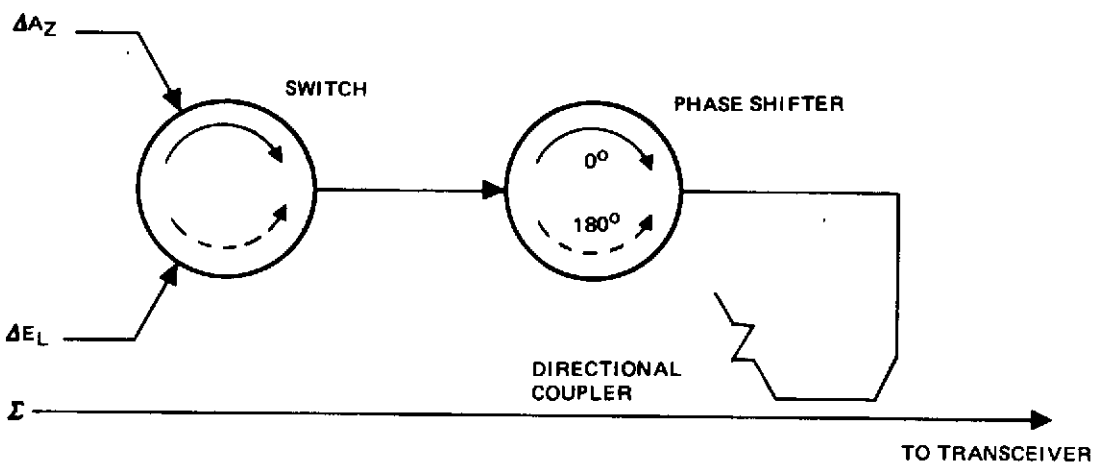

A. ORIGINAL CONFIGURATION

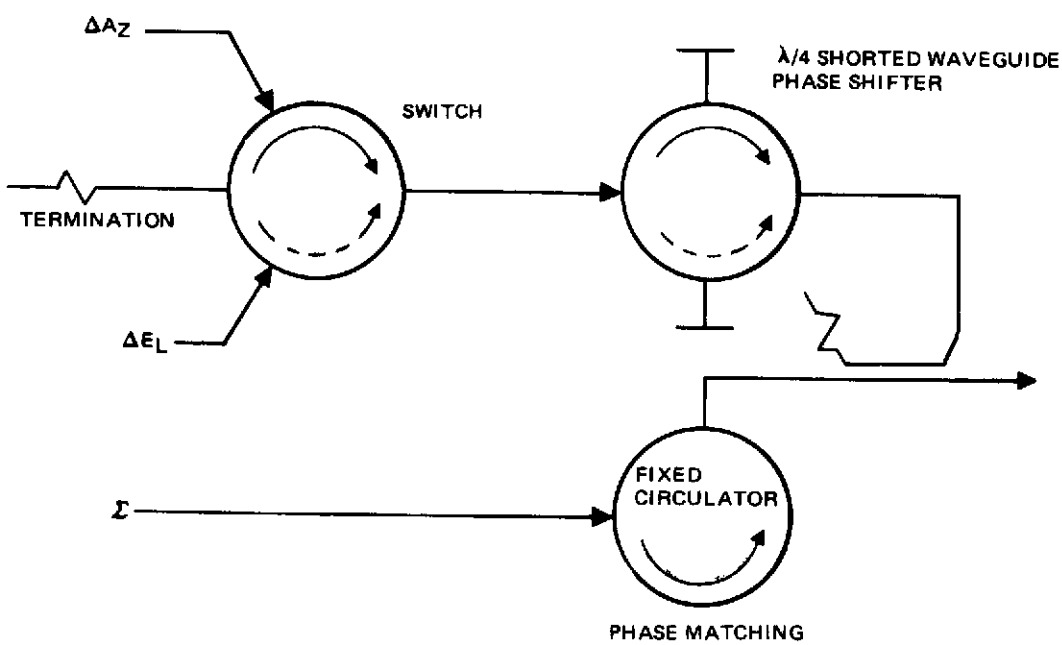

B. ALTERNATE CONFIGURATION

Figure 65. Possible Network Implementations

insertion phase between the feed network and receive channel combiner must be avoided. Most manufacturers of ferrite devices enclose them within active, temperature-controlled packages, which is unattractive from a cost, reliability, and prime power viewpoint for spacecraft applications. In addition, it can be seen that the unused error signal is routed, in the three-port circulator, back to the other error port. Isolation within the switch is adequate to keep this signal from degrading the desired tracking signal directly, but reflections in the feed network, or close coupling between the azimuth and elevation coupling ports within the feed, might be sufficient to cause serious error-channel cross coupling. An improvement on this scheme is shown in Figure 65b, where a four-port circulator is used for the switch. Here the unused error signal is routed to a termination and acceptable difference port isolation is achieved. The phase shift is also accomplished with a four-port circulator, with orthogonal ports terminated in short circuits placed to provide a 180-degree phase difference in the two paths. A fixed circulator, with insertion phase equal to the total phase of the switch and phase shifter and with similar phase-temperature characteristics, can be inserted in the receive sum arm to maintain phase balance over the full operating range of the ferrite material without the requirement for a temperature-controlled package. Although the devices required for implementation of this configuration appear feasible, development costs were estimated to be between $10,000 and $25,000 and satisfactory operation over the desired temperature range remains questionable.

The most viable proposal for a ferrite configuration was offered by Electromagnetic Sciences, Inc. That firm proposed a modification of an existing complete network, as diagrammed in Figure 66. Proposed insertion loss (1 db maximum), isolation (20 db minimum) and other pertinent specifications for this unit were excellent, but for an operational temperature range of -40° to +126° F, a 115 volt, 2 amp (maximum) heater supply is required. The unit is housed in a rather large container (which could be minimized for flight applications) and required additional power conversion and logic interface equipment for compatibility with the Apollo-type hardware. The price of the network was quoted to be $3,500.

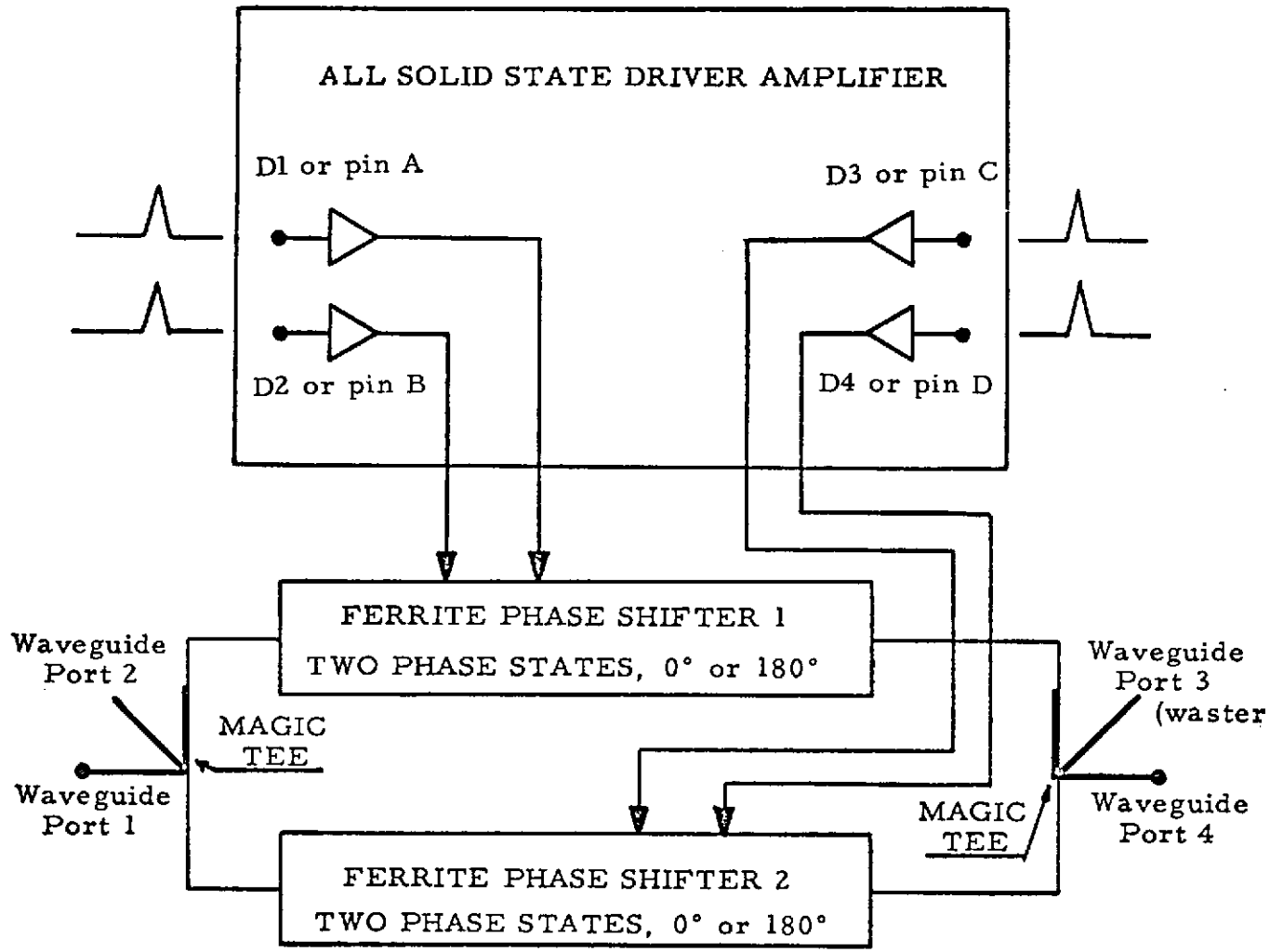

Figure 66. Block Diagram of Error Signal Sampler

An alternative to the ferrite configuration, utilizing diode SPST switches, is shown in Figure 67. This configuration offers the advantage of minimal phase-temperature sensitivity with no heater requirement, insertion loss comparable to that obtainable with ferrite devices, unused difference channel power is terminated rather than reflected back to the feed, and the network is relatively inexpensive, compact, lightweight, and producible. The only active elements in the device are four diode waveguide shorting switches. Azimuth and elevation difference signals are input to the E and H arms of a folded hybrid tee. The output arms of the tee each feed a hybrid coupler whose outputs are terminated with a diode shorting switch followed $\lambda g/4$ later by a fixed-waveguide short. Turning on the diodes thus changes the location of the short position by 90 degrees, and results in a 180-degree phase shift at the coupler output. Coupler outputs are connected to colinear arms of a second hybrid tee, of which one output is terminated in a matched load. Depending on the state of each pair of diode switches, either azimuth or elevation signal in either a 0- or 180-degree state is routed to the output and the other difference signal is routed to the termination. Since the phase shift is determined only by the spacing between diodes and fixed shorts, the device is quite insensitive to temperature variations, but is limited in operating bandwidth. As will be seen, the bandwidth achievable is adequate for this application but not for much more. Insertion loss of the network is dependent upon the state of the diode switches, being minimum when all diodes are shorted and maximum when all diodes are open. This results in a slight bias to the tracking null of one channel at large boresight angles but disappears as the boresight condition is approached. The cost of implementing this configuration was estimated at $3,000.

The final choice for implementation of the tracking network was between the ferrite configuration offered by Electromagnetic Sciences, Inc. and the diode configuration described above. Costs of the two versions, both for the breadboard unit and for subsequent production, are approximately the same. The ferrite configuration offered better bandwidth and required no development, so that its performance parameters were reasonably assured. Insertion loss of the diode configuration was somewhat questionable, as was its bandwidth

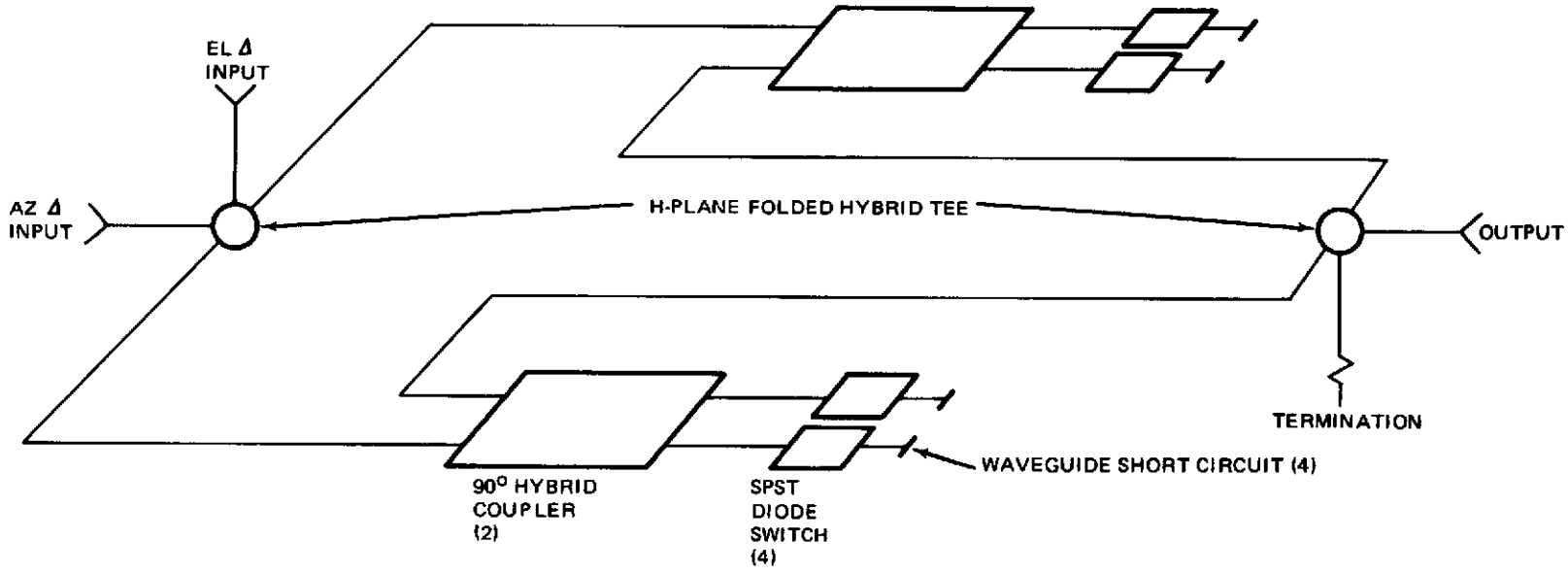

Figure 67. Solid State Tracking Network

capability. Reliability of the individual devices appeared to be equal, based upon the information obtained from various suppliers, but the increased complexity of the ferrite configuration (primarily in the thermal control hardware) suggests a lesser reliability factor for that network. It was decided to build the diode configuration so that its performance could be evaluated against the benefits of eliminating the thermal control system of the ferrite configuration.

Satisfactory diode switches were obtained from Microwave Associates, Inc. Specifications for the switches included an insertion loss of 0.5 db maximum and a minimum isolation of 20 db across the 13.5- to 13.7-GHz bandwidth. Measured parameters of the delivered devices ranged from 0.3- to 0.45-db insertion loss and 24- to 28-db isolation.

The network was first assembled with variable waveguide shorts in place of fixed shorts. With the variable shorts set at $\lambda g/4$, the data of Table 5 were obtained. It can be seen that the insertion loss is generally higher than desired, varying from 0.5 to 1.7 db, the phase shift in the azimuth channel varies ±20 degrees at the band edges, and interchannel isolation is not sufficient at the band edges. The expected insertion loss unbalance between the two states of the azimuth channel is also quite evident. Empirical optimization of the short positions resulted in the improved performance of Table 6. Fixed waveguide shorts were then machined to match the electrical lengths of the optimum variable short positions.

The results achieved with the diode configuration are seen to be comparable to those of the ferrite version over the bandwidth required. The channel isolation can be seen to be approaching -20 db at the band edges, however, and it appears that for a requirement involving any substantially wider bandwidth, the ferrite configuration would appear more appropriate.

Operation of the tracking network is pictured in the scope trace of Figure 68a. For this demonstration, receive sum and difference signals were developed in the network of Figure 68b. The two difference signals were modulated with different audio waveforms for identification. The upper trace in the photograph is one (equivalent to FTD I) of the two control signals, the second

Table 5

PRELIMINARY TRACKING NETWORK PERFORMANCE

Channel	Switch State Pair A	Switch State Pair B	13,500 GHz Insertion Loss (db)	13,500 GHz Relative Phase (deg)	13,500 GHz Isolation (db)	13,550 GHz Insertion Loss (db)	13,550 GHz Relative Phase (deg)	13,550 GHz Isolation (db)	13,600 GHz Insertion Loss (db)	13,600 GHz Relative Phase (deg)	13,600 GHz Isolation (db)	13,650 GHz Insertion Loss (db)	13,650 GHz Relative Phase (deg)	13,650 GHz Isolation (db)	13,700 GHz Insertion Loss (db)	13,700 GHz Relative Phase (deg)	13,700 GHz Isolation (db)
+ Elevation	High	Low	1.55	180	15	1.60	180	19.4	1.40	180	24.8	1.25	180	21	1.70	180	15.9
+ Azimuth	High	High	0.65	0	32	1.00	0	38	0.67	0	45	0.60	0	42	0.50	0	34.2
- Elevation	Low	High	1.40	0	11.6	1.50	0	17.4	1.15	0	26.7	1.10	0	21	1.40	0	14
- Azimuth	Low	Low	1.60	159	27	1.70	171	30	1.60	180	33.3	1.50	188	36	1.30	197	32.8

CR10
POLAROID

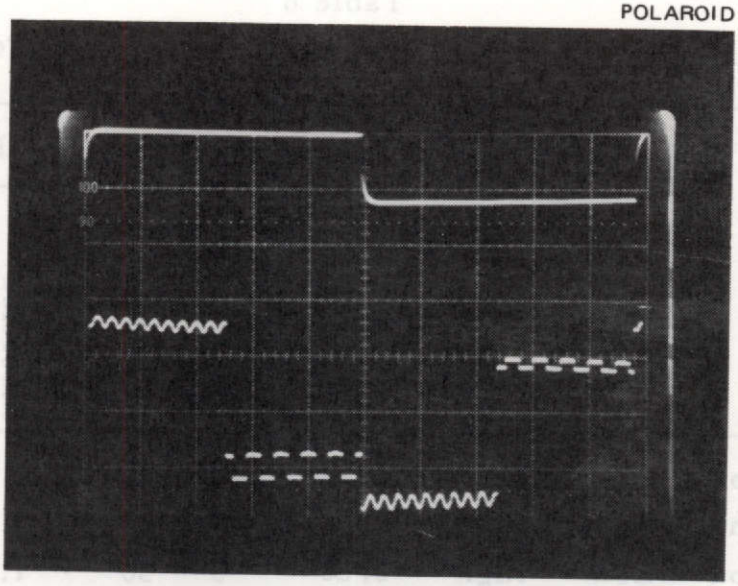

Figure 68A. Tracking Network Operation

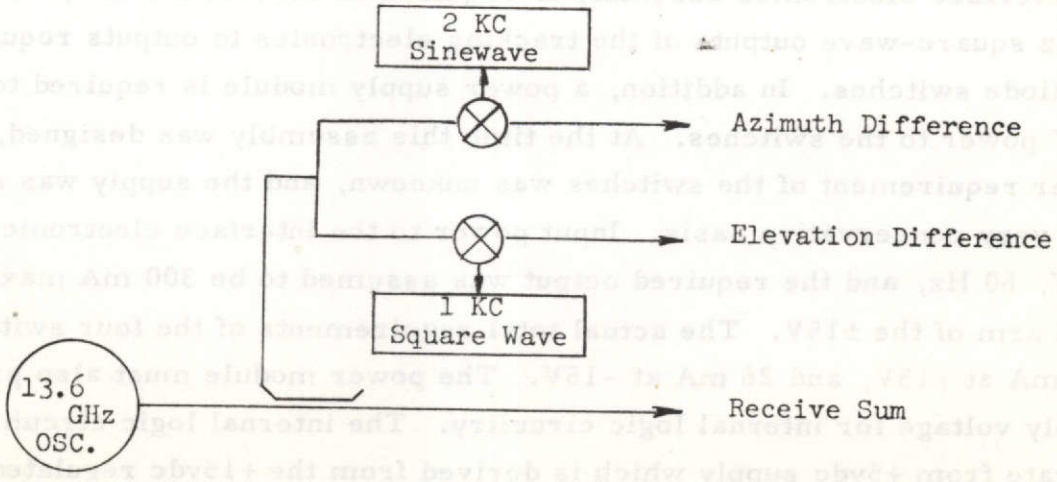

Fig. 68b Tracking Signal Synthesis

Table 6

FINAL TRACKING NETWORK PERFORMANCE

Channel	Switch State Pair A	Switch State Pair B	Center Frequency Insertion Loss (db)	Center Frequency Relative Phase (deg)	Center Frequency Isolation (db)	Band Edge (Typ) Insertion Loss (db)	Band Edge (Typ) Relative Phase (deg)	Band Edge (Typ) Isolation (db)
+ Elevation	High	Low	0.25	180	23	1.20	180	22
+ Azimuth	High	High	0.50	0	25.5	0.65	0	25
- Elevation	Low	High	0.60	0	30	1.30	0	22
- Azimuth	Low	Low	0.50	179	36	0.75	172	27

of which lags that shown by 90 degrees. At the leading edge of the control signal, the azimuth error signal is added to the reference sum. During the next quarter cycle, the elevation error signal is subtracted from the reference. The following quarter cycles subtract the azimuth and add the elevation, in that order. The control state sequence is given in Figure 69.

An interface electronics assembly is required to convert the +3V, -50V, 50 Hz square-wave outputs of the tracking electronics to outputs required by the diode switches. In addition, a power supply module is required to provide ±15V power to the switches. At the time this assembly was designed, the power requirement of the switches was unknown, and the supply was selected on a very conservative basis. Input power to the interface electronics is 115V, 60 Hz, and the required output was assumed to be 300 mA maximum on each arm of the ±15V. The actual total requirements of the four switches is 120 mA at +15V, and 26 mA at -15V. The power module must also provide supply voltage for internal logic circuitry. The internal logic circuits will operate from +5vdc supply which is derived from the +15vdc regulated output. Total current drain from the logic power will not exceed 50 mA.

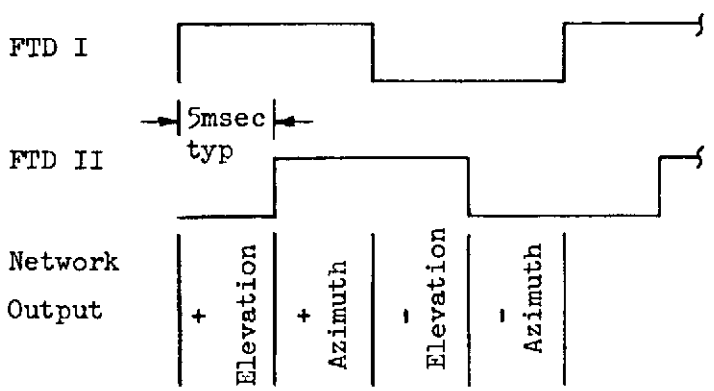

Fig. 69 Control State Sequence

A Monsanto MCL 600 integrated circuit (IC) is used to accomplish the logic conversion. This IC contains an optically isolated logic gate, which maintains a high degree of isolation between the input and output of the converter circuit. The circuit schematic is shown in Figure 70, with an equivalent circuit of the tracking electronics signals.

When the input voltage is at +3 volts, input current, I_F to the MCL 600 is

$$I_F = \frac{E_2 - V_{CE(SAT)} - V_F}{R_2}$$

$$= \frac{3.0 - 0.4 - 1.15}{1K} = 1.45 \text{ mA}$$

The worst-case current required to switch the MCL 600 is 1.2 mA; therefore, the output will change from logic 1 (3.5vdc) to logic 0 (0.2vdc). When the input is switched to the opposite condition, the input LED is reverse biased so that the output returns to the logic 1 state. Input diode reverse voltage is limited to one diode drop by DR1. The maximum reverse voltage for the LED used in the input to the MCL 600 is 3V.

A test circuit was included in the design of this assembly to provide simulated FTD I and FTD II signals. This circuit, when operating, will switch the optically coupled isolation circuits so that the TTL compatible outputs are switched at 50 Hz in a phase quadrature relationship similar to the FTD I/ FTD II input signals. This circuit consists of three integrated circuit packages and several discrete components. Two one-shot multivibrators are used to produce a 100-Hz clock pulse. This clock pulse is then used to clock a dual J-K flip-flop circuit to provide the desired output. A schematic diagram of this circuit is presented in Figure 71.

It is necessary to provide +5 volt dc power for the operation of the logic level converter circuits as well as the integrated circuits used to provide the test output capability. In order to conserve power, the test circuit design incorporated low-power TTL circuits. The total IC current requirement is 18 mA for normal operation and 43 mA in the test mode.

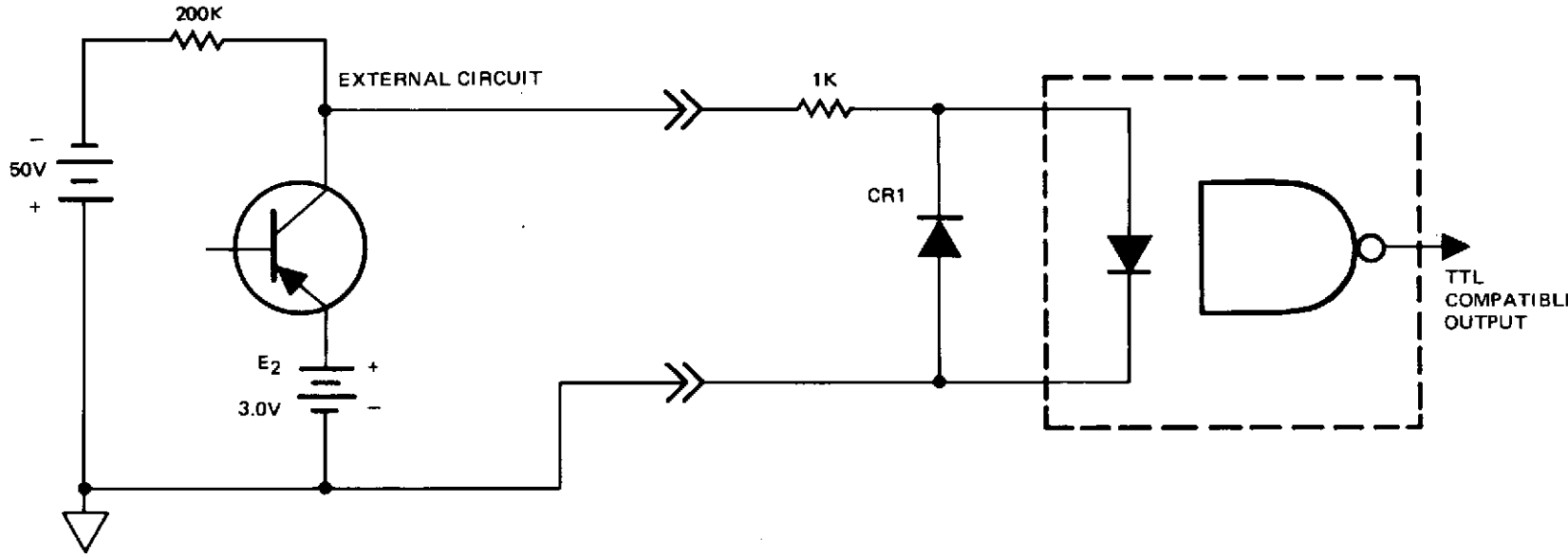

Figure 70. Logic Level Converter Schematic

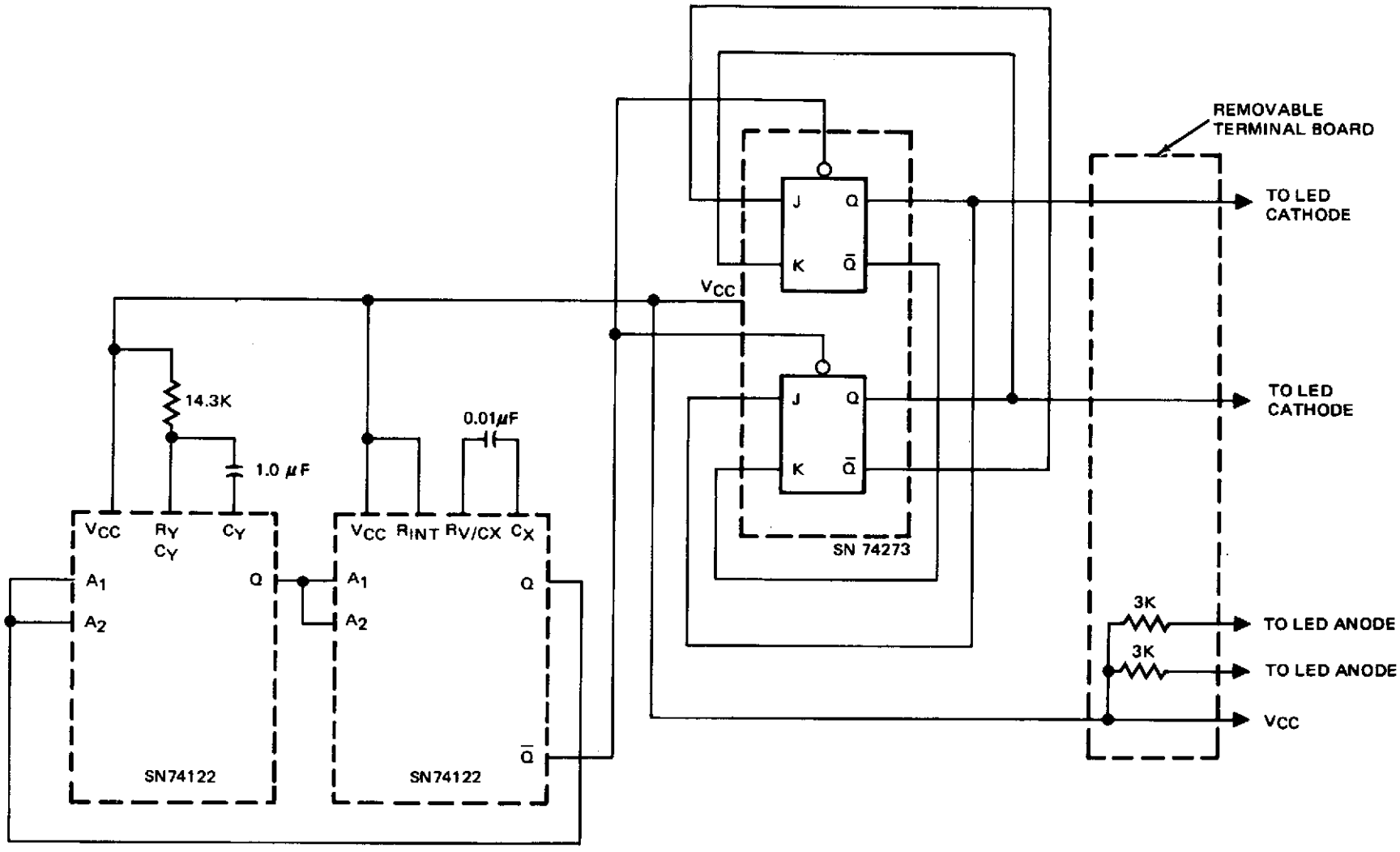

Figure 71. Test Circuit Schematic

An LM309 5-volt regulator is used to derive 5V logic voltage from the 15V supply. This unit is available in the TO-5 package and is capable of supplying 50 mA of current at 50°C with no heat sink. No external components are required for the operation of this circuit; however, a 10-μf capacitor will be used across the output to provide decoupling for the TTL circuits.

The integrated circuits and discrete components for this assembly are contained on two connectors which are designed to accommodate dual in-line packages. The layout of the hardware is shown in Figure 72. Input/output connections are made through the use of a 16-pin component socket adapter and discrete components are mounted on the same type of adapter. The large adapter card, covering pins 1 through 8 of rows A, B, C, and D, contains the crossover wiring for insertion of the test output signals. When this board is in place as shown, the simulated FTD signals will be present at the output. For operation from the external inputs, this board must be removed. During normal operation, the test circuits are not powered. The switching logic signals are brought out from the electronics board to two OSM coax connectors, and are connected to the switches through solid-jacket coax cables.

This assembly, including power supply, electronics, and microwave switching hardware, is packaged in an aluminum housing which will provide protection from the elements during outdoor, year-round range measurement usage. The directional coupler for combining the sum and difference signals is mounted to one side of the box. Tracking signals and prime power are introduced to the assembly through two hermetic connectors. Mating plugs for these connectors are provided. The complete tracking network is shown in Figure 73, with all ports and connectors appropriately designated.

2.2.7 Antenna Assembly

The antenna reflector and support structure delivered under this contract was of conventional aluminum construction; no attempt was made to optimize the structural weight characteristics of that assembly. It was required, however, that the configuration selected must have the potential of lightweight implementation, and the lightweight design data are provided.

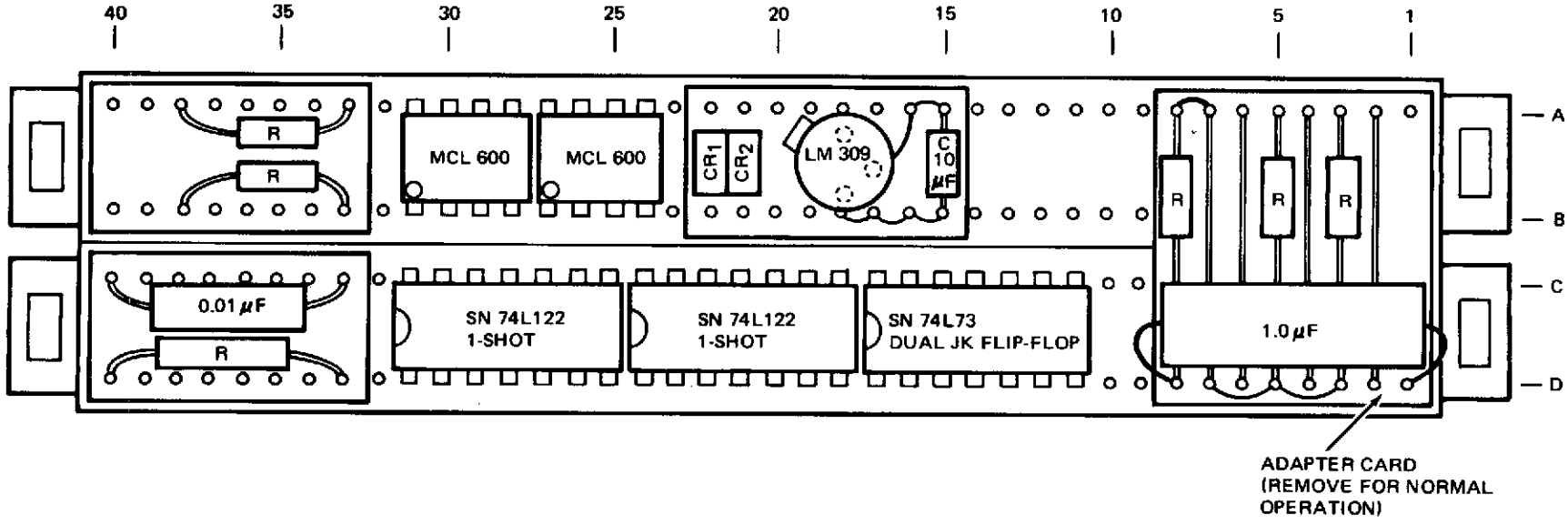

Figure 72. Electronic Circuit Subassembly

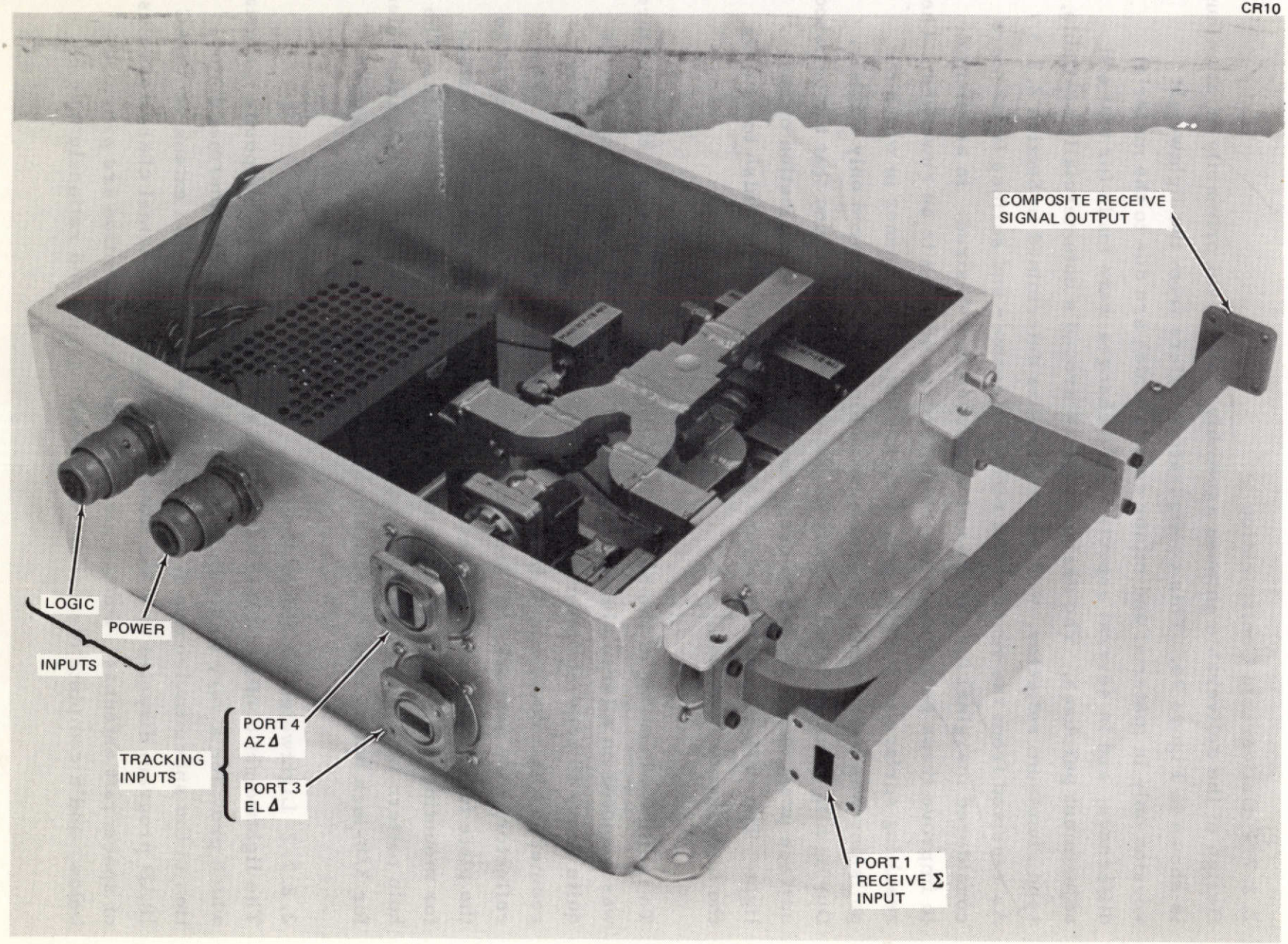

Figure 73. Tracking Network Assembly

2.2.7.1 Deliverable Configuration

Design of the deliverable antenna assembly, fabricated primarily of aluminum, is shown in Figure 74. This configuration differs from the lightweight version only in material and minor details which are due to the material difference, and in several aspects where changes were made for test and adjustment purposes. The design is based around a commercially available, spun aluminum reflector, with parameters as determined in Section 2.2.3. As received from the vendor, the reflector contour and surface finish were considered marginal for the type of measurements desired. In an attempt to improve these parameters the reflector was sent out to be reworked. The resulting surface was highly polished, but due to the manner in which the polishing was performed, the surface contour was improved only slightly. During alignment and test activity on the range, it was found that the polished surface presented a danger to personnel due to focused reflection of sunlight. The reflector was therefore given a light sandblast finish to remove the high degree of polish.

To facilitate handling of the assembly during test and shipment, the structure was mounted on a large aluminum plate. The plate was intentionally made quite heavy to prevent distortions of the reflector and the feed/reflector geometry which could result in erroneous and misleading test data. The reflector, feed network, and tracking network are independently mounted to the plate for maximum ease in accomplishing adjustments. A hole pattern for mounting the plate to an antenna positioner is provided in the plate. The hole pattern is 17 inches in diameter, with six equally spaced clearance holes for 3/8-inch bolts. The overall antenna assembly is shown in Figure 75.

2.2.7.2 Lightweight Configuration

The lightweight configuration is based on a graphite/epoxy composite material which provides a very lightweight structure with negligible thermal distortion in the space environment. The design is a result of an extensive MDAC IRAD program directed at optimization of weight and thermal characteristics of spacecraft antennas. Design details of this configuration are provided below, and a complete discussion of supporting data and rationale may be

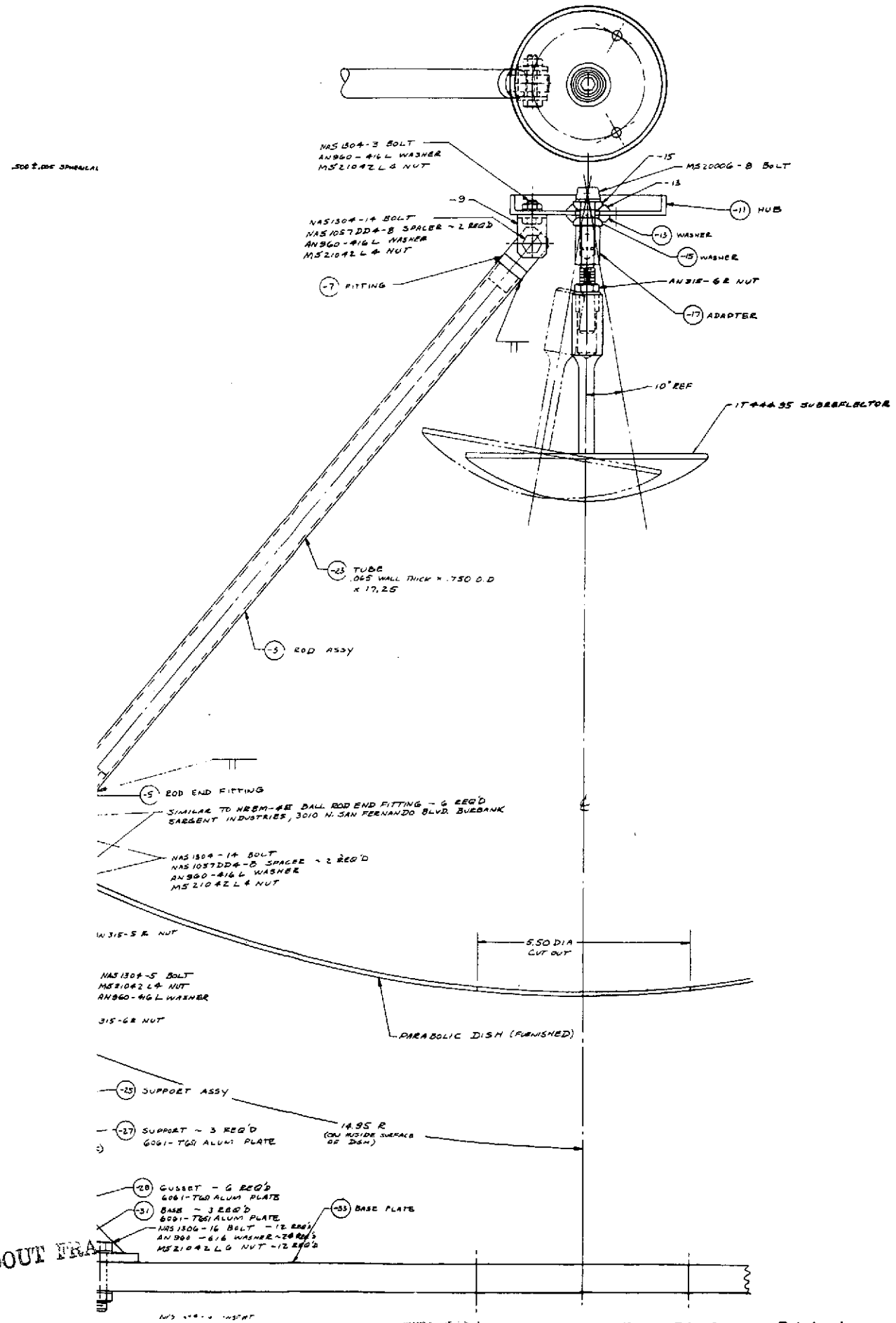

FOLDOUT FRAME

FOLDOUT FRAME

Figure 74. Antenna Fabrication

CR10
POLAROID

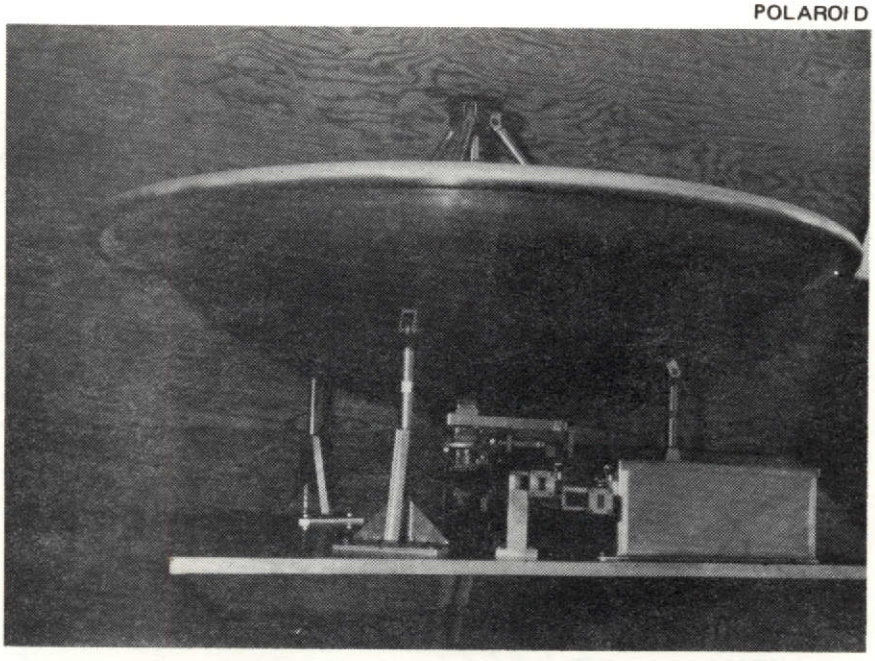

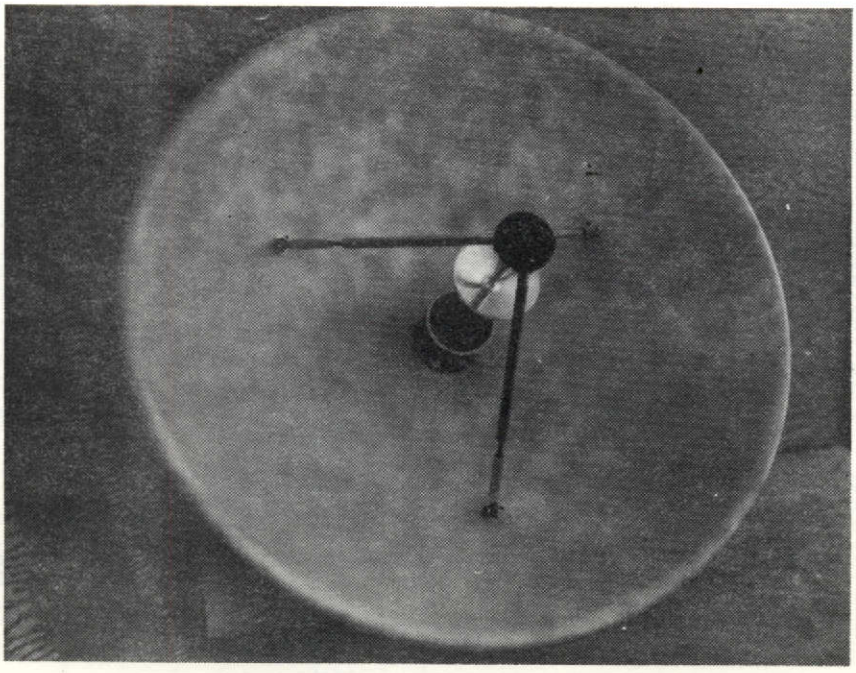

Figure 75. Complete Antenna Assembly

found in the IRAD report, "Research and Development in the Use of Graphite/ Epoxy Composites in the Fabrication of Low Distortion Structures," MDC G4035, which is provided as Addendum 1.

Figure 76 gives a general view of the design of the 4-ft-diameter antenna. Figure 77 shows detailed views of the design. The dish is in accordance with MDAC proprietary design. The basic material used in this design is Modmor I graphite continuous filament (tow) tape prepreg with epoxy resin 828CL. This resin system has to be used if the present established lost-wax process is to be used. It is to be noted that there are nine ribs. This requirement of having the ribs in multiples of three's is to maintain axial symmetry with respect to the tripod supporting the subreflector.

Provisions for attachment of the feed horn were not made because details of a flight-weight model have not been established. Three attach points are provided on the antenna for attaching to the space vehicle.

All metal fittings and bolts are made of titanium instead of aluminum because their α is about 5.3×10^{-6} in./in./°F versus that of about 13×10^{-6} in./in./°F for aluminum. The density of titanium is about 0.16 lb/in.^{3} versus 0.1 lb/in.^{3} for aluminum. Some weight reduction can be made by drilling concentrically through some of the fittings. Another approach to the fittings is to make billets out of chopped graphite fiber and epoxy and then machine them to the required contour. Some of the fittings may be made in this manner. The advantage will be a still lower α and less weight.

The reflective face is made of six plies of $(0° \pm 60°)_S$ for a balanced construction. The ribs and rings are made by spiral wrapping over wax rods and also using tape running in the direction of the length of the member.

A typical joint is shown in Figure 77. This is the joint at which the subreflector struts attach to the reflector. The other face of this joint serves as the attach points of the antenna. At the joint the tube is filled with a preform by making a preform billet in a press and then cutting to the required configuration. This preform is inserted in the rib during fabrication and the joint is

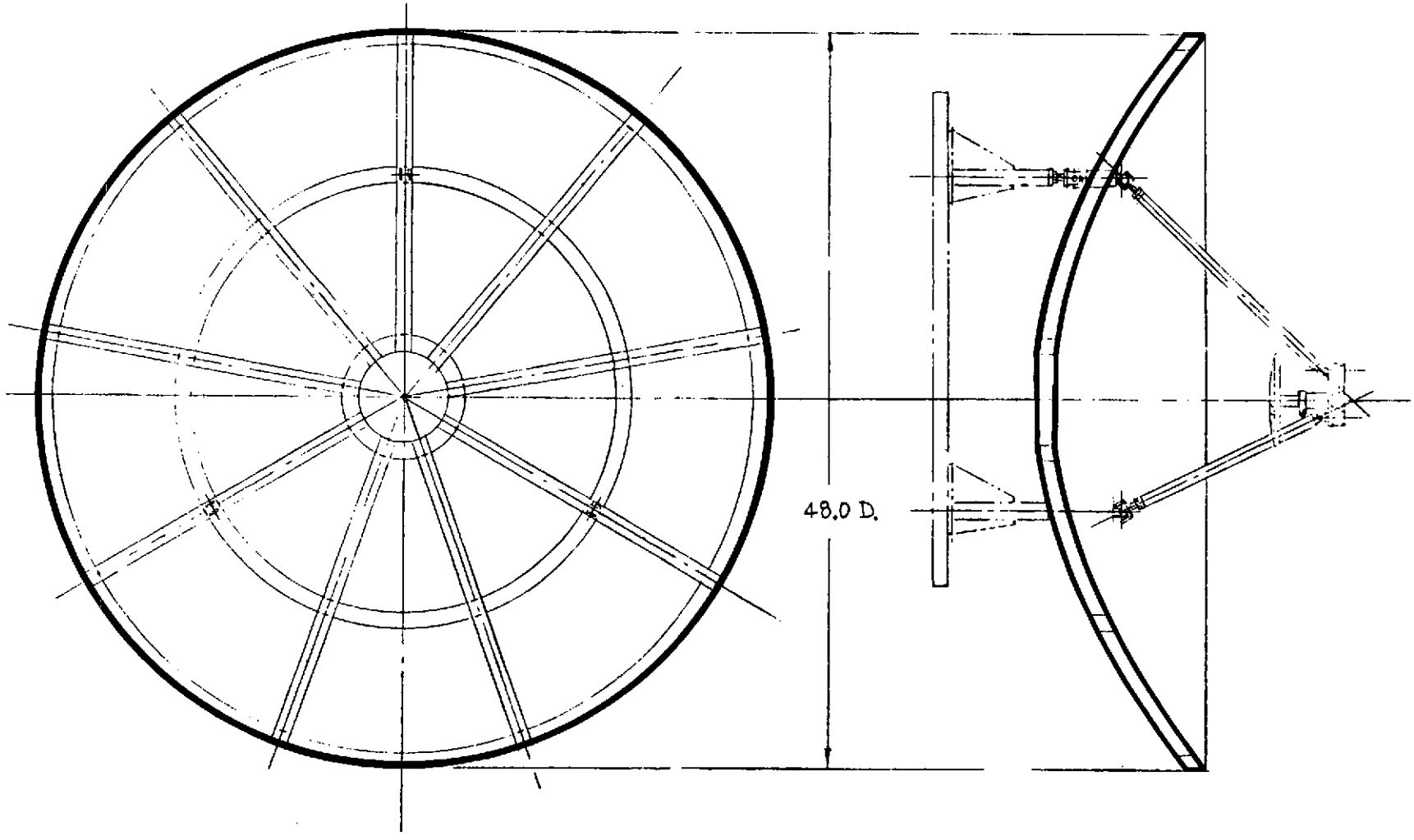

Figure 76. 4-Ft-Dia Parabolic Antenna

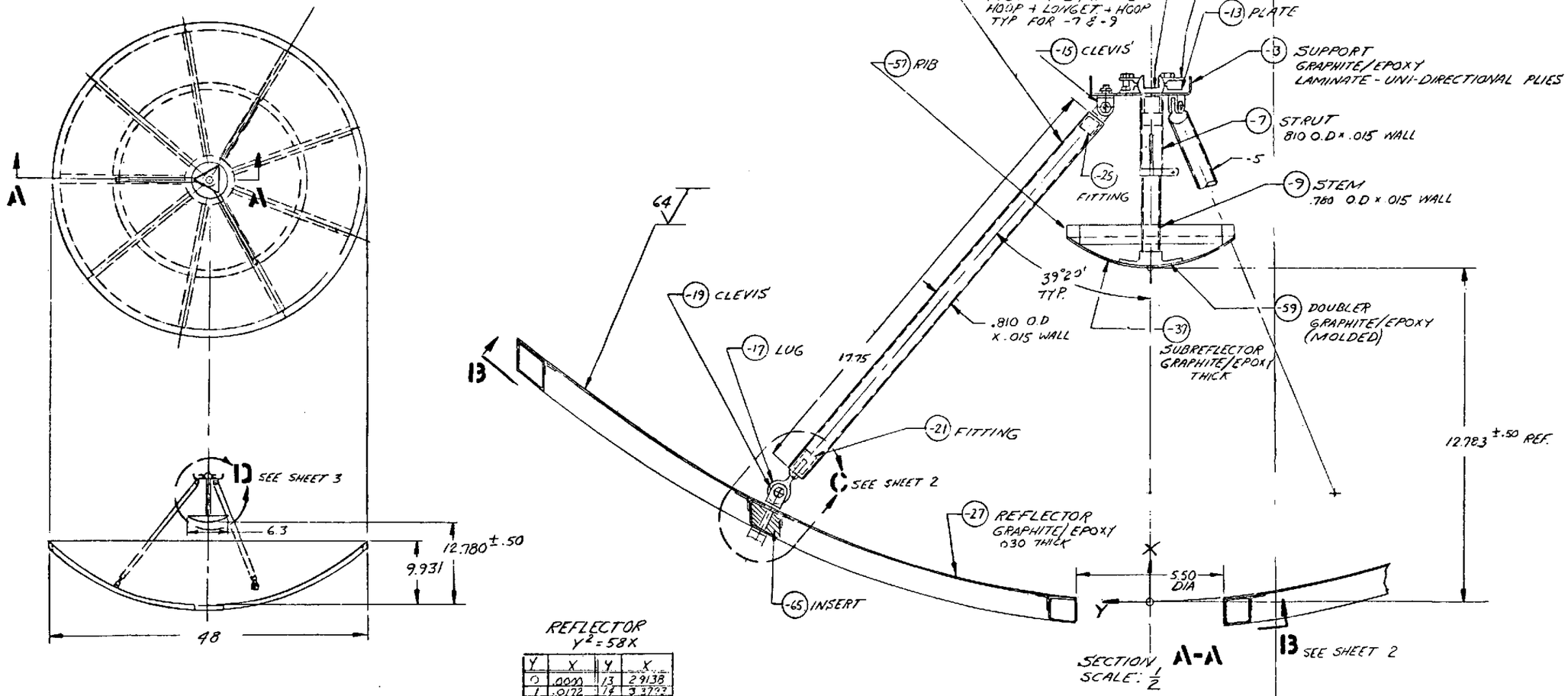

REFLECTOR
$Y^2 = 58X$

Y	X	Y	X
0	.0000	13	2.9138
1	.0172	14	3.3792
2	.0690	15	3.8773
3	.1552	16	4.4082
4	.2759	17	4.9717
5	.4310	18	5.5682
6	.6207	19	6.1974
7	.8449	20	6.8596
8	1.1034	21	7.5547
9	1.3964	22	8.2826
10	1.7241	23	9.0434
11	2.0862	24	9.8370
12	2.4828		

Figure 77. Antenna Details (Sheet 1 of 3)

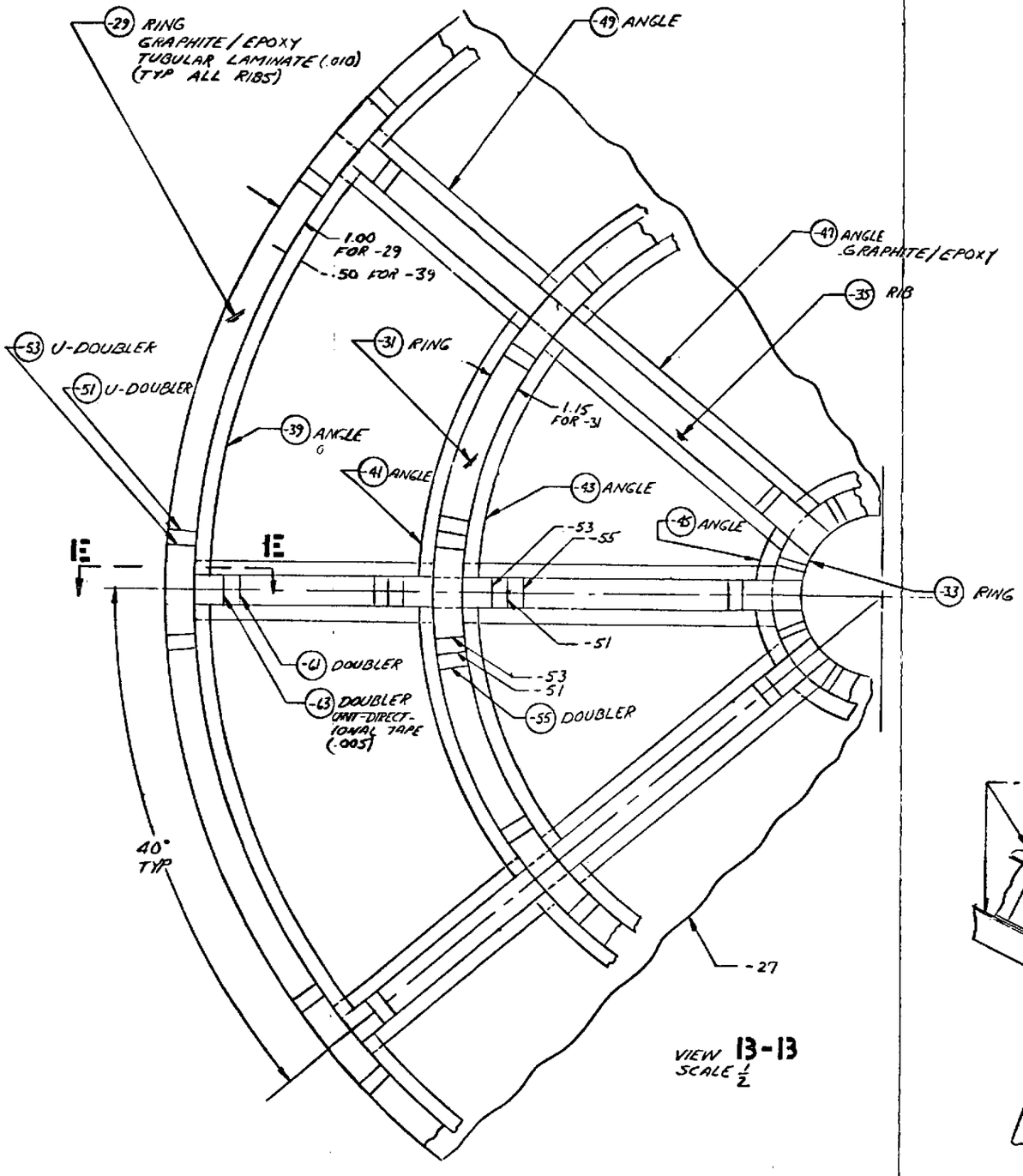

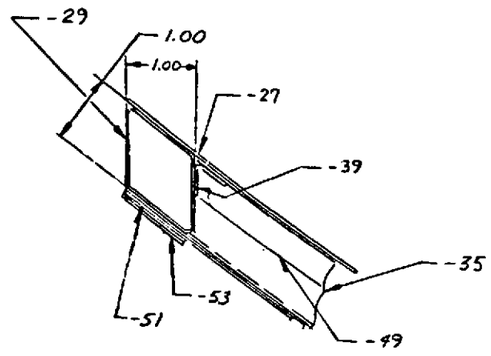

SECTION E-E
SCALE: 1/1

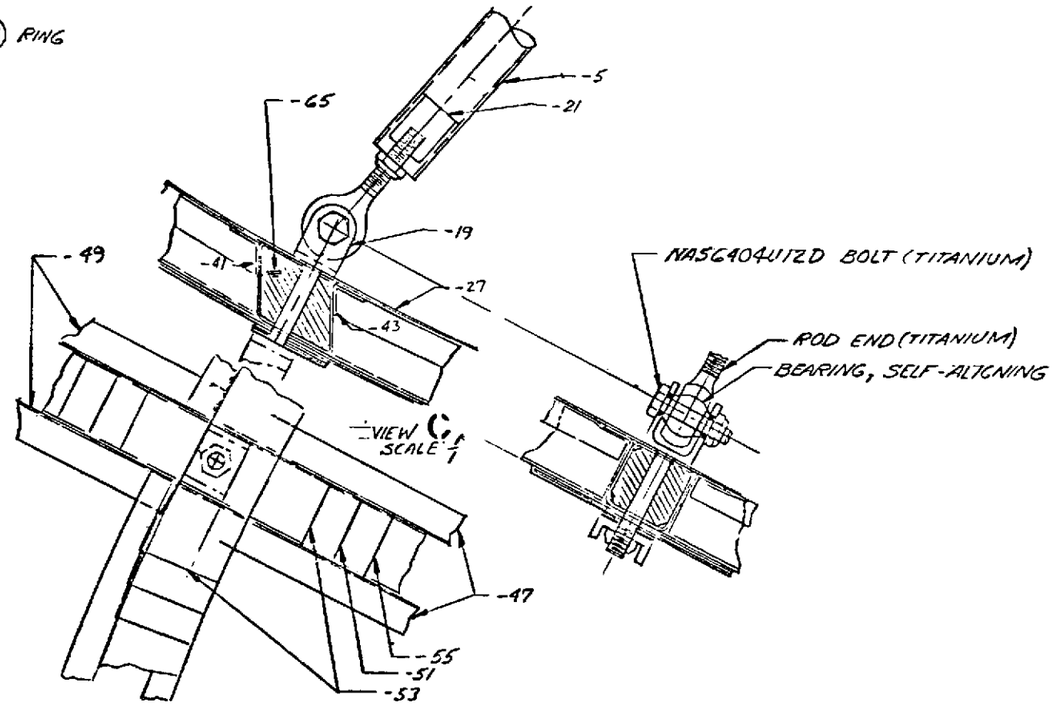

Figure 77. Antenna Details (Sheet 2 of 3)

FOLDOUT FRAME 1

FOLDOUT FRAME 2

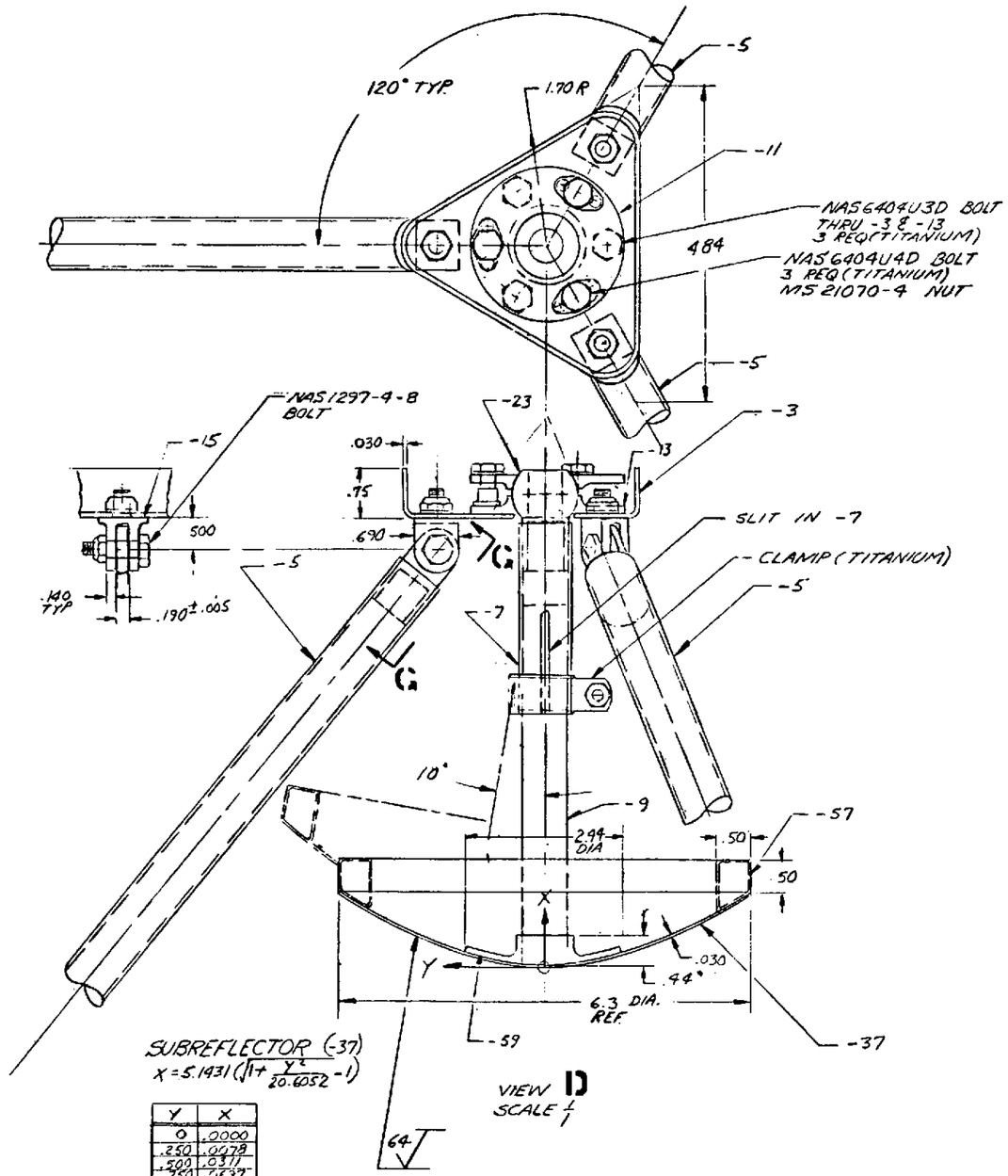

Y	X
0	.0000
.250	.0079
.500	.0311
.750	.0687
1.000	.1203
1.250	.1859
1.500	.2655
1.750	.3590
2.000	.4665
2.250	.5879
2.500	.7232
2.750	.8724
3.000	1.0357
3.150	1.1470

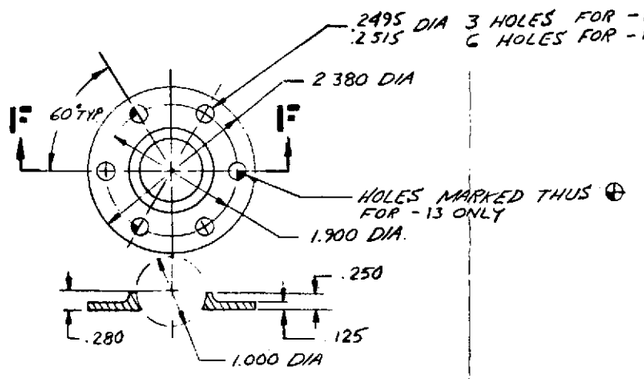

SECTION F-F

DETAIL -11 & -13

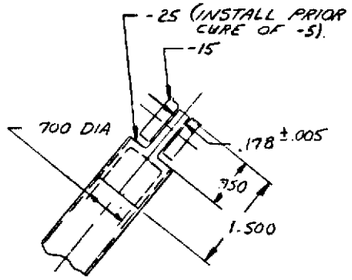

VIEW G-G

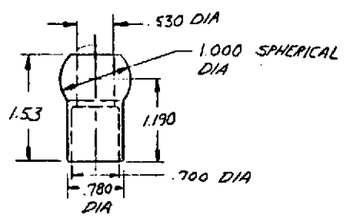

DETAIL -23 FITTING INSTALL PRIOR TO CURE OF -7

Figure 77. Antenna Details (Sheet 3 of 3)

then reinforced with doublers, as shown. Doublers are used at all rib-ring intersections. The doublers in general are continuous prepreg tape with the filaments oriented in the direction of the ring or rib.

Through the spool fits a titanium eye bolt, which threads into a titanium fork fitting, which picks up the ball-and-socket universal joint at the end of one of the tripod struts.

The subreflector is supported by three tubular graphite/epoxy struts set 120 degrees apart. The struts have titanium end fittings. The end fitting attaching to the main reflector is a ball-and-socket universal joint which also allows adjustment of strut length. The end fitting attaching to the subreflector structure is a plain titanium tongue-and-fork joint.

All three struts converge to a graphite/epoxy triangular flanged panel consisting of a balanced six-ply laminate. The attachment to this panel is by means of fork bolts. Oversize holes are provided for adjustment purposes.

The subreflector is made of a graphite/epoxy six-ply balanced laminate, and its rim is stabilized with a tubular ring. The reflector is attached to a graphite/epoxy tubular stem through a graphite/epoxy fitting.

The stem telescopes into a larger-diameter graphite/epoxy tube. This allows distant adjustment of the spacing of subreflector from the main reflector. This tube has a slit cut which allows the tube to be clamped over the inner tube by means of a metal clamp. At the upper end of this tube is a titanium ball joint for adjusting the angular position of the subreflector. The ball joint is attached to the triangular graphite panel through oversize holes for further adjustment of position. A clamping plate is provided to lock the subreflector in the desired angular position.

As can be observed from the above description, sufficient means of adjustment is provided to allow the proper alignment of the subreflector with respect to the main reflector.

Preliminary estimated weight of the complete antenna is about 6.5 pounds with all titanium fittings, and somewhat less if the fittings are fabricated of graphite/epoxy.

2.2.8 Final System Performance

Upon completion of measurements on each component of the antenna subsystem, which had been performed on a near-field range and assembly of the subsystem, the complete antenna assembly was then tested on a far-field range. A 988-foot range distance was established, which is more than twice the usual for field requirement ($2D^2/\lambda$) of 480 feet at the shortest wavelength of interest. The antenna was centered at a height of 16.2 feet on a fixture capable of providing axial over azimuth rotation. Range geometry was aligned within approximately 2 minutes of arc in both planes, using optical techniques. The illumination field was then probed over the dimensions of the antenna apertures, and the range was determined to be free of reflections to approximately -60 db.

The antenna subsystem was assembled and aligned as close as possible, using optical methods, to the geometry determined in Section 2.2.3. The linearly polarized patterns obtained with this condition of adjustment were excellent, as shown in Figure 78. This pattern of the transmit channel, typical of those taken in four planes (0°, 90°, ±45°) at 14.650 GHz, shows the highest side lobe to be 24 db down, with remaining lobes falling off rapidly. No sidelobes higher than -40 db were found in the forward hemisphere beyond 36 degrees from boresight, and the highest cross-polarized level is -33 db. The half-power beamwidth is 70 minutes of arc (1.17 degrees), indicating an aperture efficiency of 84.22 percent. Gain was measured to be 43.21 db, yielding an overall efficiency of 59.84 percent.

The electrical axis of the antenna was found to be approximately 1/4 degree off the mechanical axis to which the range had been aligned. With the two-axis positioner as described above, the beam could not be centered on the range except at one discrete roll angle. An axial over elevation over azimuth positioner would have overcome this difficulty, since precise electrical and mechanical axis alignment is not required, but the time required for

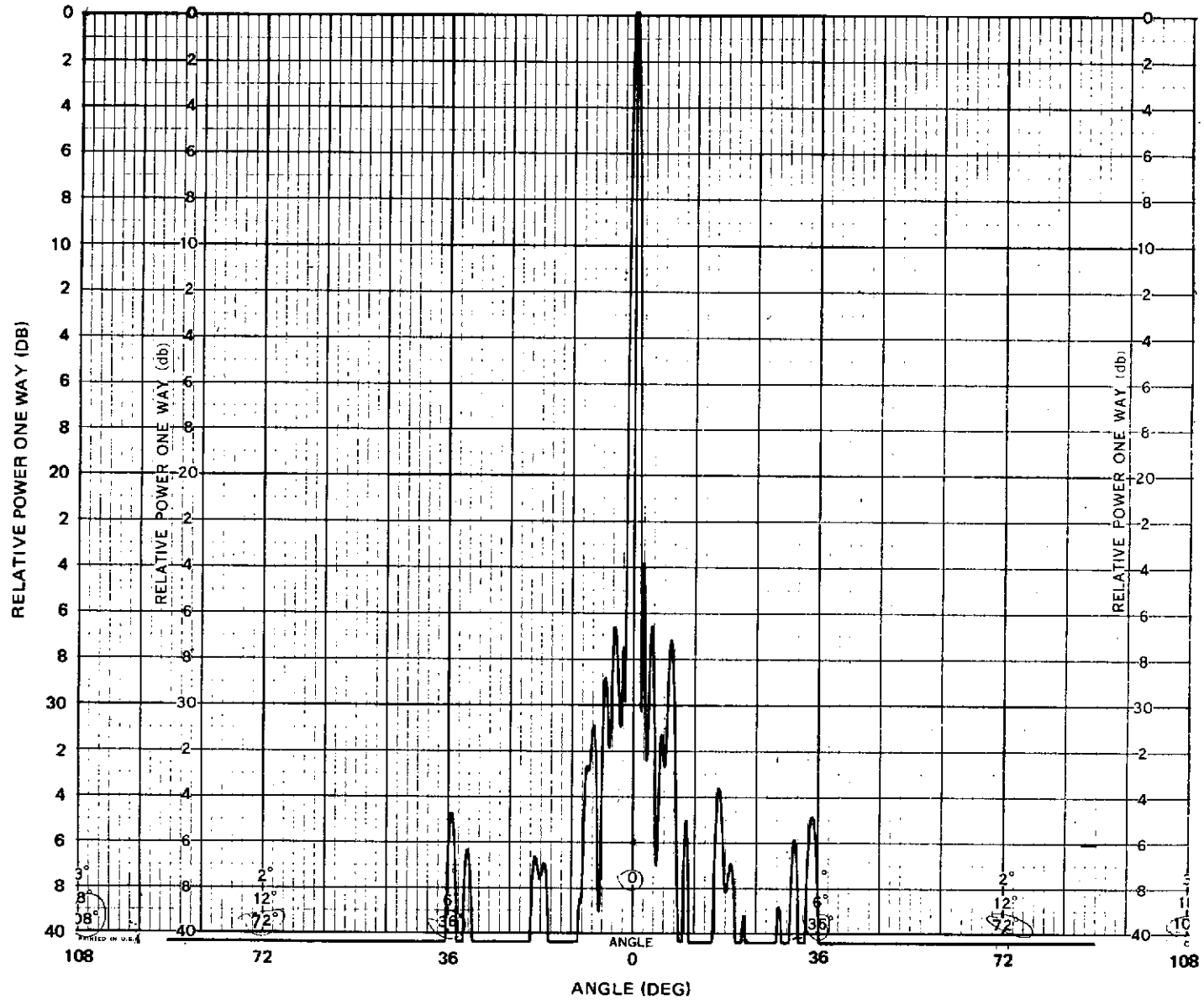

Figure 78. Subsystem Pattern — Initial Alignment

reconstruction and realignment of the range did not appear justified. The antenna subsystem was therefore realigned to make the two axes coincident.

The results obtained after realignment of the antenna were not as good as those obtained previously. The adjustment was carried out by tilting the reflector to bring the beam to coincidence with the range axis, then adjusting feed network and subreflector for maximum gain. The gain and efficiency data for the linearly polarized subsystem, as finally aligned, is provided in Table 7. The gain degradation incurred by realignment is nearly 0.4 db at 14.650 GHz, yielding a value of 54.70 percent efficiency. The values for the receive channel at 13.600 GHz are considerably better, 42.65 db and 61.09 percent efficiency. Also shown in Table 7 are gain and efficiency values adjusted to eliminate the losses due to VSWR of the final assembly which are shown in Table 8. This represents the gain which would be achieved if the ports were perfectly matched, a condition which could be approached with slight additional effort on the feed. The final alignment condition is obviously not optimum, but the contractual delivery schedule did not allow further effort. The achievable efficiency of this configuration, however, is at least greater than 62 percent and likely to be somewhat higher.

Effects of alignment can also be seen in the final patterns, Figures 79 through 88. The first sidelobe is higher than the original configuration by typically 6 db, while other near-in lobes were decreased substantially. The average cross-polarization level increased slightly to approximately 30 db. Rotational symmetry of the patterns was maintained to a high degree, as will be seen in the pattern beamwidth summary of Table 9.

The merits of the add-on polarizer approach are demonstrated in the circularly polarized patterns and gain measurements. The circular patterns, Figures 89 through 98, did not change appreciably from the linear configuration, and rotational symmetry was actually improved due to an apparent diffusing effect of the polarizer. Sidelobe levels increased to an average -16 db, an increase of 2 db from the linear, due primarily to the increased blockage ratio of the polarizer as discussed in Section 2.2.3. It was earlier pointed out that the polarizer slightly increased the beamwidth of the feedhorn.

Table 7

GAIN AND EFFICIENCY RESULTS

	Port 2 14.650 GHz		Port 1 13.600 GHz
	Original Alignment	Final Alignment	Final Alignment
Maximum Gain $\frac{4\pi A}{\lambda^2}$ (db)	45.44	45.44	44.79
Measured Gain (db)	43.21	42.82	42.65
Efficiency (%)	59.84	54.70	61.09
VSWR Loss (db)	0.18	0.18	0.01
Available Gain (if matched) (db)	43.39	43.00	42.66
Available Efficiency (if matched) (%)	62.37	57.02	61.24

Table 8

VSWR OF ANTENNA SUBSYSTEM

	Frequency	VSWR		Frequency	VSWR
	13.500	1.45		14.550	2.20
Port 1	13.600	1.10	Port 2	14.650	1.50
	13.700	1.30		14.750	1.50

The effect of such broadening is to provide less taper across the aperture of the reflector, resulting in a somewhat narrower subsystem beamwidth and slightly higher sidelobes. Table 9 provides a summary of the measured beamwidths of both the linear and circular configurations, and shows the circularly polarized beamwidth reduction to be only 1-1/2 percent. The increased sidelobe level due to the variation in aperture distribution can be assumed to be similarly negligible. The measured cross-polarization level increased significantly to approximately -23 db. Since ellipticity of the transmitter was maintained to 0.25 db maximum, -30 db is the minimum cross-polarization level which could be measured even with a perfectly circular antenna, so that

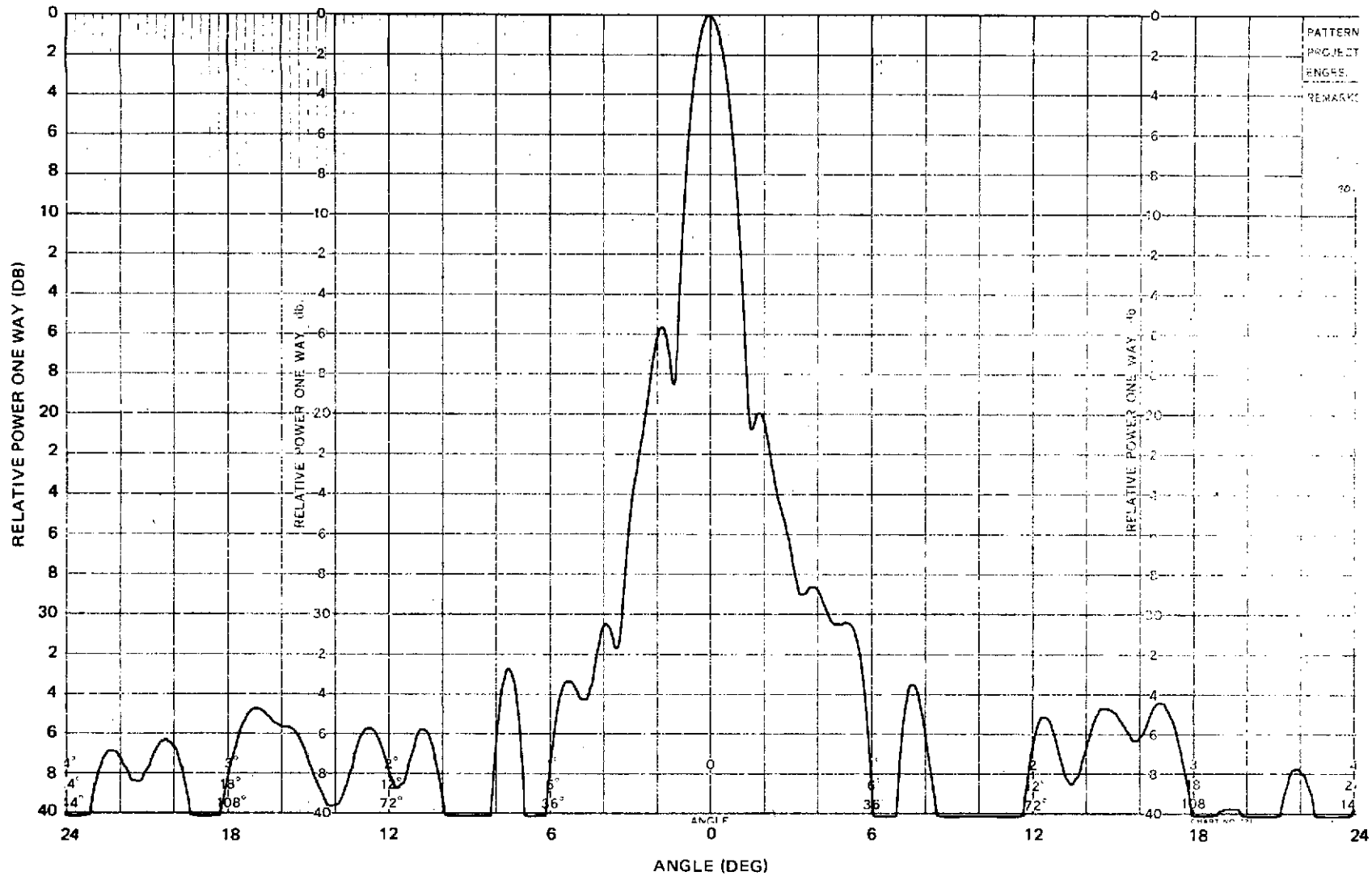

Figure 79. Port 2 E-Plane Pattern ~ Linear Polarization 14.650 GHz $\phi = 0^{o}$

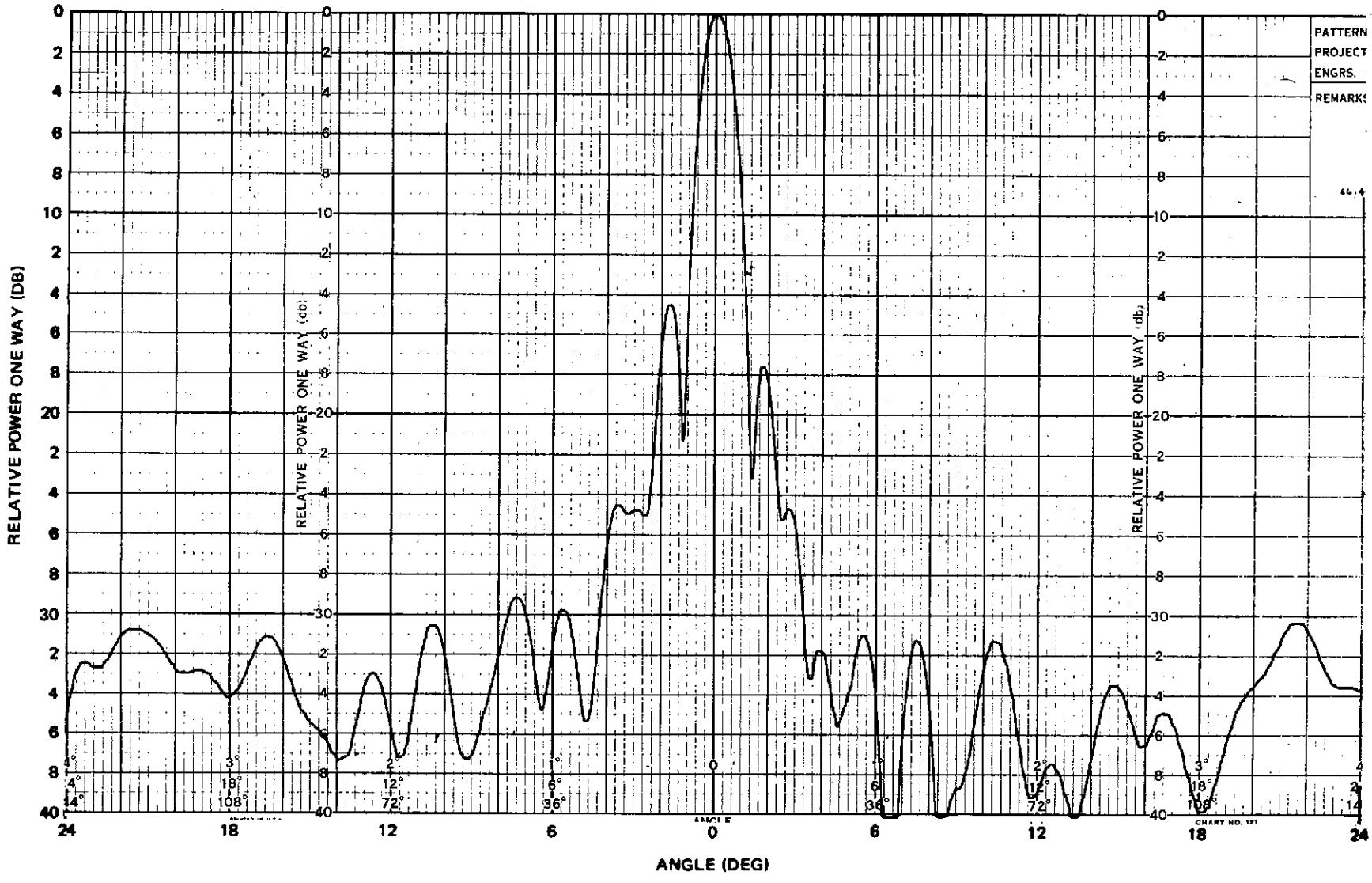

Figure 80. Port 2 H-Plane Pattern ~ Linear Polarization 14.650 GHz $\phi = 90^{o}$

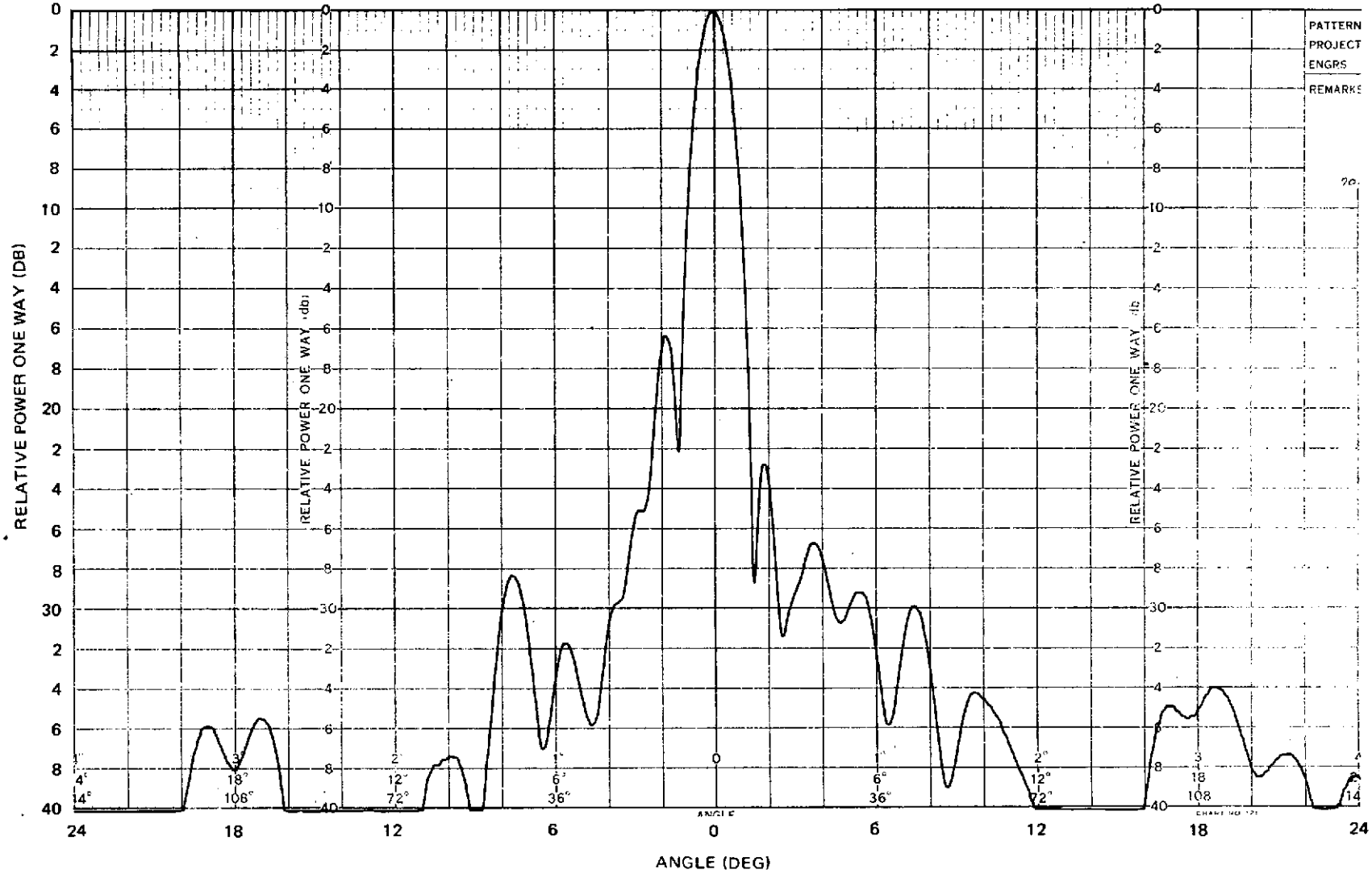

Figure 81. Port 2 E-Plane Pattern ~ Linear Polarization 14.550 GHz $\phi = 0^{o}$

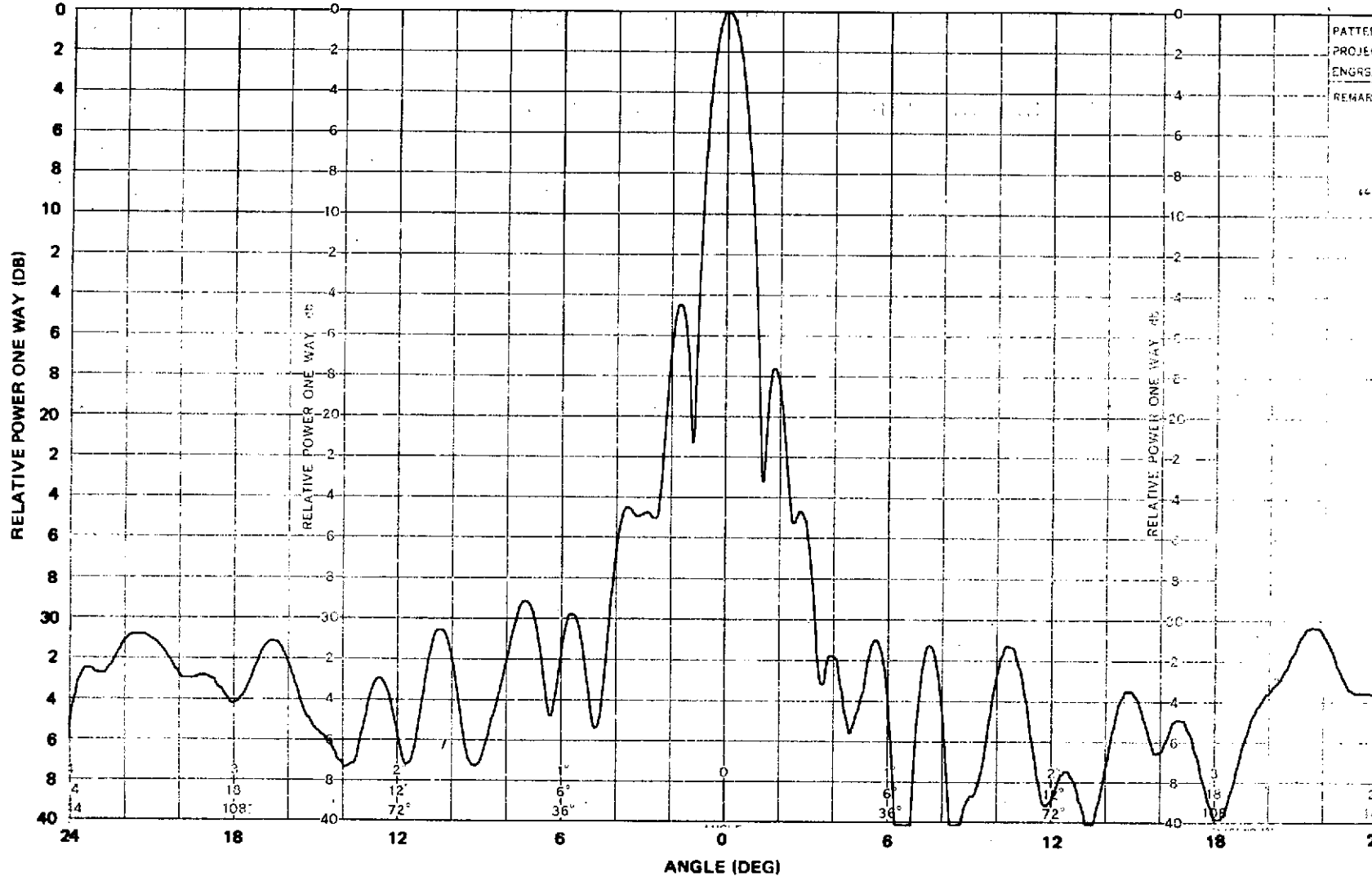

Figure 82. Port 2 E-Plane Pattern ~ Linear Polarization 14.750 GHz $\phi = 0^{o}$

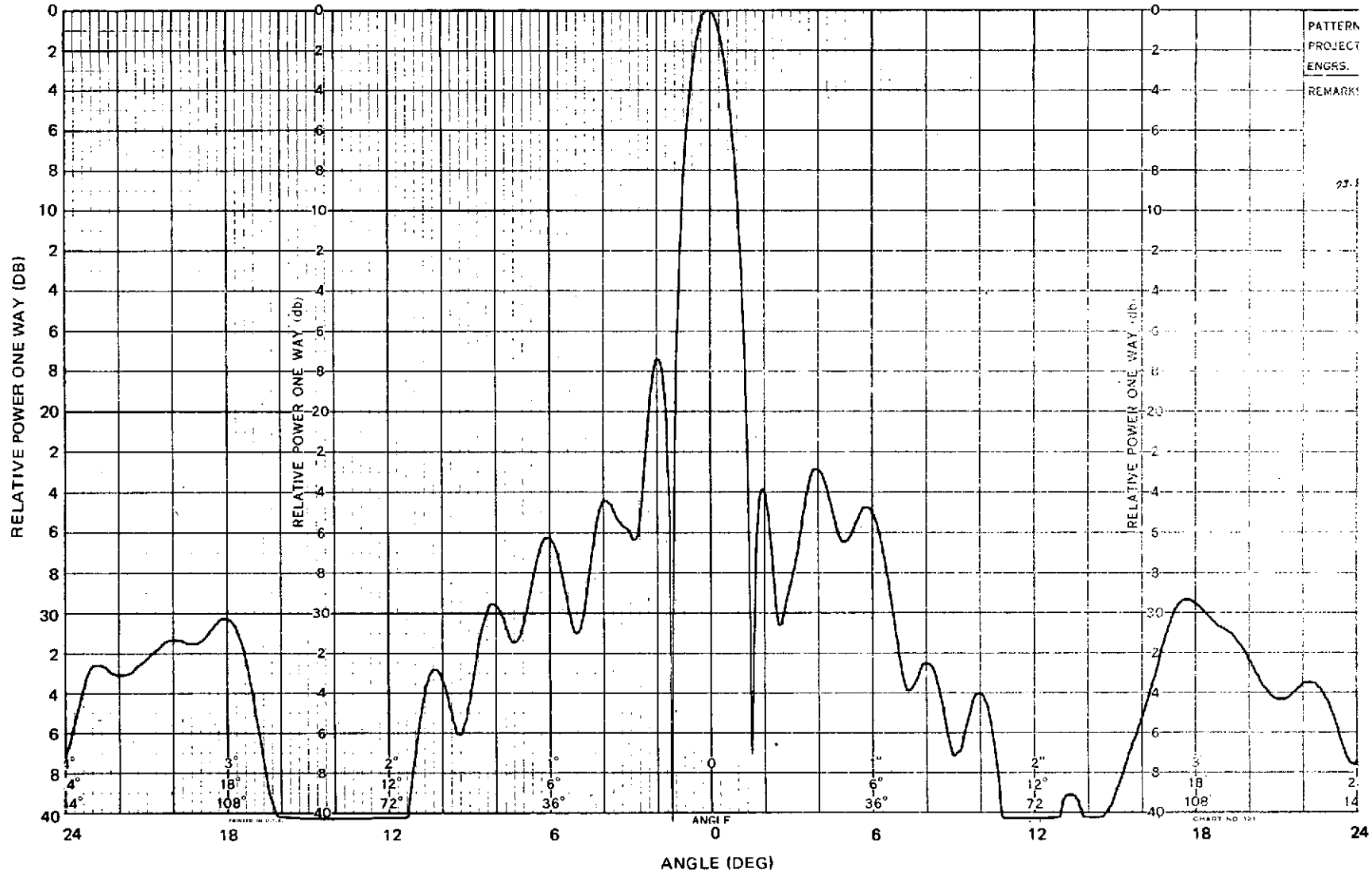

Figure 83. Port 1 H-Plane Pattern ~ Linear Polarization 13.600 GHz $\phi = 0^{o}$

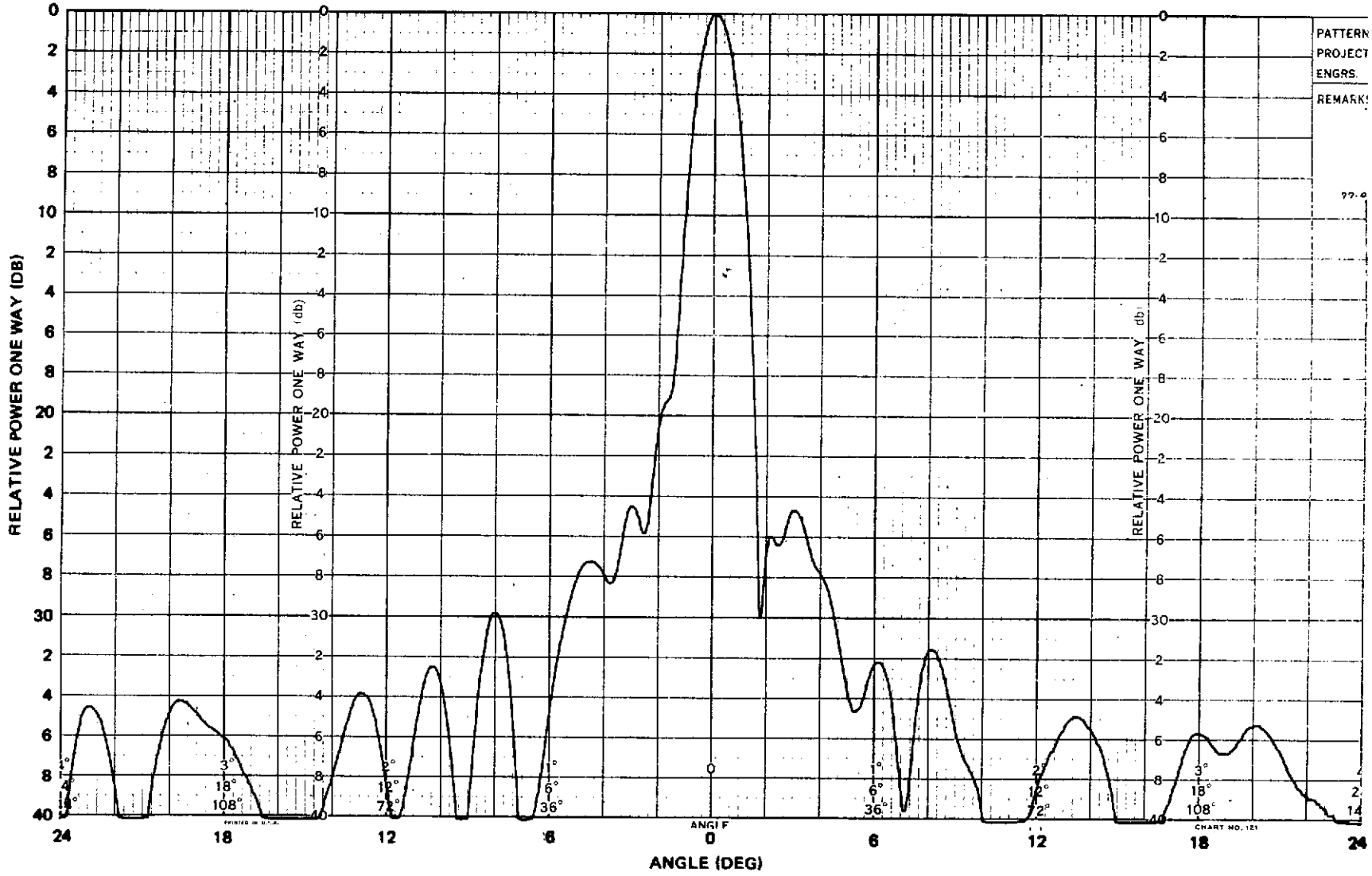

Figure 84. Port 1 E-Plane Pattern ~ Linear Polarization 13.600 GHz $\phi = 90^{o}$

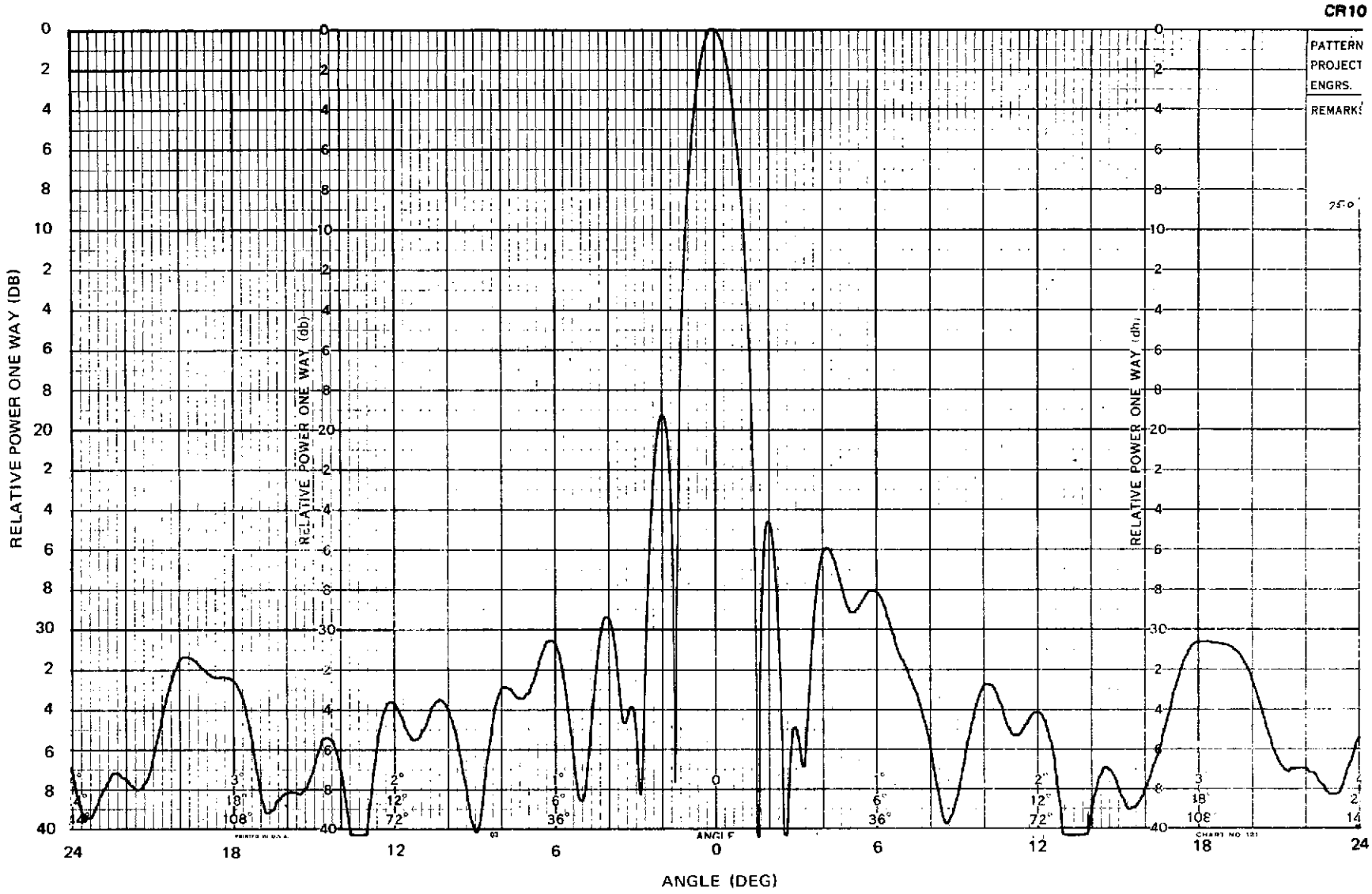

Figure 85. Port 1 H-Plane Pattern ~ Linear Polarization 13.500 GHz $\phi = 0^{o}$

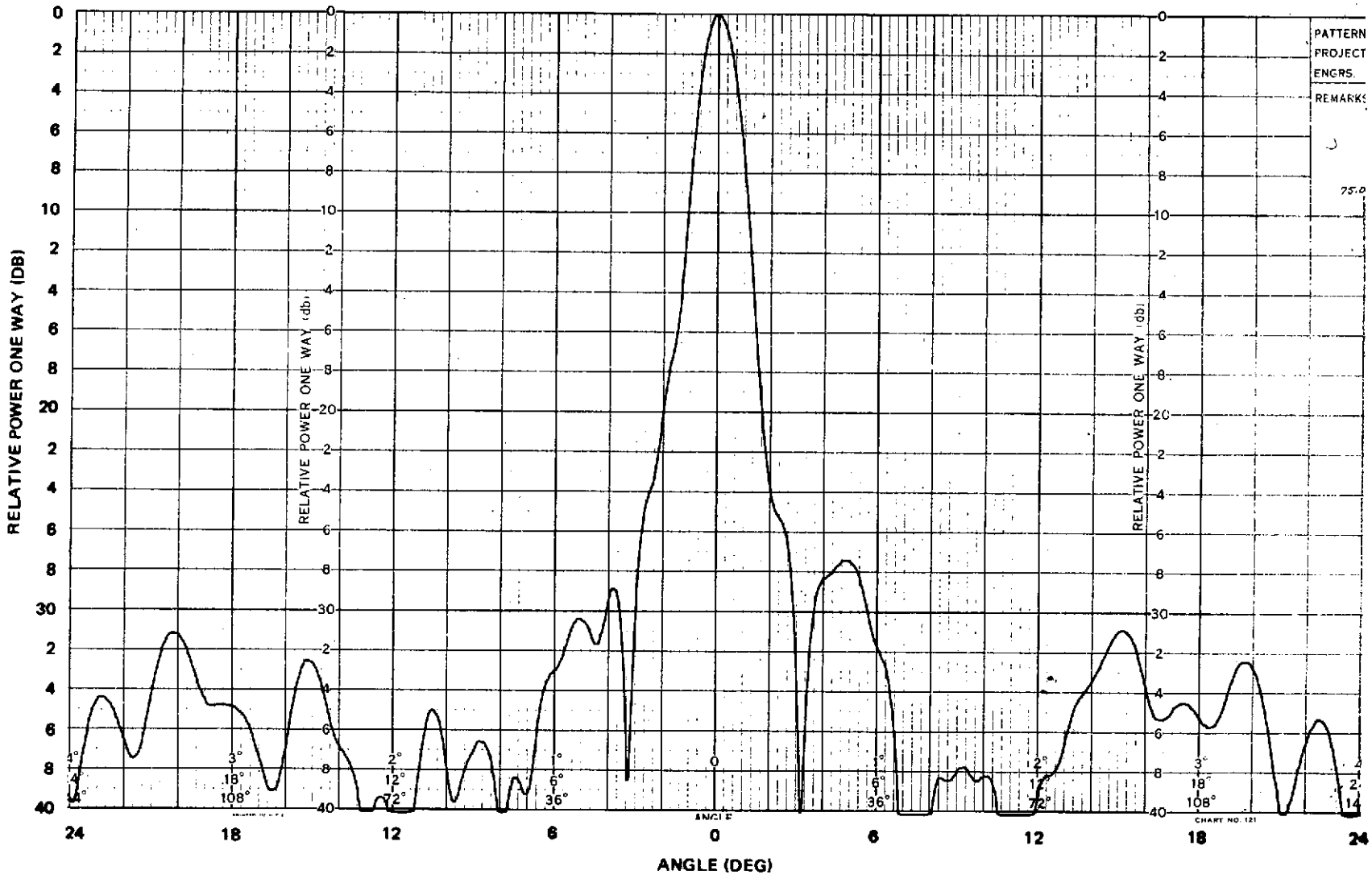

Figure 86. Port 1 H-Plane Pattern ~ Linear Polarization 13.700 GHz $\phi = 0^{o}$

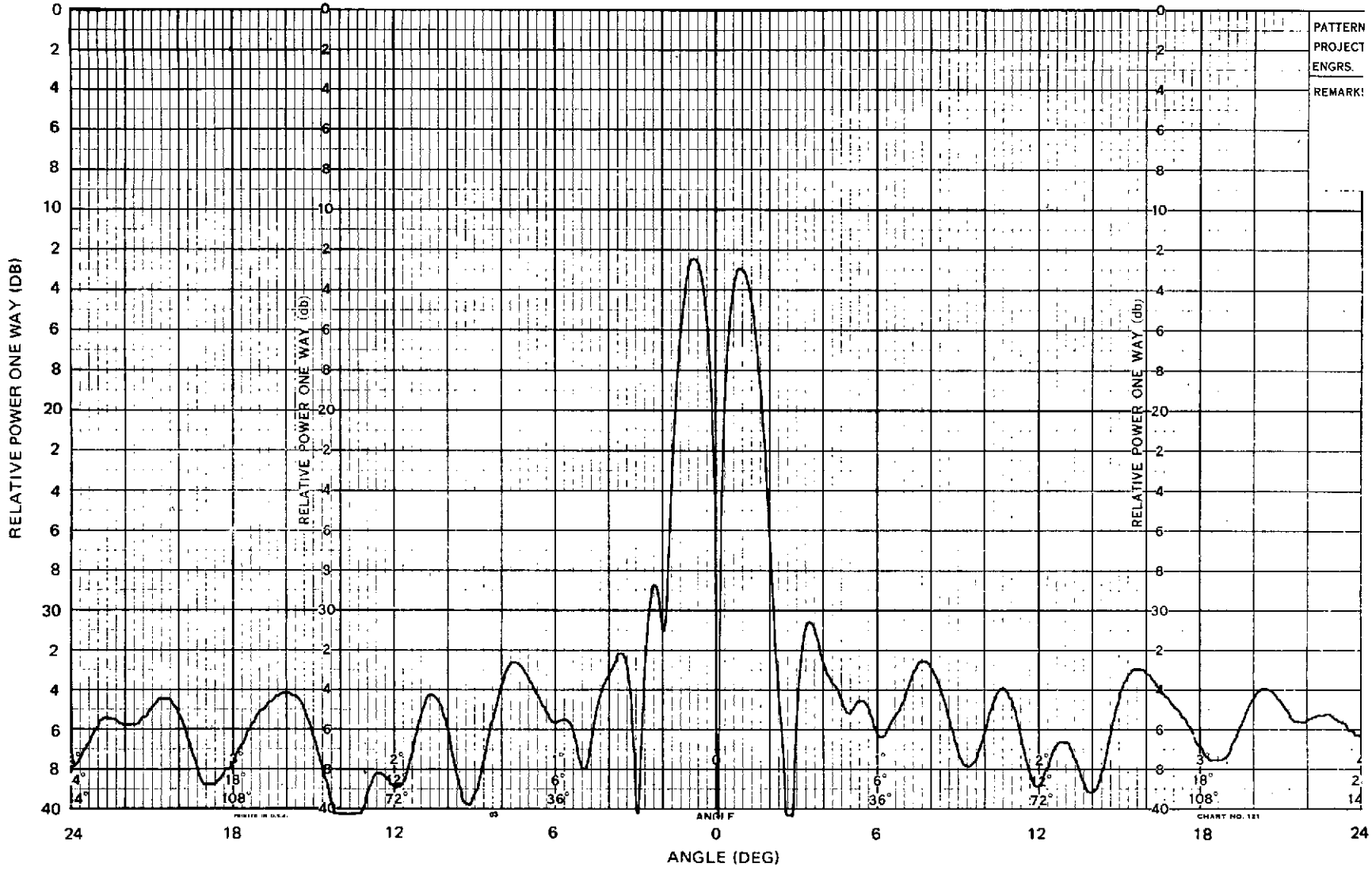

Figure 87. Port 4 Azimuth Difference Pattern ~ Linear Polarization 13.600 GHz $\phi = 0^{o}$

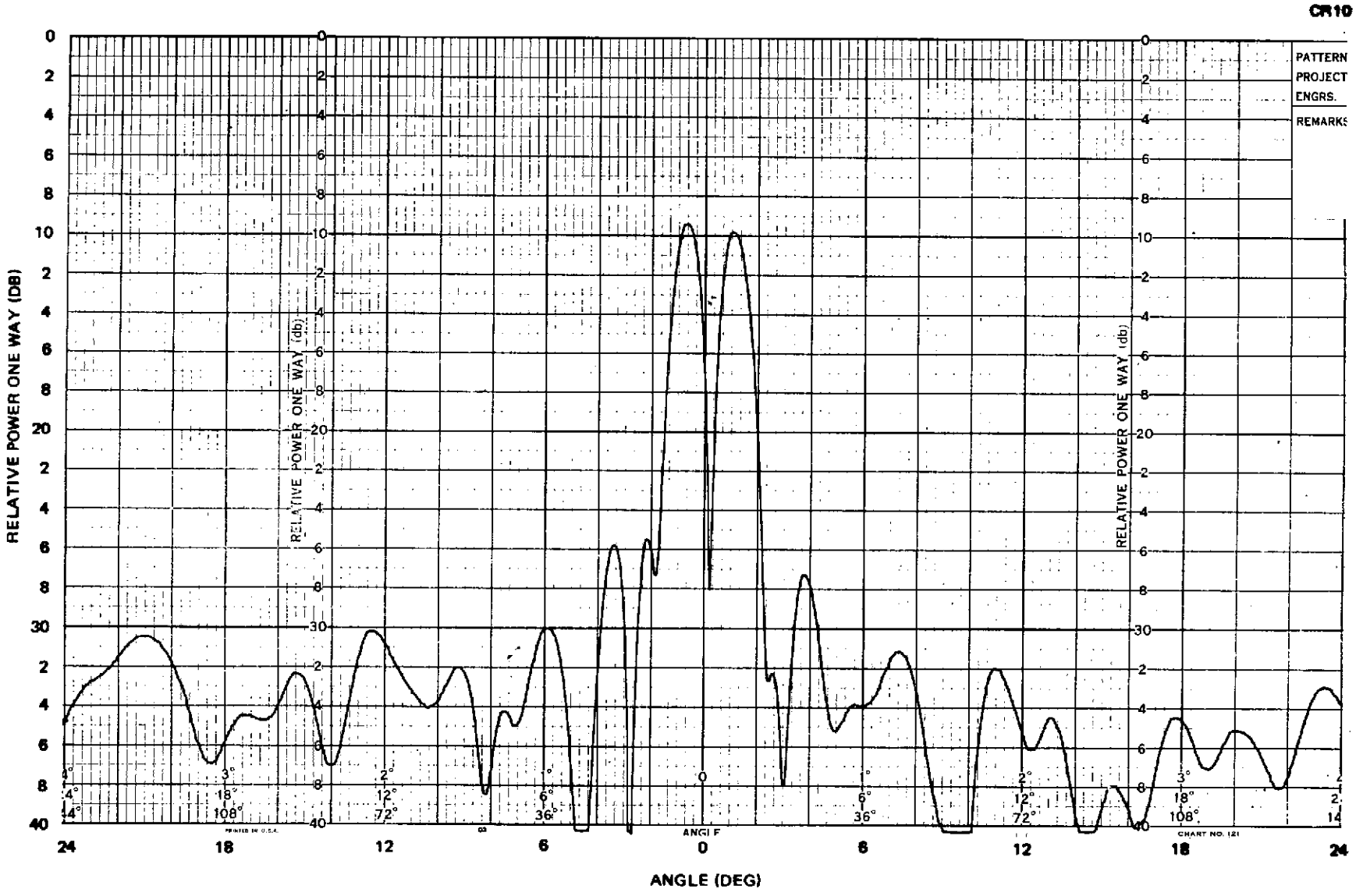

Figure 88. Port 3 Elevation Difference Pattern ~ Linear Polarization 13.600 GHz $\phi = 90^{o}$

Table 9

FINAL MEASURED BEAMWIDTHS

LINEAR POLARIZATION

	Freq (GHz)	E-Plane (arc min)	H-Plane (arc min)	ϕ = 45 (arc min)	ϕ = 315 (arc min)	Avg (arc min)
Port 1	13.500	75.0	75.0			75.0
	13.600	77.0	73.8	75.0	75.0	75.2
	13.700	77.0	70.5			73.75
Port 2	14.550	70.7	70.5			70.16
	14.650	70.4	66.4	72.0	71.2	70.0
	14.750	75.0	63.8			69.4

CIRCULAR POLARIZATION

	Freq (GHz)	(E) (arc min)	(H) (arc min)	45 (arc min)	315 (arc min)	Avg (arc min)	Circ./Lin.	Pol. Beam Narrowing (%)
Port 1 RHCP	13.500	75.0	73.5			74.25	0.99	1
	13.600	75.0	73.1	72.4	75.0	73.9	0.983	1.7
	13.700	73.1	71.2			72.15	0.979	2.1
Port 2 LHCP	14.550	71.3	69.4			70.35	0.995	0.5
	14.650	69.4	67.5	68.6	69.4	68.7	0.982	1.8
	14.750	72.7	63.8			68.25	0.984	1.6
	Avg Beam Narrowing Due to Polarizer						0.9855	1.45

the increase in cross-polarization level can be attributed almost entirely to the measurement process. Measured gain decreased 0.25 db and 0.40 db on the receive and transmit channels, respectively. In Table 2, it was seen that the polarizer decreases blockage efficiency by 4.8 percent, or 0.21 db. This leaves only 0.04 and 0.19 db in receive and transmit channels, respectively, to be attributed to polarizer network insertion loss, pattern effects, and

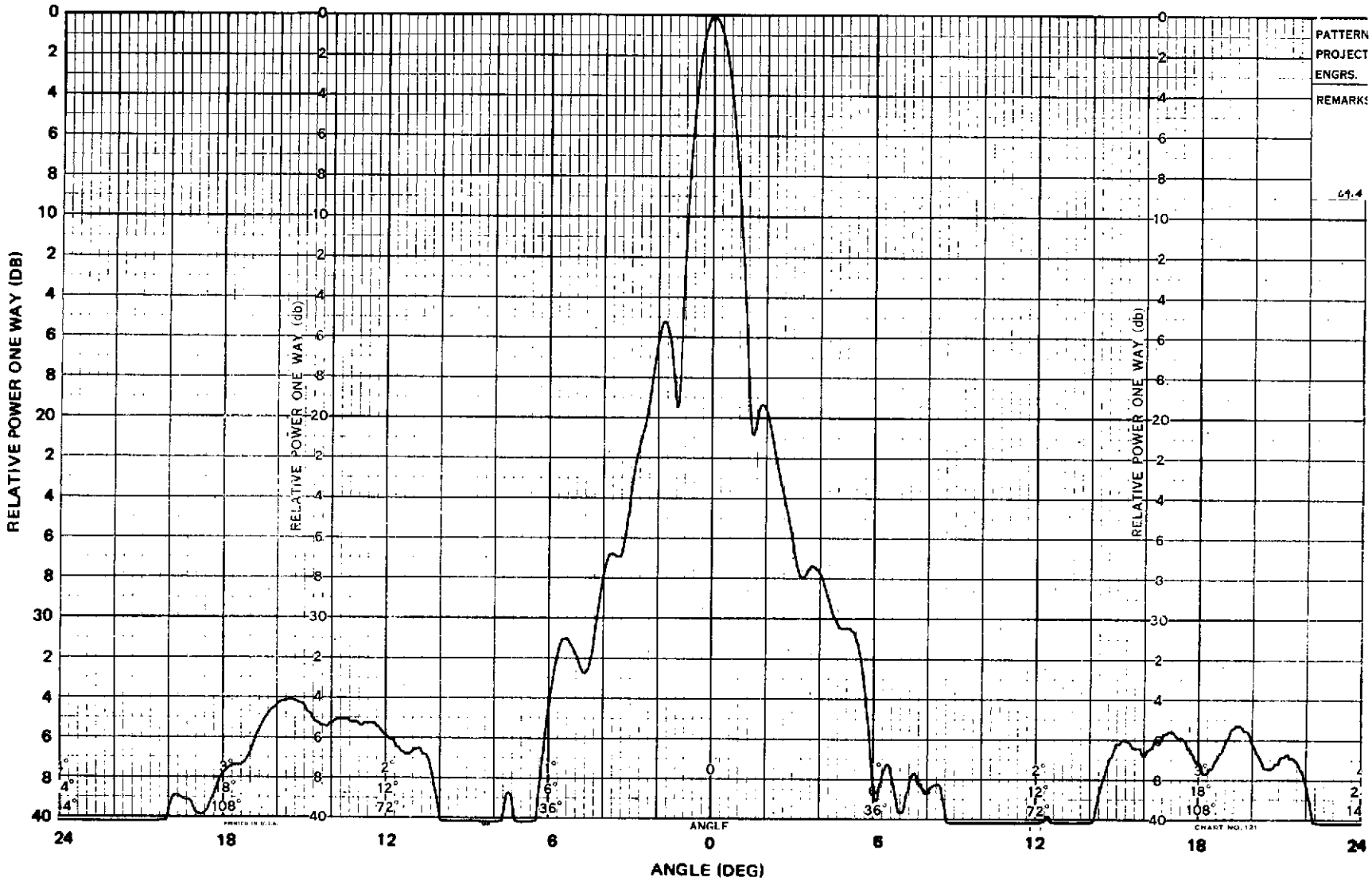

Figure 89. Port 2 E-Plane Pattern ~ Circular Polarization 14.650 GHz $\phi = 0^{o}$

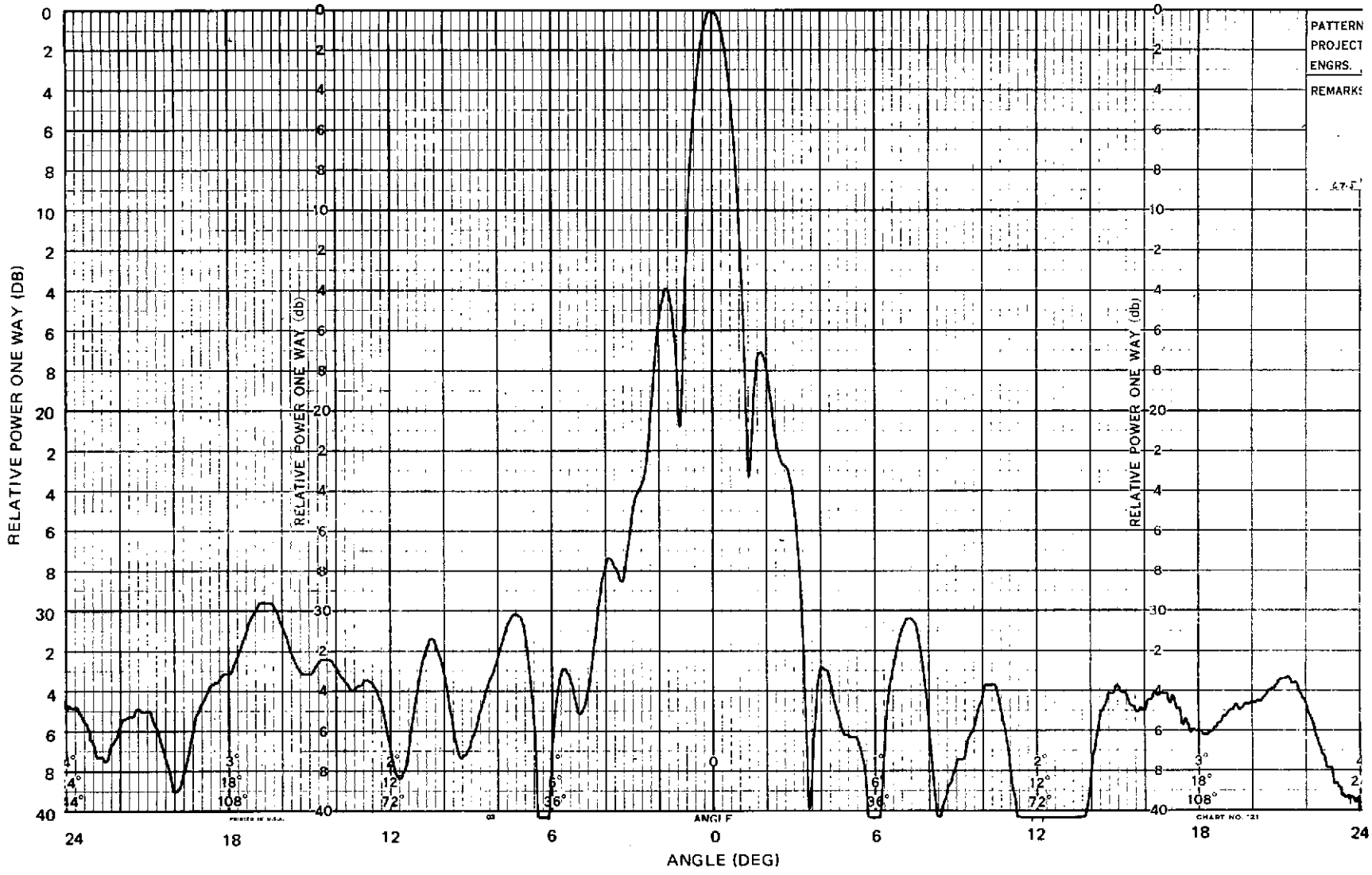

Figure 90. Port 2 H-Plane Pattern ~ Circular Polarization 14.650 GHz $\phi = 90^{o}$

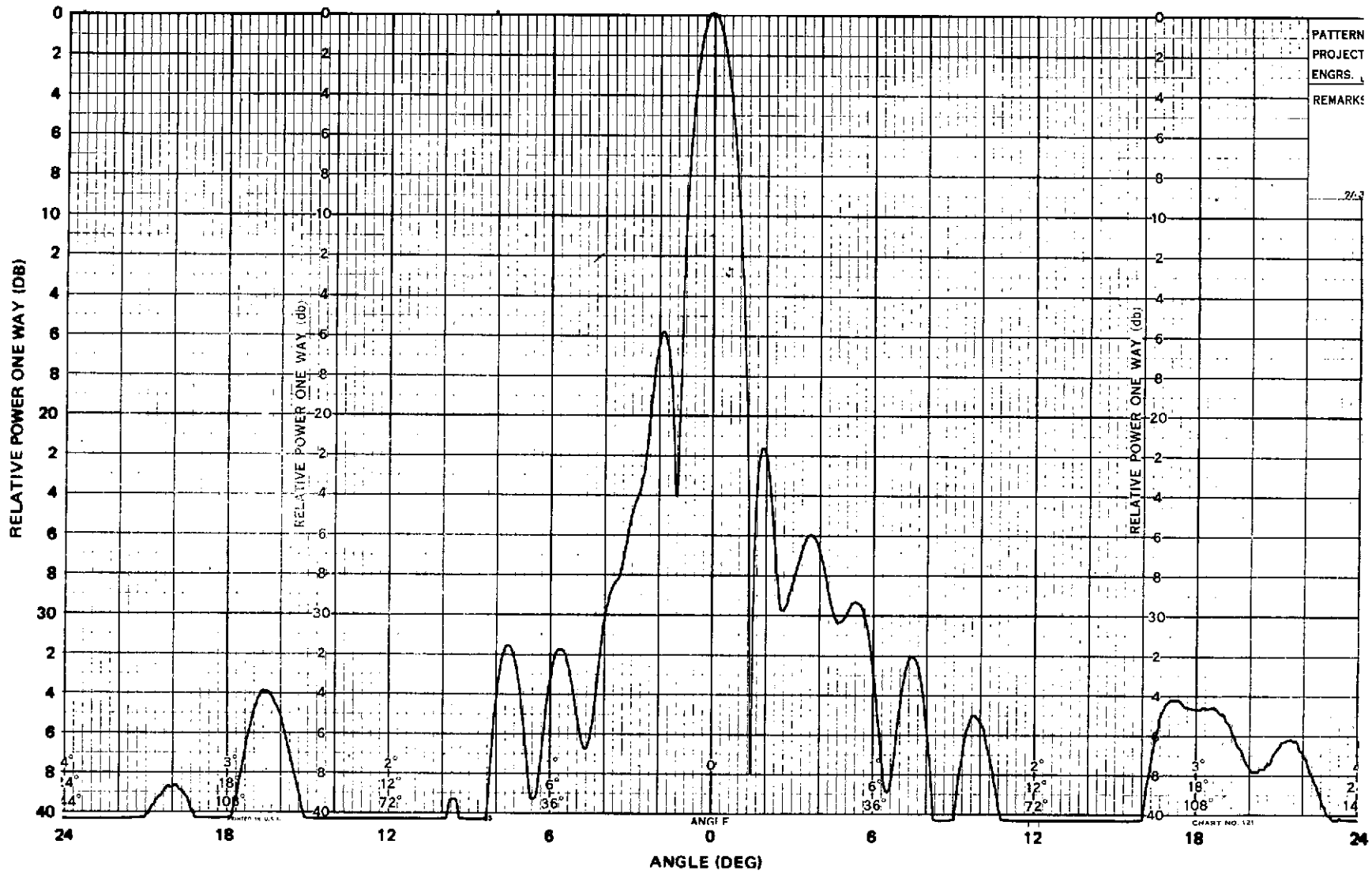

Figure 91. Port 2 E-Plane Pattern ~ Circular Polarization 14.550 GHz $\phi = 0^{o}$

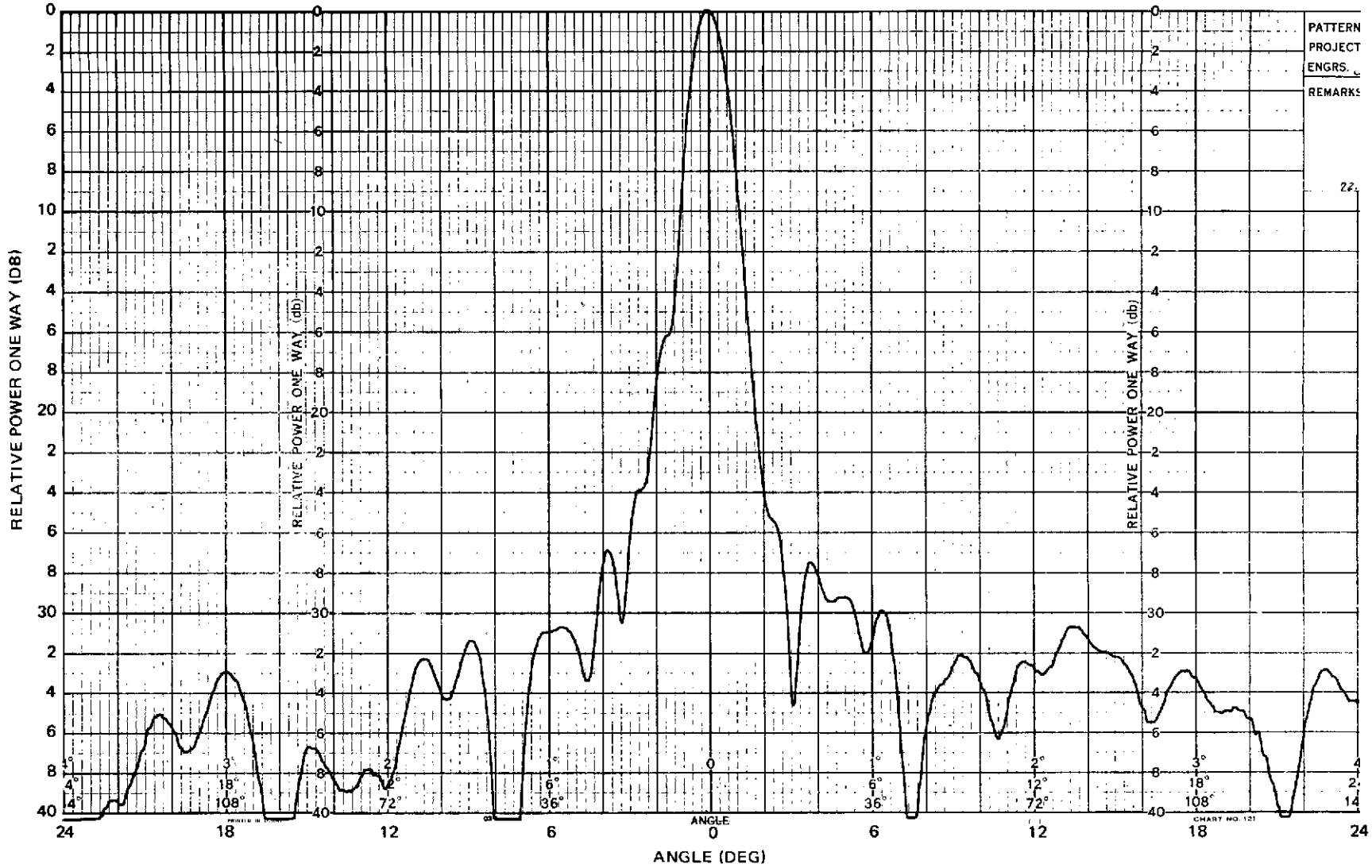

Figure 92. Port 2 E-Plane Pattern ~ Circular Polarization 14.750 GHz $\phi = 0^{o}$

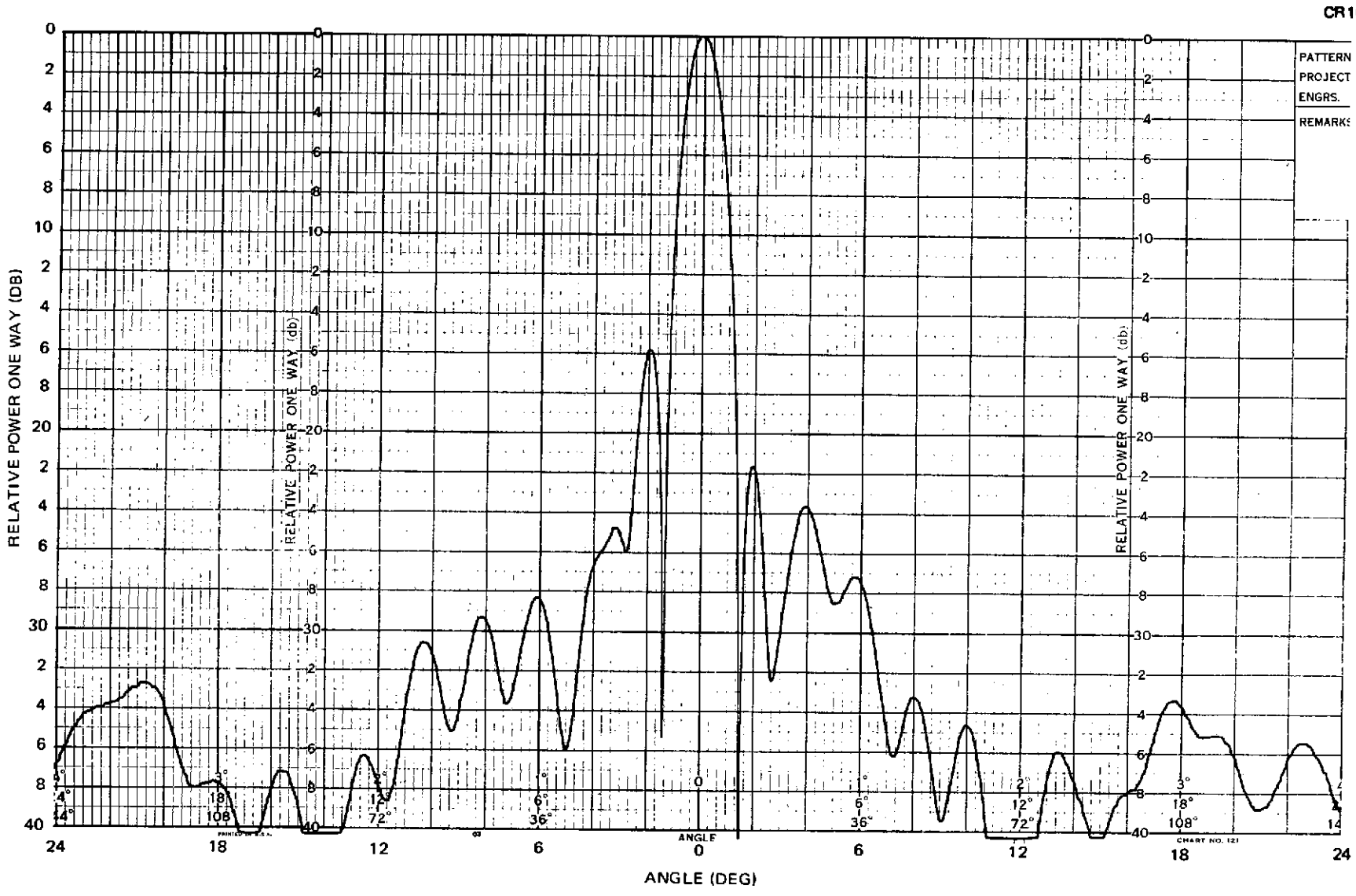

Figure 93. Port 1 H-Plane Pattern ~ Circular Polarization 13.600 GHz $\phi = 0^{o}$

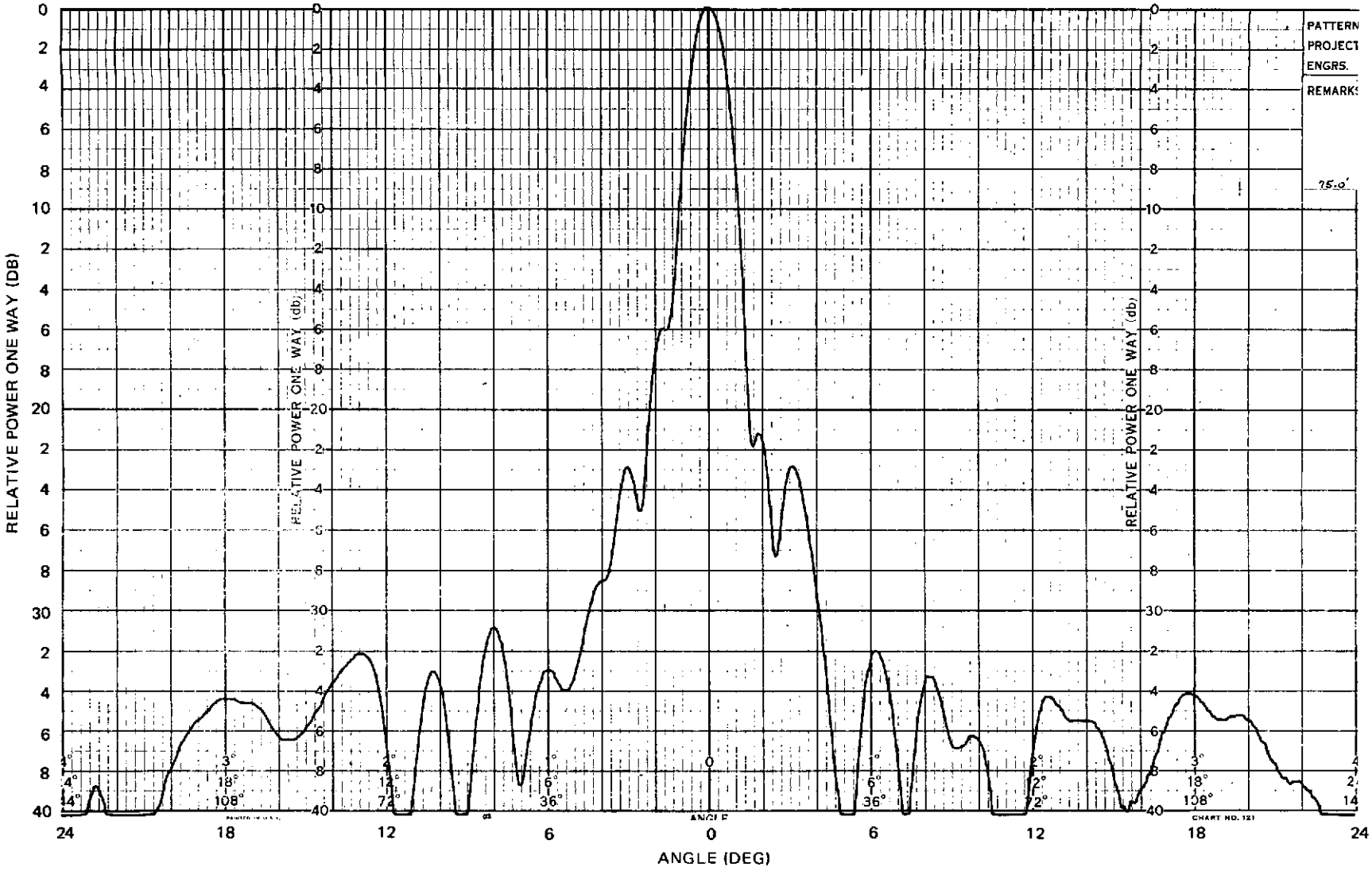

Figure 94. Port 1 E-Plane Pattern ~ Circular Polarization 13.600 GHz $\phi = 90^{o}$

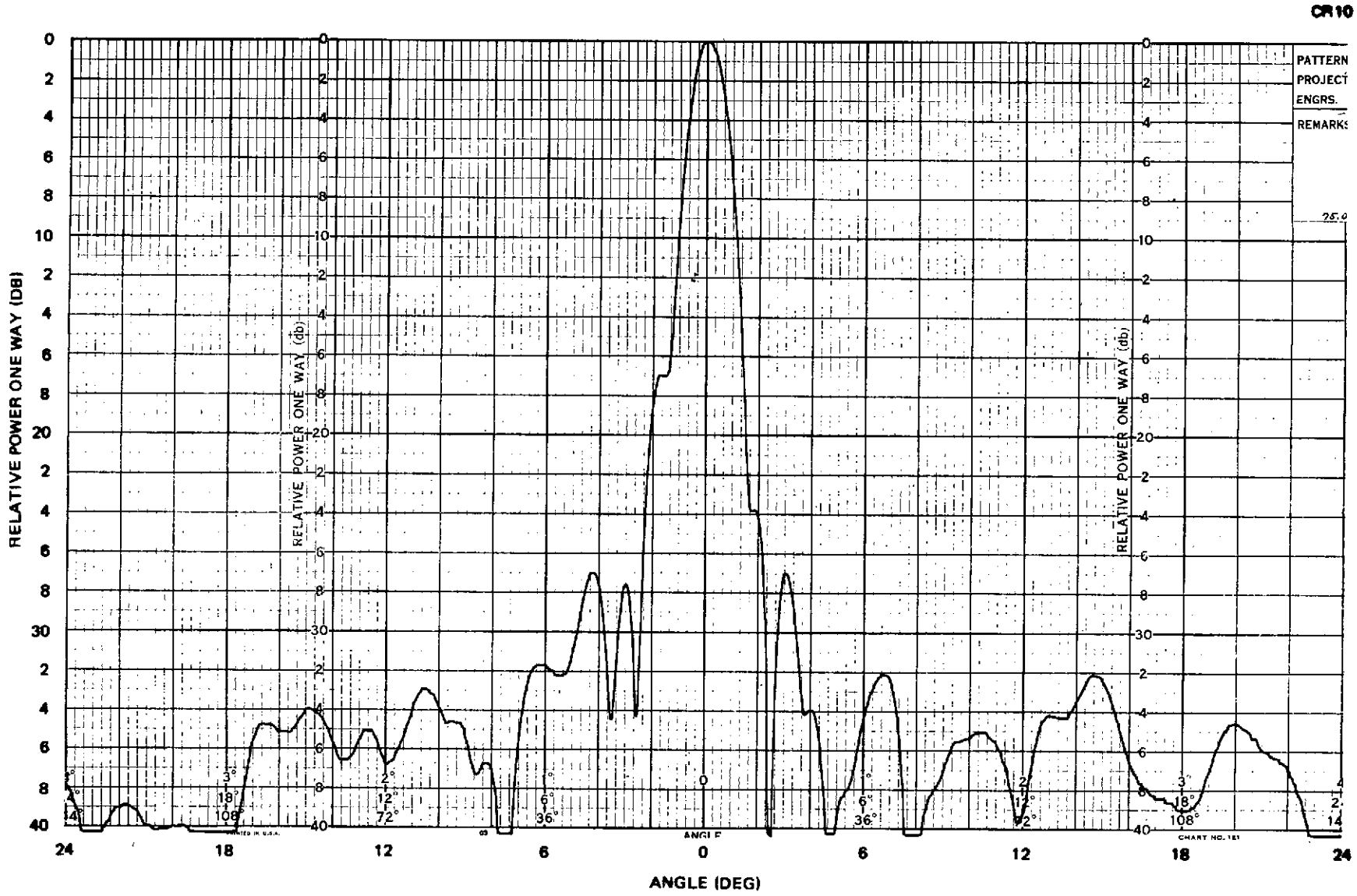

Figure 95. Port 1 E-Plane Pattern ~ Circular Polarization 13.500 GHz $\phi = 90^{o}$

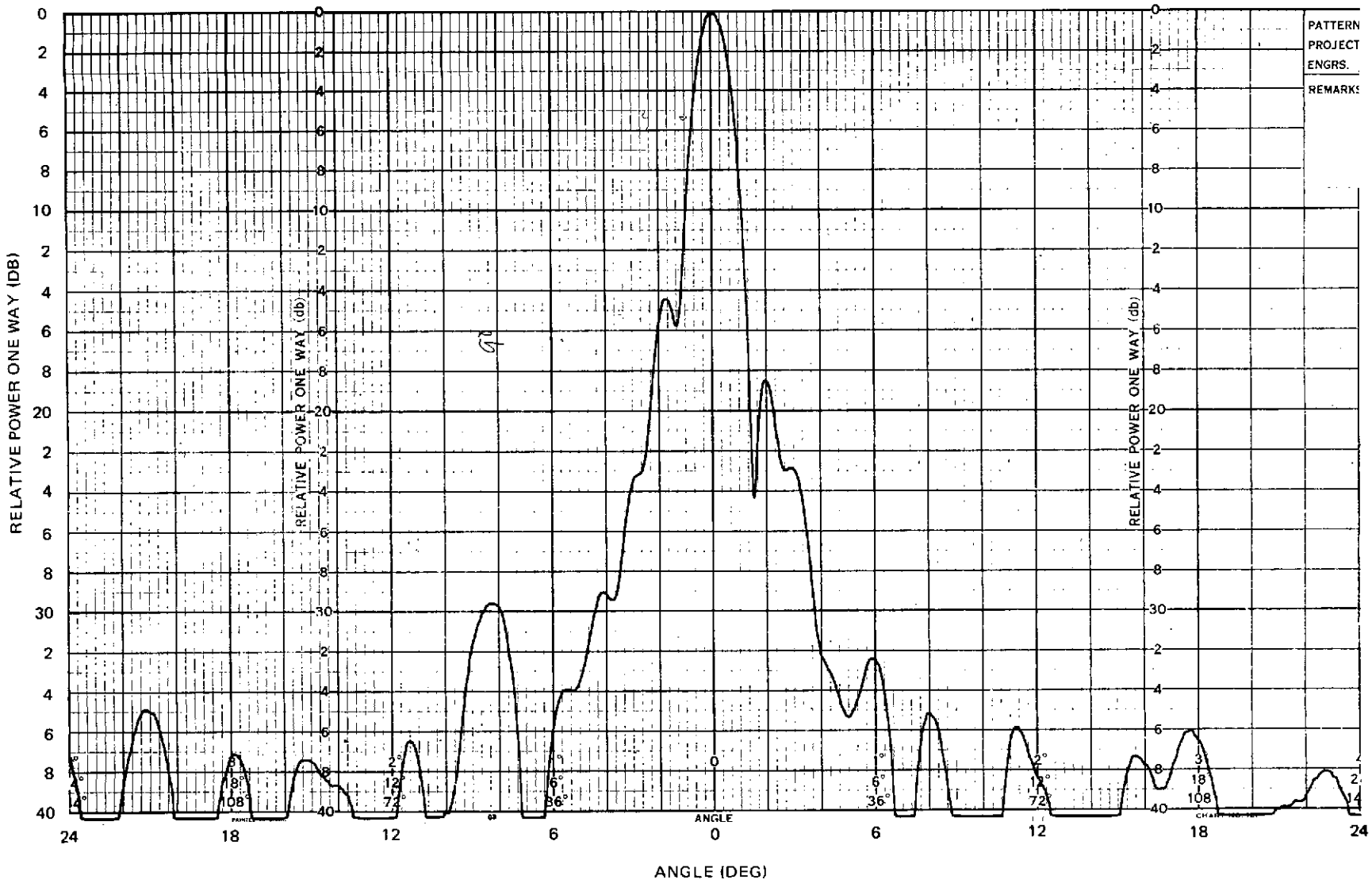

Figure 96. Port 1 E-Plane Pattern ~ Circular Polarization 13.700 GHz $\phi = 90^{o}$

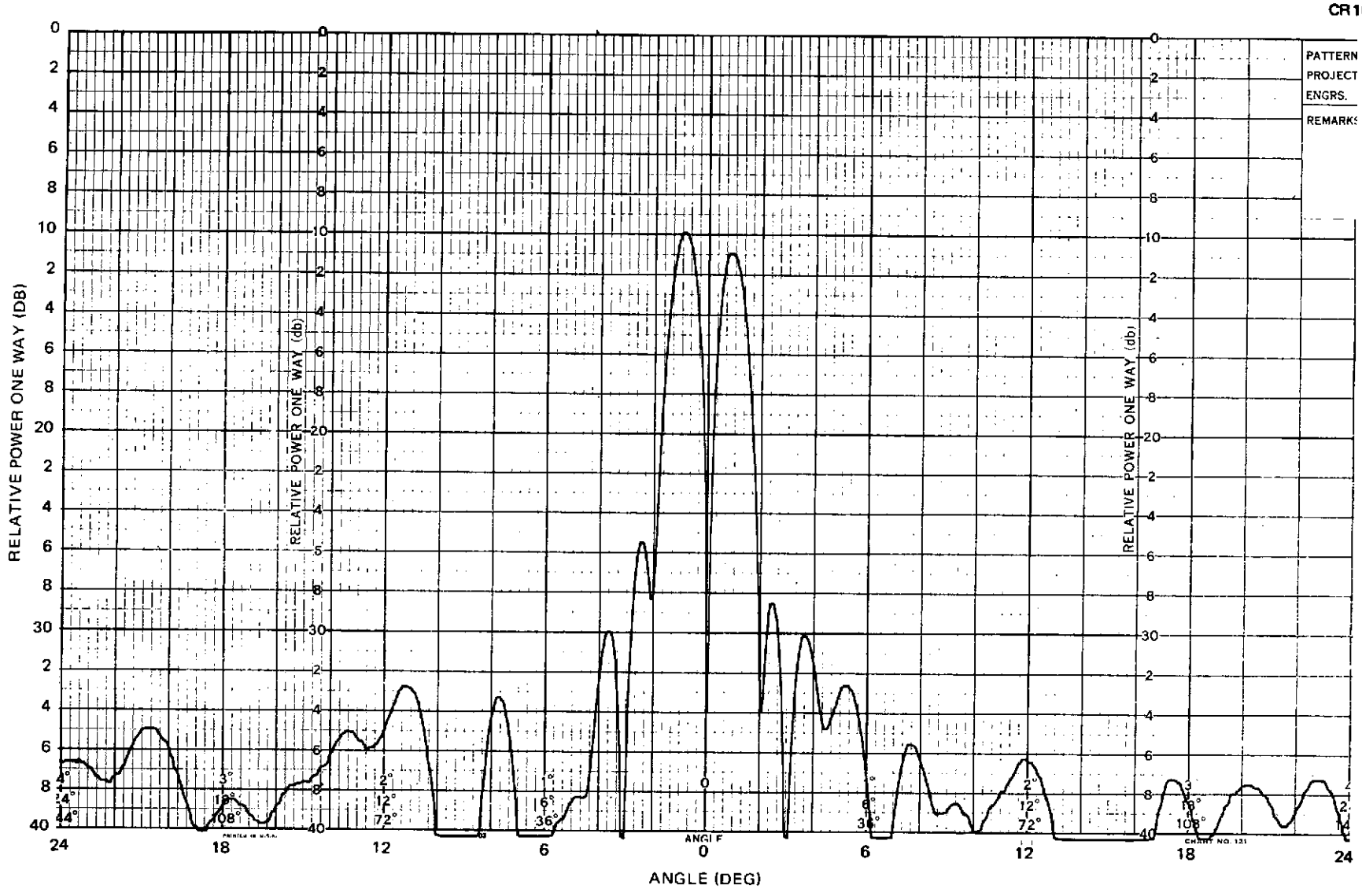

Figure 97. Port 3 Elevation Difference Pattern ~ Circular Polarization 13.500 GHz $\phi = 90^{o}$

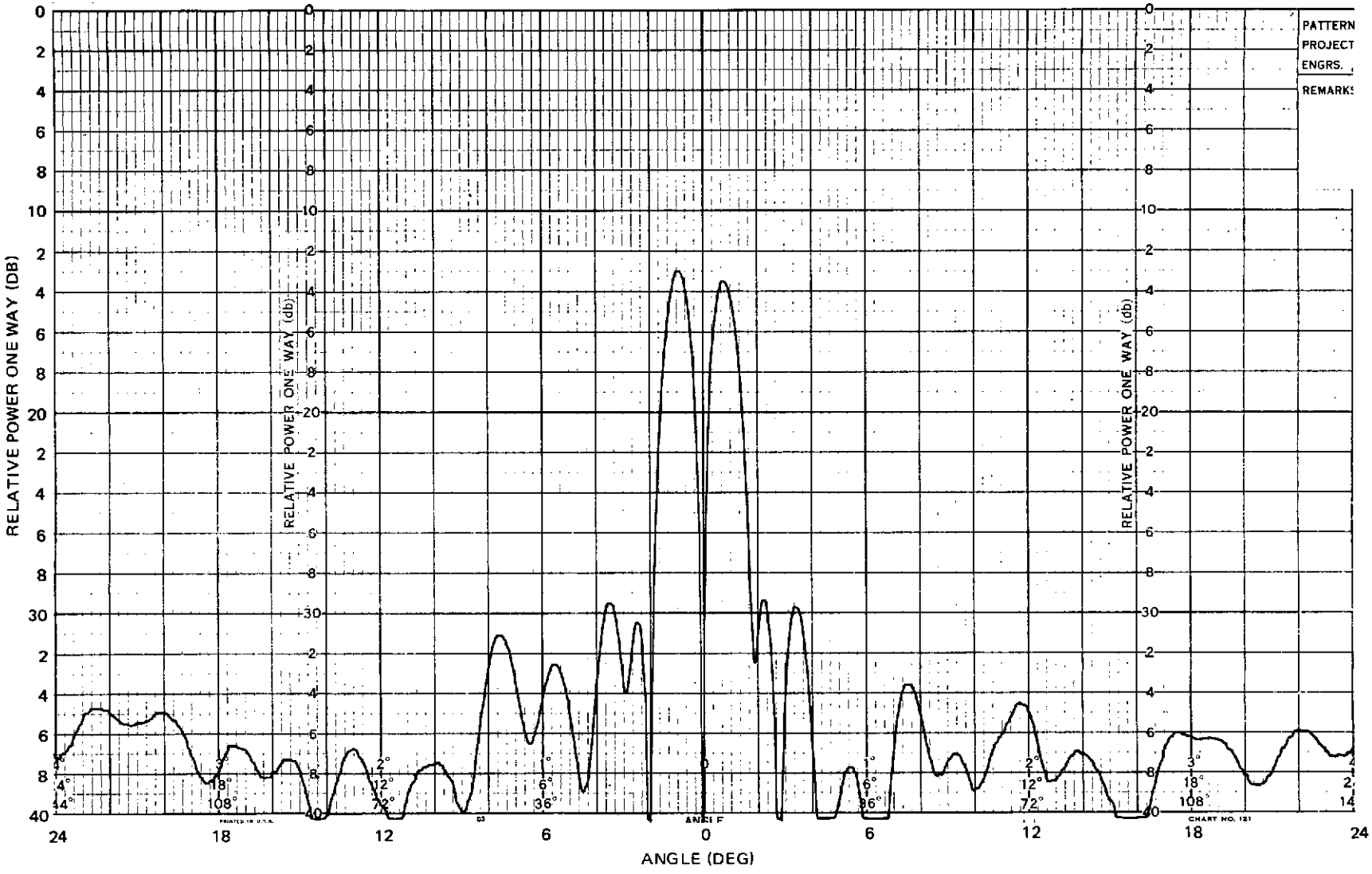

Figure 98. Port 4 Azimuth Difference Pattern ~ Circular Polarization 13.500 GHz $\phi = 0^{o}$

measurement error. The polarizer, then, is seen to be essentially free of gain degrading effects, other than the increased blockage which would be eliminated in any future iteration of the design. Overall efficiency of the circularly polarized antenna subsystem, as delivered, is 57.67 percent at 13.600 GHz and 49.89 percent at 14.650 GHz. Patterns were also measured in the configuration for transmitting left-hand circular polarization and receiving right; these patterns are essentially identical to the delivered configuration.

Patterns of the azimuth and elevation tracking signals, as derived through the complete antenna subsystem, are shown in Figures 99 and 100, respectively. The unmodulated reference sum signal (solid pattern) is shown for comparison. To obtain these patterns, the switches of the tracking network were biased to provide continuous addition or subtraction of the difference signals, as required, for each pattern cut. In actual operation, the tracking network output is a signal modulated between the two levels of the two dashed curves for any particular angle encountered. The degree of modulation versus boresight angle is plotted in Figure 101. The design goal of 20 ±2 percent per degree modulation was achieved over approximately twice the 3-db beamwidth.

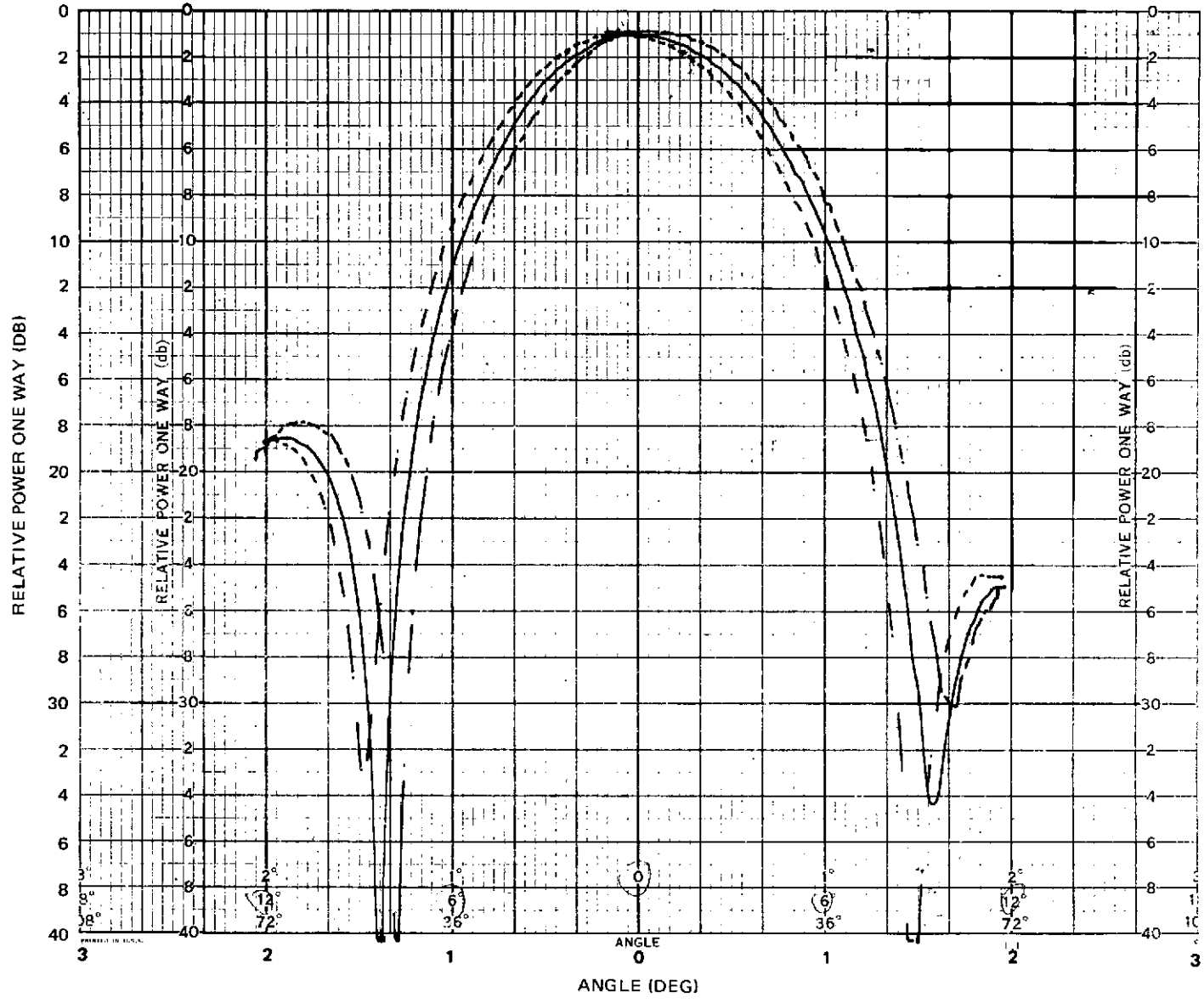

Figure 99. Azimuth Tracking Pattern

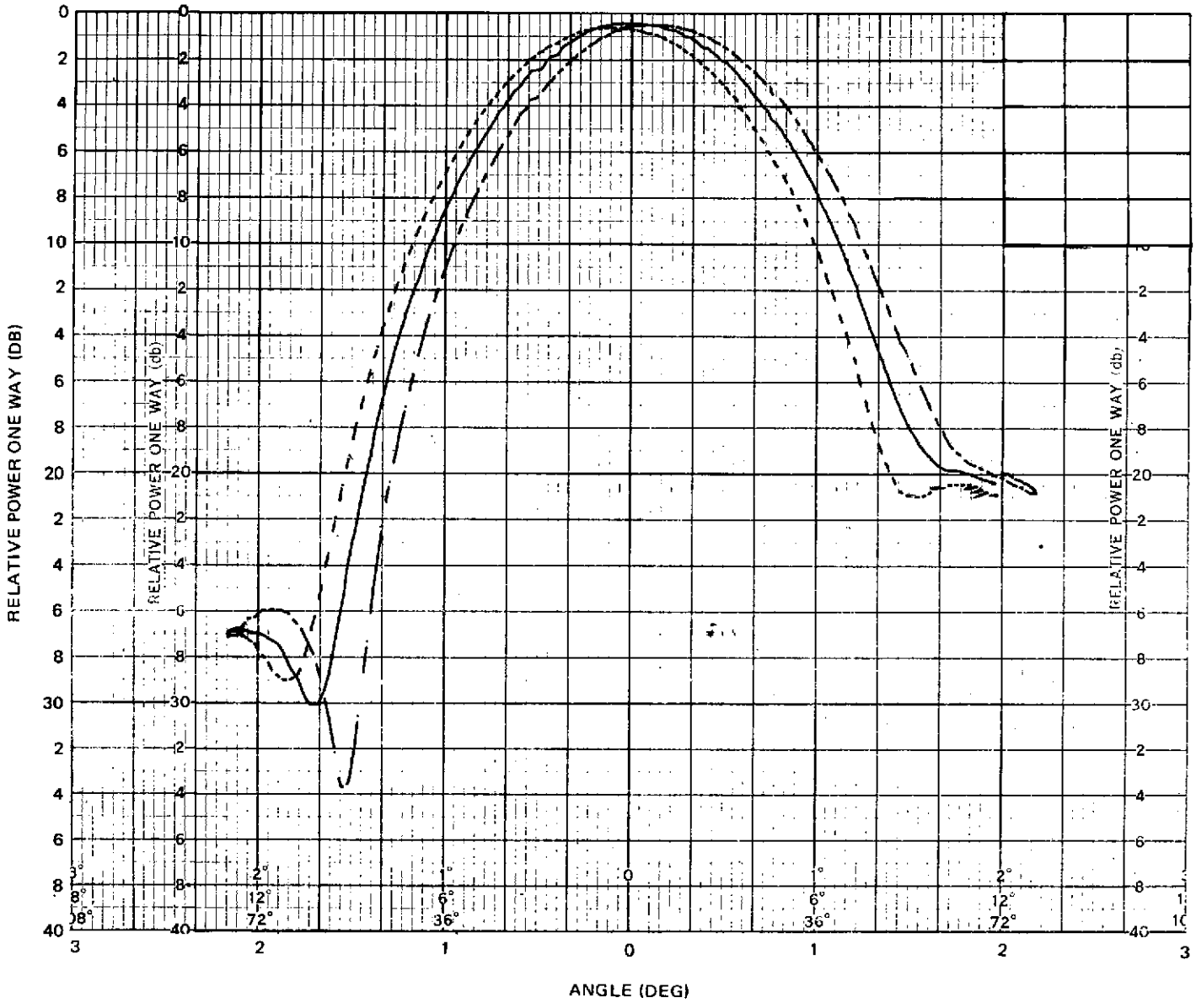

Figure 100. Elevation Tracking Pattern

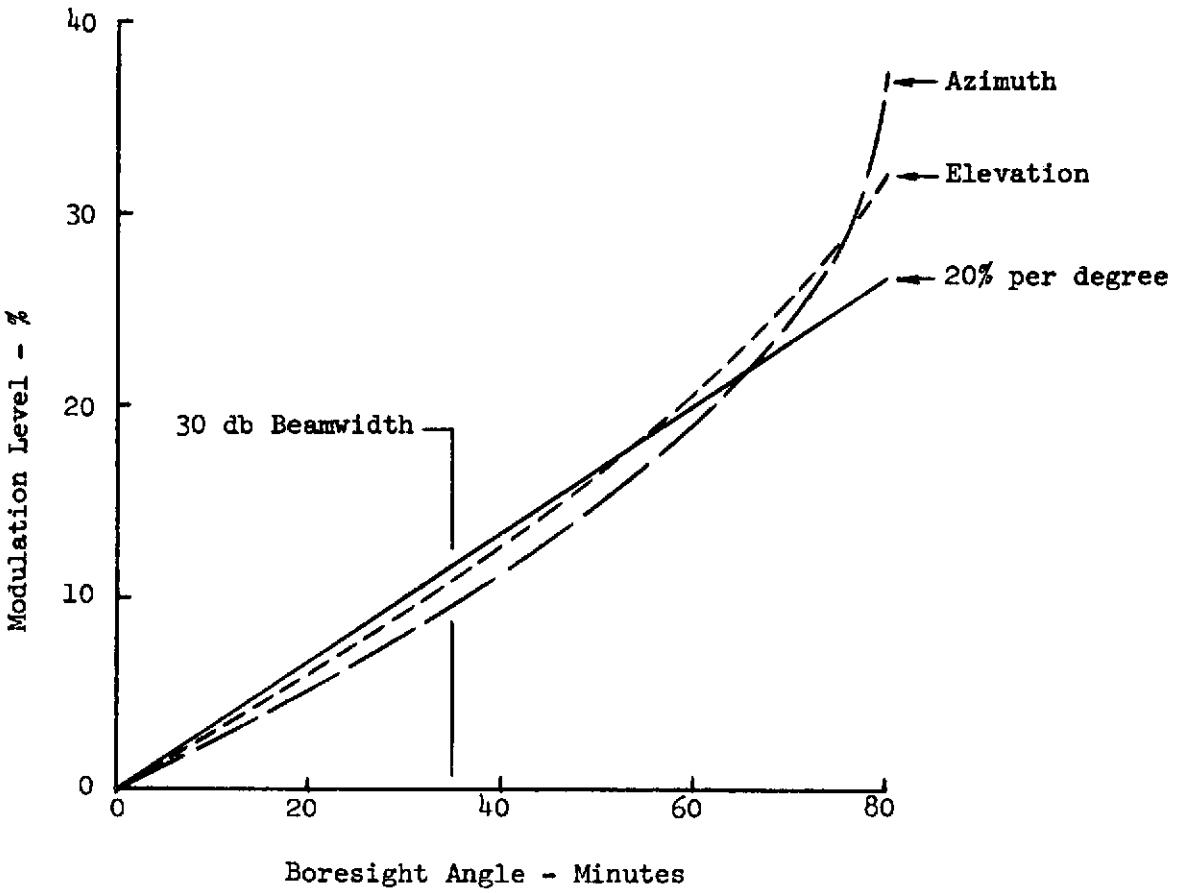

Fig. 101 Tracking Modulation Level

Section 3

PROGRAM SUMMARY

A complete working breadboard model of a K-band single-channel monopulse antenna was developed, with primary emphasis on efficiency and bandwidth of each component. The major elements of the subsystem include a near-field multimode feed, optimized Cassegrainian geometry, an add-on circular polarizer, and a single-channel tracking network. Due to funding limitations, the reflectors were not of flight quality and imposed a severe limitation on the efficiency achievable with the breadboard model. The efficiency which would be obtainable with a flight-quality antenna are shown in Section 3.1.6 to exceed 70 percent.

3.1 PERFORMANCE VERSUS SPECIFICATIONS

The antenna specifications established in the contract were delineated in Section 2.1. The performance achieved with the antenna subsystem is discussed relative to the specifications in the following paragraphs.

3.1.1 Polarization

Circular polarization is achieved with an add-on, or separable, polarizer. As delivered, the antenna is configured to transmit right-hand circular and receive left. Rotation of the polarizer by 90 degrees adapts the antenna to a transmit left and receive right configuration. Removal of the unit results in transmission of horizontal linear polarization and reception of vertical linear. Ellipticity of the polarizer is less than 2 db across the required frequency band, and less than 1/2 db over the receive band.

3.1.2 Power Handling

All components utilized in the antenna subsystem are inherently capable of handling the required 50 watts of transmitter power. The delivered subsystem is expected to be capable of operating with considerably greater power.

3.1.3 Transmit-Receive Isolation

Measurement of the isolation between transmit and receive channels was inadvertently omitted in the final subsystem measurements, but study of the pattern data indicates a considerable degree of isolation. This isolation is achieved primarily in the orthomode transducer, which has an inherent value greater than 40 db, but is degraded by reflections in the feed network and the reflector assembly. It is expected that the isolation achieved is on the order of 30 db or greater.

3.1.4 Error Signal Modulation Level

The modulation level of each of the monopulse tracking error signals on the receive sum signal is within the 20 ± 2 percent per degree specification. Modulation effects on the transmit channel were not measurable.

3.1.5 Apollo Tracking Electronics Compatibility

An interface electronics assembly is provided to adapt the +3, -50 volt switching signals of the Apollo tracking electronics to the 0, +5 volt signals required by the tracking network. An internal power supply is used to provide ±15 volt power for the switches as well as +5 volt power for the interface logic. The internal supply requires 115 volt, 60 Hz prime power. In addition, an internal circuit for simulation of the FTD I and FTD II switching signals is provided for test purposes.

3.1.6 Antenna Efficiency

The measured gain and efficiency values achieved with the antenna subsystem are shown in Table 10. The design goal parameters were predicated on a reflector surface error of approximately 0.010 inch, rather than the 0.030-inch tolerance of the commercial grade reflector. Even with the nearly 9 percent loss incurred with the larger surface error, the values achieved are relatively close to the design goals.

A breakdown of individual elements contributing to the overall efficiency is given in Table 11. Intermediate products of efficiency which are of particular interest are bracketed in that table. The values for illumination taper and spillover were calculated from the patterns of the feed network. The

Table 10

DELIVERED SYSTEM EFFICIENCY

Configuration Polarization Frequency	Design Goal	Original Alignment Linear 14.650 GHz	Final Configuration			
			Linear		Circular	
			13.600 GHz	14.650 GHz	13.600 GHz	14.650 GHz
Gain max (db)	45.44	45.44	44.79	45.44	44.79	45.44
Gain measured (db)	43.36	43.21	42.65	42.82	42.40	42.42
η measured (%)	62	59.84	61.09	54.70	57.67	49.89

product of these terms yields the aperture efficiency, which can be compared to the beamwidth efficiency, α, which is derived from measured beamwidths in Table 12. The similarity of these aperture efficiency values, determined in different manners, lends considerable credence to the analytical values. All effects not specifically accounted for, such as VSWR, ohmic and interactive loss are included in the value for feed network loss. The resulting feed efficiency is seen to be quite high, even including some losses which likely do not belong in that category.

The reflector surface error is based on the 0.030-inch tolerance of the reflector and 0.020 inch on the subreflector. Cross-polarization efficiency is estimated from the pattern results. Any loss due to surface reflectivity, which is very difficult to measure, was included in the lump sum ascribed to the feed network.

A value of potential efficiency is given in Table 11 for each frequency and configuration. This represents the overall antenna efficiency which would be obtained with a flight-quality reflector with a contour tolerance of ±0.010 inch, with the feed network ports matched to provide a maximum VSWR of 1.5:1 and with the antenna geometry adapted to optimize blockage

Table 11

EFFICIENCY BREAKDOWN

Loss Mechanism	Design Goal	Original Configuration Linear 14.650 GHz	Final Configuration			
			Linear		Circular	
			13.600 GHz	14.650 GHz	13.600 GHz	14.650 GHz
Illumination Tapes, η_i	93	92	92			
Spillover, η_s	89	94.4	94.4			
[Aperture Efficiency, $\eta_i \times \eta_s$]	[82.8]	[86.8]	[86.8]			
[Measured Aperture Efficiency, α]	--	[85.9]	[84.7]		[85.9]	
Blockage, η_b	93	89.3	89.3		84.5	
Feed Network, $\eta_m \times m_e$	86	95	97	87	97	84
Feed Efficiency, %	66.2	73.7	75.2	67.5	71.2	61.6
Reflector Surface Error, $\eta_r \times \eta_h$	97	82	82			
Cross Polarization, η_x	98	99	99			
Overall Antenna, η	62.9	59.8	61.1	54.7	57.7	49.9
Potential, η		71.5	70.1	65.4	69.7	62.8

Table 12

APERTURE EFFICIENCY

$BW = \alpha \frac{\lambda}{D}$ Minimum α for circular aperture is 58.5 deg.

Polarization	Frequency	BW_{min} (deg)	BW_{meas} (deg)	α	Average Efficiency (%)
LINEAR	13.50	1.066	1.25	68.68	
	13.60	1.058	1.25	69.24	
	13.70	1.051	1.229	68.29	
	14.55	0.989	1.177	69.63	
	14.65	0.983	1.167	69.44	
	14.75	0.976	1.157	69.26	
	Avg			69.09	84.67
CIRCULAR	13.50		1.238	67.99	
	13.60		1.232	68.05	
	13.70		1.203	66.81	
	14.55		1.173	69.38	
	14.65		1.145	68.15	
	14.75		1.138	68.11	
	Avg			68.08	85.93

in the circularly polarized configuration. These factors are readily achievable and would be expected in a flight configuration subsystem. Under these conditions, it is anticipated that an overall antenna subsystem efficiency exceeding 70 percent across the frequency band is achievable with the antenna configuration developed on this contract, and for larger reflectors for which the aperture blockage can be less, efficiencies greater than 75 percent can be obtained.

3.1.7 Pointing Accuracy

The pointing accuracy of the antenna is dependent upon characteristics of the Apollo tracking electronics and therefore was not directly measurable. However, the tracking modulation levels are within the desired range, and the receive sum and difference patterns are exceptionally stable with

frequency and demonstrate excellent null depths, so the pointing accuracy is expected to be well within the 1-db beamwidth.

3.1.8 Lightweight Implementation

Design data for a lightweight, thermally stable antenna configuration of graphite/epoxy composite construction is provided. The estimated weight for this configuration is less than 6.5 pounds for the reflectors and supporting structure. A flight-weight configuration of the feed network and tracking network is estimated to weigh an additional 3 and 2 pounds, respectively, resulting in an overall antenna subsystem weight of approximately 11.5 pounds.

3.1.9 Operating Frequency

The antenna subsystem operates satisfactorily over the 13.500- to 13.700-GHz and 14.550- to 14.750-GHz frequency bands required for receiving and transmitting, respectively. The subsystem appears to be capable of operating at high efficiency over even greater bandwidths.

3.2 POTENTIAL AREAS OF IMPROVEMENT

The commercial-quality parabolic reflector imposes a severe limitation on the efficiency achievable with the antenna subsystem. Losses due to the reflector contour amount to approximately 0.6 db more than would be encountered with a flight-quality reflector. Side lobe and cross-polarization levels which would be achievable with a precise reflector are difficult to determine. It would therefore appear quite beneficial to develop a flight-quality reflector and supporting structure for a more realistic evaluation of subsystem performance.

The space-filter network utilized for circular polarization is capable (Section 2.2.5) of considerably better performance than that obtained with the delivered configuration. Further development effort, particularly to determine the source of troublesome resonance effects and to derive an analytical basis for subsequent polarizer designs, is indicated.

Several parameters of the delivered configuration, such as blockage in the circularly polarized configuration and the VSWR of the feed network ports,

which are not at their optimum values, are readily correctable in subsequent design iterations, and require no further development effort. A combined analytical and experimental investigation to thoroughly resolve the question of near-field phase center and corresponding selection of subreflector contour (Section 2.2.4.3), should be performed in order to determine the optimum near-field configuration.

3.3 APPLICATIONS

Although designed specifically for use on earth-orbiting spacecraft, the antenna subsystem and associated techniques developed on this contract have wide areas of application. The significantly high efficiency achieved with the near-field multimode configuration would be of increasing value with increasing gain requirements, permitting the use of smaller reflector diameters for equal gain.

The 48-inch-diameter reflector of this subsystem is about the minimum size for which the Cassegrainian configuration is the optimum choice for this frequency of operation. However, the multimode feed network as a prime-focus feed is equally beneficial. The efficiency loss incurred by adapting from a near-field to far-field configuration is approximately 4 percent (less than 0.2 db), so the high efficiency characteristics of the multimode feed are readily applicable to smaller antenna implementations.

As a nontracking feed, elimination of the tracking couplers removes a major limitation on antenna bandwidth, and the multimode network is capable of providing exceptionally high efficiency over a bandwidth of 20 to 25 percent.

REFERENCES

1. P. D. Potter. The Design of a Very High Power, Very Low Noise Cassegrain Feed System for a Planetary Radar. Technical Report 32-653, Jet Propulsion Lab, Aug 1964.

2. K. H. Schetne. Wideband Communication Subsystems. McDonnell Douglas Astronautics Company Technical Report MDC G0968, March 1971.

3. P. D. Potter. A New Horn Antenna with Suppressed Sidelobes and Equal Beamwidths. Microwave Journal, Vol. VI, No. 6, pp 71-78, June 1963.

4. A. Ludwig, J. Hardy, R. Norman. Gain Calibration of a Horn Antenna Using Pattern Integration. Technical Report 32-1572, Jet Propulsion Lab, Oct 1972.

5. P. W. Hannan. Microwave Antennas Derived from the Cassegrain Telescope. IRE Trans. on Ant. and Prop., Vol. AP-9, No. 2, pp 140-153, Mar 1961.

6. P. A. Watson and S. I. Gkobrial. Off Axis Polarization Characteristics of Cassegrainian and Front-Fed Paraboloidal Antennas. IEEE Trans. on Ant. and Prop., Vol. AP-20, No. 6, pp 691-698, Nov 1972.

7. R. C. Hansen. Low Noise Antennas. Microwave Journal, pp 19-24, June 1959.

8. C. E. Profera and L. H. Yorinks. An Improved Cassegrain Monopulse Feed System. 1968 USAF Antenna R&D Symposium.

9. D. C. Hogg and R. A. Semplak. An Experimental Study of Near-Field Cassegrainian Antennas. BSTJ, Nov 1964.

10. W. D. Fitzgerald. The Efficiency of Near-Field Cassegrainian Antennas. IEEE Trans. on Ant. and Prop., Vol. AP-20, No. 5, pp 648-650, Sept 1972.

11. R. C. Hansen (Editor). Microwave Scanning Antennas. Vol. I, Academic Press, N. Y., 1964.

12. A. F. Kay. Near-Field Gain of Aperture Antennas. IRE Trans. on Ant. and Prop., Vol. AP-8, No. 6, pp 586-593, Nov 1960.

13. C. E. Profera and L. H. Yorinks. A High Efficiency Dual Frequency Multimode Monopulse Antenna Feed System. Supplement to IEEE Trans. on Aerospace and Electronic Systems, Vol. AES-2, No. 6, pp 314-322, Nov 1966.

14. D. D. Howard. A New Broadband, Efficient, and Versatile Feed for the Monopulse Tracking Radar. NRL Report 5559, Dec 1960. (CONFIDENTIAL)

15. G. Ploussios and J. Donovan. Circular Polarizer for Linear Polarized Antennas. NEREM Record, pp 50-51, 1963.

16. D. S. Lerner. A Wave Polarization Converter for Circular Polarization. IEEE Trans. on Ant. and Prop., Vol. AP-13, No. 1, pp 3-7, Jan 1965.

17. E. J. Perrotti. Low Noise Satellite Communication Antenna Feeds. Electrical Communication, Vol. 45, No. 4, 1970.

18. L. Young, L. Robinson, and C. Hacking. Meander Line Polarizer. IEEE Trans. on Ant. and Prop., Vol. AP-21, No. 3, pp 376-378, May 1973.